Searching for Long Lived Particles with ADAM

(Auxiliary Detector above the ATLAS Muon Spectrometer)

by

Rishap Lamichhane

A thesis submitted in partial fulfillment of the requirements for the degree of

Master of Science

Department of Physics

University of Alberta

Abstract

The Large Hadron Collider (LHC) is the world's largest particle accelerator, delivering proton-proton ($p-p$) collisions to various experiments, including ATLAS (A Toroidal LHC ApparatuS). The proposed Auxiliary Detector above the ATLAS Muon Spectrometer (ADAM) aims to expand the physics capabilities of ATLAS. Its primary objective is to detect the decay products of particles beyond the standard model (BSM), escaping detection from the ATLAS collisions.

Long-lived particles (LLPs) represent a key aspect of BSM theories, and ADAM has the potential to extend ATLAS's reach in this domain. One of these models of great interest is the hidden (dark) sector scalar model, which explains the origin of mass in the form of dark matter (DM). The theory suggests that DM particles acquire mass similar to electroweak symmetry breaking, forming a complete dark sector with additional scalar and vector bosons. The resulting scalar, known as the dark Higgs boson (ϕ), generally mixes with the Standard Model (SM) Higgs boson, displaying some SM-like characteristics.

While physicists aim to detect such particles, many experiments, including ATLAS, are not inherently designed for this purpose. ADAM emerges as a cost-effective enhancement to the LHC infrastructure, extending the physics reach of the current ATLAS detector. Positioned above the ATLAS detector, ADAM transforms the upper cavern region into a fiducial volume of $\sim 12,000$ m^3 for detecting LLP decays. The evaluation of the spatial resolution performance using Silicon Photomultiplier readout from the proposed ADAM detector module is presented. We also present an overview of dark Higgs bosons (DHBs) produced in rare

inclusive B meson, and exotic SM Higgs decays. Our analysis is performed under the operational scenario of High Luminosity - LHC run 4, anticipating an integrated luminosity of 715 fb^{-1} and centre-of-mass energy $\sqrt{s} = 14$ TeV. The analysis includes the reach of ADAM for the leptonic decays of lighter DHB to muons ($\phi \rightarrow \mu^+\mu^-$), with a requirement of at least three decays inside the fiducial volume, in the parameter space spanned by the mass of DHB (m_ϕ) and the mixing term $\sin^2\theta$. Additionally, a comparison between the reach of ADAM and the existing experimental bounds for the DHB is also presented.

Preface

The proposed ADAM detector design and its components presented in Chapter 4 is based on the discussions between Dr. James Pinfold, Joseph Mitchell Kelly, and myself. The simulation setup in $GEANT4$ for the proposed ADAM detector module presented in Chapter 5 and the evaluation of the spatial resolution performance using SiPM readout presented in Chapter 6 is my original work. The theoretical foundation of the DHB discussed in Chapter 7 builds upon my own study, incorporating findings from previous theoretical and experimental research in this field. The simulation of production and the decay of the DHBs using the Monte Carlo event generator $Pythia8$ to explore the parameter space $(m_\phi, \sin^2\theta)$ for ADAM presented in Chapter 8 is my original work as well.

Acknowledgments

First and foremost, I would like to extend my sincere gratitude to my supervisor, Dr. James Pinfold, for his invaluable guidance in selecting this research topic and generously sharing his profound knowledge of particle physics. Throughout this journey, he consistently instilled a sense of adventure and passion for research, providing crucial direction and nurturing the development of my scientific mindset. Dr. Pinfold's kindness, encouragement, humor, and inspiring demeanor have made the entire process a truly enriching experience. I also express my sincere gratitude to Dr. Doug Gingrich and Dr. Juan Pablo Yanez Garza for their roles on my supervisory committee.

Special thanks go to Dr. Ameir Shaa Bin Akber Ali, Dr. Michael Staelens, Abhinab Mukhopadhyay, and Joseph Mitchell Kelly for their unwavering assistance throughout my research project. Their support has been instrumental, and without their help, the completion of this dissertation would not have been possible. In this academic journey, the support and love of friends and colleagues, Nuzhat Anjum, Apsana Kafle, Muhammad Mubasher, Syed Navid Reza, Hitesh Chopra, and many others, have been crucial for me. I am profoundly grateful for the warmth that you have provided, turning my academic pursuit into a genuinely enriching life experience. I will forever cherish these memories as a significant part of my life.

Lastly, I want to express heartfelt appreciation to my family for their unwavering and unconditional support. I dedicate this dissertation to you for your support in my educational pursuits and professional development.

Contents

List of Abbreviations

ADAM Auxiliary Detector Above the ATLAS Muon Spectrometer

APD Avalanche Photodiode

ATLAS A Toroidal LHC Apparatus

BBN Big Bang Nucleosynthesis

BSM Beyond the Standard Model

C.L Confidence Level

CERN European Center for Nuclear Research

CMB Cosmic Microwave Background

DHB Dark Higgs Boson

DM Dark Matter

FWHM Full Width Half Maximum

GAPD Geiger-mode Avalanche Photodiode

HL-LHC High Luminosity LHC

HLT High-Level Trigger

IP Interaction Point

ISR	Intrinsic Spatial Resolution
LEP	Large Electron-Positron Collider
LHC	Large Hadron Collider
LLPs	Long-Lived Particles
LS	Long Shutdown
LSF	Light Spread Function
MS	Muon Spectrometer
p.d.f	Probability density function
PDE	Photon Detection Efficiency
PS	Positron Synchrotron
PSF	Point Spread Function
QCD	Quantum Chromodynamics
QE	Quantum Efficiency
QED	Quantum Electrodynamics
QFT	Quantum Field Theory
RF	Radio Frequency
SiPM	Silicon Photomultipliers
SM	Standard Model
vev	Vacuum Expectation Value
WLS	Wavelength Shifting

List of Tables

List of Figures

Chapter 1

Introduction

The Large Hadron Collider (LHC) is the world's largest particle accelerator dedicated towards the exploration of the fundamental constituents of matter. The ATLAS (A Toroidal LHC ApparatuS) [1] and CMS (Compact Muon Solenoid) [2] experiments at the LHC discovered the Higgs Boson in 2012 [3, 4], the last piece of the Standard Model (SM) puzzle. The SM is a theory that describes the fundamental particles and forces of the universe [5, 6], but it's not necessarily a complete theory of all phenomena in the universe [7]. There are several limitations, like the nature of dark matter and dark energy [8]. These limitations have led to the development of theoretical models beyond the Standard Model (BSM), which tries to overcome the current limitations of the SM. There are many BSM theoretical models that try to address these limitations [9].

Hidden sector models are theoretical frameworks in particle physics that propose the existence of additional particles and forces beyond those described by the SM [7]. A generic benchmark model can be considered where the hidden sector is weakly coupled to the SM by a mediator particle which mixes with its SM counterpart [7]. The mediator particle, known as the Dark Higgs Boson (DHB), can decay into known SM particles because of the mixing. Many experiments, including ATLAS, are not inherently designed to detect these particles because they can have extended lifetimes. This thesis focuses on the simulation of DHBs production using the Monte Carlo event generator *Pythia*8 [10] at the ATLAS experiment and their subsequent detection of decay products in the proposed auxiliary detector named ADAM (Auxiliary Detector above the ATLAS Muon spectrometer). We are proposing that ADAM would be positioned above the ATLAS experiment transforming the upper cavern region into a fiducial volume of $\sim 12,000$ m^3 for detecting long-lived particle (LLP) decays. The simulation of the proposed ADAM detector module is performed using $GEANT4$ [11] for the evaluation of the spatial resolution performance using Silicon Photomultiplier (SiPM) readout.

This thesis is organized as follows: Chapter 2 describes the SM, exploring its limitations and theories beyond it. Chapter 3 provides an in-depth look into the LHC, discussing its operational mechanisms and detailing the ATLAS experiment. Chapter 4 describes the proposed ADAM detector and its components. The simulation setup for the proposed ADAM detector module is presented in Chapter 5. The evaluation of the spatial resolution performance using SiPM readout from the proposed simulation setup module is presented in Chapter 6. Chapter 7 introduces the theory predicting the scalar DHB, which mixes with the SM Higgs boson. The properties and phenomenology of the DHB are also discussed. Chapter 8 includes the discussion on the simulation of production and the decay of the DHBs. The reach of ADAM for the leptonic decays of the DHB to muons in the parameter space spanned by the mass of DHB (m_ϕ) and the mixing term $\sin^2\theta$ is presented. Additionally, the conclusion of the study and a future outlook for the proposed ADAM detector is presented in Chapter 9.

Chapter 2

The Standard Model

2.1 Fundamental Particles and Forces

The SM is a theory that describes the fundamental particles and forces of the universe [5, 6]. The SM describes the fundamental particles in the universe with an intrinsic internal angular momentum quantum number called spin. These fundamental particles are categorized into two classes based on their associated spins:

- Fermions: Half-odd-integer spins $\left(\frac{1}{2}, \frac{3}{2}, ...\right)$
- Bosons: Integer spins (0, 1, 2, ...)

The fermions are further categorized into two classes, leptons and quarks, depending on whether they carry the colour charge or not. The lepton generations consist of: the electron, the muon, and the tau lepton. Each of them are accompanied by a corresponding neutrino, which are the nearly-massless neutral leptons. The quark generations consist of: the up and down quarks, the charm and strange quarks, and the top and bottom quarks.

There are four known fundamental forces that govern our universe: the strong force, the electromagnetic (EM) force, the weak force, and the gravitational force. Since there is no adequate theory for quantum gravity, the SM is only able to describe the first three of these forces. These forces are propagated by the exchange of the spin-1 vector bosons: gluons, photons, and the W and Z bosons. These vector bosons are emitted and absorbed by the particles while propagating the forces between them. There are eight gluons that mediate the strong force, a singular photon mediates the EM force, and the $W^{\pm}$ and Z^0 bosons mediate the weak force.

The spin-0 Higgs boson is the newly discovered particle, which is responsible for giving the mass of all the fundamental particles. There exists an anti-matter counterpart for each of the fermions in SM with equal mass but opposite quantum numbers. As seen in Figure 2.1.1 [12], there are three generations of leptons and quarks ordered by the increasing mass. The charged leptons interact via the EM and weak forces, while the quarks can interact via all three forces.

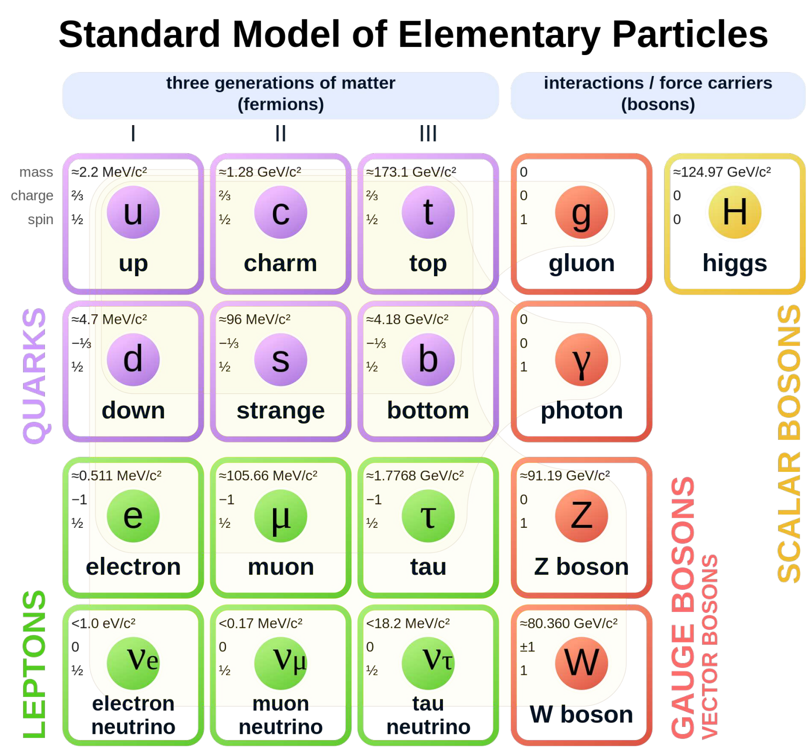

Figure 2.1.1: The twelve fundamental fermions and the five fundamental bosons as described by the SM [12].

The mathematical framework for the SM is given by a relativistic quantum field theory

(QFT) [13]. Each of the particles are described in terms of a dynamic field that permeates through space-time. The excitations in each field corresponds to a particle in that particular field. The Lagrangian formulation is used to describe the dynamics and interactions between the particle fields. The general Lagrangian formulation for the SM has 19 free parameters, which have already been experimentally determined [14]. With the application of the concept of symmetry to the Lagrangian, the SM presumes that all the fundamental interactions are described by the gauge theories. By imposing local gauge invariance, invariant under the group of local transformations (gauge transformations), introduces new vector fields (gauge fields). This gives rise to new interaction terms in the Lagrangian which couples the fermion fields to the vector fields. There is a corresponding gauge group for every kind of interactions.

Quantum electrodynamics (QED) is an abelian gauge theory with the symmetry group $U(1)$ of electrodynamics [13]. The $U(1)$ gauge transformations corresponds to the change in the phase of the wave function. A gauge field, the electromagnetic four-vector potential $A_\mu(x)$, is introduced to maintain the gauge invariance [15]. The gauge field $A_\mu(x)$ mediates the electromagnetic interaction with the photons as the quanta. For the strong nuclear force interactions, the gauge group of Quantum Chromodynamics (QCD) is the non-abelian gauge theory with the symmetry group $SU(3)$ [13]. The colour charges are the QCD counterpart of the electric charges, and the gluons are the mediators like photon in QED. The gluons exist in the adjoint representation of $SU(3)$ with eight possible colour charges. They are represented by a combination of colour and anti-colour charges.

The weak force is given by the gauge group $SU(2)$ [13]. The weak charged-current mediated by the $W^\pm$ bosons, is associated with the weak isospin $SU(2)_L$ local gauge symmetry, which gives rise to the $W^\pm$ bosons and a neutral gauge field. The SM describes the electromagnetic interaction and the weak interaction as two different aspects of a single electroweak interaction. The Glashow–Salam–Weinberg model of electroweak unification [16, 17, 18] shows that this neutral field mixes with the photon-like field to give the physical photon and Z boson fields. The photon-like field is of the $U(1)_Y$ gauge symmetry, and the field associated with this symmetry couples to a weak hypercharge, Y. This results in both the electromagnetic and weak force, and the mixing of its gauge fields gives rise to the photon and the Z^0 boson.

2.1.1 The Higgs Boson

The local gauge symmetry is satisfied if the gauge boson for an interaction is massless. As discussed before, the gauge bosons are massless in the case of QED and QCD interactions. However, the large masses are observed for the $W^{\pm}$ and Z^0 bosons, which is in contradiction with the requirement of gauge invariance. This contradiction is resolved by the introduction of the Higgs mechanism. The spontaneous breaking of symmetry triggers the Higgs mechanism which causes the bosons it interacts with to have a mass (see Appendix §A.2). The Higgs mechanism introduces a doublet complex scalar field because of which the vacuum state is degenerate. The spontaneous breaking of this symmetry with the $SU(2)_L \times U(1)_Y$ gauge symmetry provides mass to the $W^{\pm}$ and Z^0 bosons while the photon remains massless. The consequences of this effect can be seen in Figure 2.1.2 [19], which provides clearer picture of the SM.

The Higgs field sets the mass scale for the electroweak bosons because of the non-zero vacuum expectation value. The interaction between the fermion fields and the non-zero expectation value of the Higgs field provides a gauge-invariant mechanism for the generation of the SM fermions masses. Their mass is directly proportional to the strength of their interactions (Yukawa interactions) with the Higgs field. The discovery of a new spin-0 particle associated with the Higgs field, the Higgs boson with a mass of 125 GeV, was announced jointly by the ATLAS and CMS experiments on 4^{th} July 2012 [3, 4] .

2.2 Limitations of the Standard Model

While the Standard Model (SM) of particle physics has been highly successful in describ-

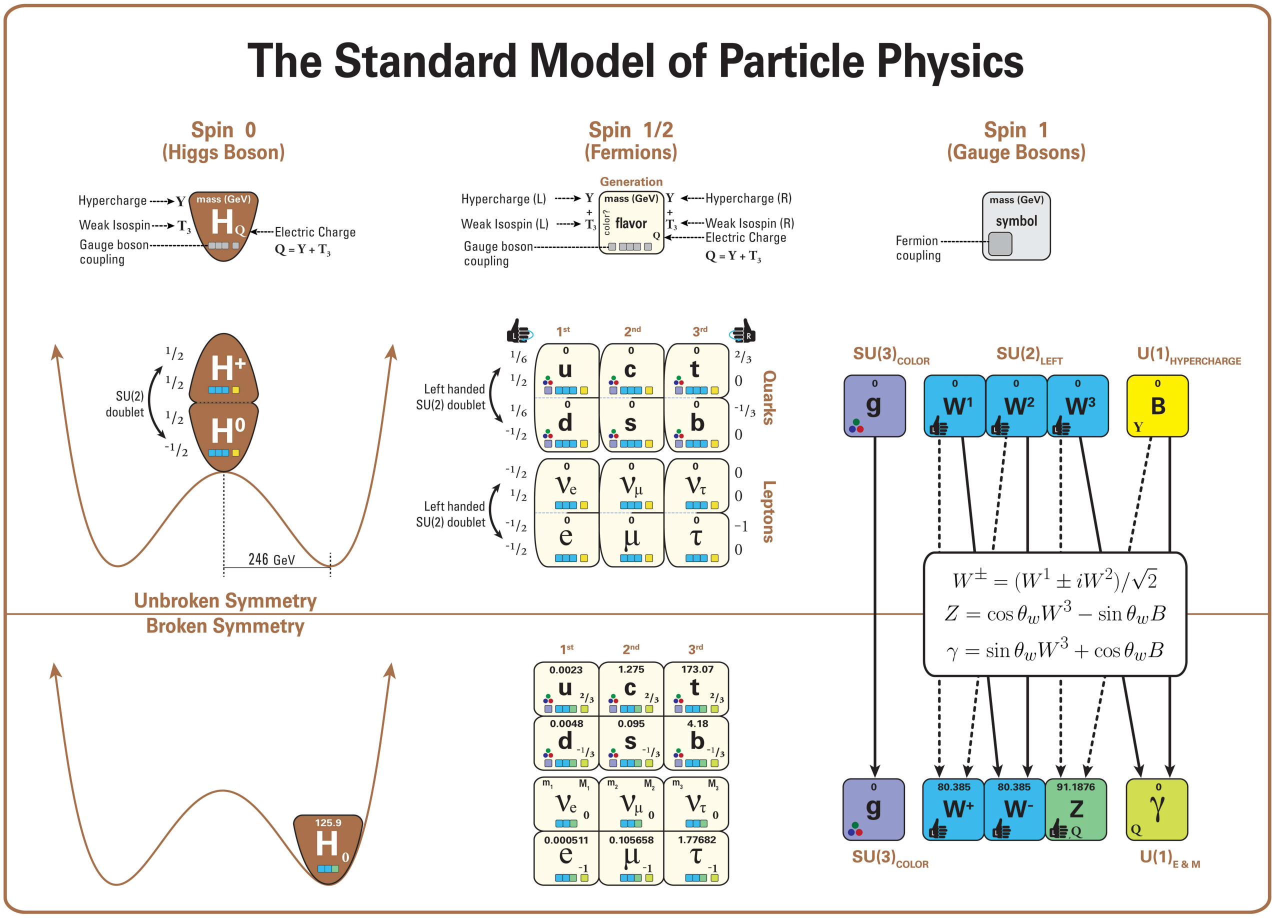

Figure 2.1.2: A diagram depicting all the particles in SM (their properties) along with the gauge bosons. It also depicts how the Higgs vacuum expectation value breaks the electroweak symmetry which changes the properties of the remaining particles as a consequence [19].

ing the fundamental particles and three of the fundamental forces (electromagnetic, weak, and strong), it also has several limitations, indicating that it's not a complete theory of fundamental particles and interactions. We will now look at some of the most important limitations of the SM [7].

2.2.1 Dark Matter and Dark Energy

The prediction of the dark matter (DM) comes from the astrophysical observations of rotational curves of stars and galaxies clusters being incompatible with the Einstein's theory of general relativity [8]. It does not interact with EM force as the conventional matter. It also does not absorb, reflect, or emit light. So the existence of DM has only been deduced based on the gravitational interactions with the visible matter. The matter as described by SM only accounts for about 5% of the total mass of the universe based on the theoretical models and the cosmological observations of the universe. Dark matter is estimated to constitute about 27% of the total energy density of the universe and Dark energy is estimated to constitute the remaining 68% [20]. The SM fails to explain the particle nature of the DM at the moment. The studies of the cosmic microwave background (CMB) has shown that our universe began with the inflation and is still undergoing accelerating expansion [21]. It was hypothesized during the observation of distant type $1A$ supernovae, which showed that the universe's expansion is accelerating [22]. Due the gravitational attraction of matter and energy, it was widely believed that the universe's expansion should be slowing down. Dark energy has a repulsive gravitational effect, causing galaxies to move away from each other at an accelerating rate. This effect counters the gravitational attraction of matter, leading to the expansion of the universe becoming faster over time. The nature of dark energy remains a mystery and no explanations exist in the current SM.

2.2.2 Baryon Asymmetry

In the SM framework, each particle has an anti-particle. For a charged particle, there exists a particle with opposite charge with identical properties. Cosmological measurements show that, out of ordinary matter, the universe is primarily made of matter [23], which contrasts with the SM framework. Our very existence and the observation suggests that there is an asymmetry in the presence of matter versus anti-matter. From the currently-known interactions that violate charge-parity invariance in SM does not account for the abundance of matter.

2.2.3 Neutrino Oscillations

Neutrinos are elementary particles that belong to the family of leptons, along with electrons, muons, and tau particles. For many years, it was believed that neutrinos were massless, as predicted by the SM. However, experimental evidence from neutrino oscillation experiments has conclusively demonstrated that neutrinos undergo oscillations between the different generations of neutrinos [24]. This phenomenon can only occur if neutrinos have mass. The discovery of neutrino oscillations was awarded the Nobel Prize in Physics in 2015.

2.2.4 Higgs Mass Fine Tuning

The Higgs boson is the scalar field in SM that gives mass to fermions. In the SM, all the particles masses are the parameters that must be experimentally determined [14]. The scalar Higgs field from quantum corrections due to virtual particles that would drive the mass to a larger scale (around 10^{19} GeV) [25]. However the experimentally observed Higgs mass is only around 125 GeV [3, 4]. This can be explained by the existence of fine-tuning of the parameters of the SM, causing a cancellation which results in the observed mass of the Higgs. However, this process is considered "unnatural" because it does not naturally occur from the theory itself and is yet to be fully understood.

2.2.5 Gravity

As we discussed before, the current framework of SM fails to explain gravity. Some theories arising from quantum field theory framework proposes a hypothetical spin-2 particle [26], graviton, which has not yet been experimentally verified. The particle interactions considered in SM is on a scale where gravity is negligible because of the weak coupling strength of gravity compared to other fundamental forces. So it is even more difficult to experimentally connect the gravitational force in the SM framework.

2.3 Physics Beyond the Standard Model

The BSM physics are different theoretical models that try to overcome the current limitations of the SM. There are many BSM theoretical models that try to address these limitations [9]. However, it is often impossible from experimental point of view to explore all these theories. So a better way to explore them would be to perform dedicated searches for features that are common to many of these theoretical models. One of these well-known features that is common in various BSM models is LLPs.

2.3.1 Long-Lived Particles

The particles in the SM have lifetimes (τ) spanning various order of magnitudes. They span from 2×10^{-25} s for Z boson to $\sim 10^{34}$ yrs for proton. Various BSM theories predicts new particles that can have a wide variety of masses and lifetimes [9]. The weak-scale particles can have longer life-times because of small couplings between the LLP and the lighter states, and suppressed phase space that are available for the decays. Depending on the models, the LLPs can have different properties. The decay mode may also be different, where they may decay into photons, invisible particles, hadronically, leptonically or semi-leptonically. Looking at the decay length, the possible experimental signatures can be different from those expected in the SM processes.

2.3.2 Hidden Sector

Hidden sector models are theoretical frameworks in particle physics that propose the existence of additional particles and forces beyond those described by the SM [7]. These particles and forces are considered "hidden" because they do not directly interact with the known particles of the SM through the strong, weak, or electromagnetic forces. Instead, they interact through new, as-yet-unknown interactions that may only manifest themselves under certain conditions or at very high energies. A generic benchmark model can be considered where the hidden sector is weakly coupled to the SM by a mediator particle which mixes with its SM counterpart [7].

2.4 Summary

Exploring hidden sector models involves both theoretical and experimental efforts aimed at understanding the potential existence and properties of particles and forces beyond those described by the SM. The existence of LLPs is predicted by many of these models, whose signatures may have been overlooked previously in particle detector experiments. This thesis will focus on one of the benchmark models featuring LLP being produced from the hidden sector.

Chapter 3

The Large Hadron Collider

The LHC stands as the world's largest particle accelerator, boasting a circumference of 27 km. It resides approximately 100 m underground, beneath the European Centre for Nuclear Research (CERN), situated near the border between France and Switzerland, in the vicinity of Geneva. Occupying the tunnel previously housing the Large Electron-Positron Collider (LEP), its primary purpose is to collide hadrons at a maximum centre-of-mass energy of $\sqrt{s} = 14$ TeV. The LHC has undergone several upgrades and at the time of this thesis operates at $\sqrt{s} = 13.6$ TeV [27]. The information on the LHC technical report can be found in [28].

While the LHC possesses the capability to accelerate heavy ions like lead, it predominantly accelerates protons for the majority of its operations. This discussion will focus on proton-proton ($p-p$) collisions. The complete CERN accelerator complex, detailed in Figure 3.1.1, encompasses a sequence of smaller accelerators where protons progressively gain energy before they are introduced into the LHC in two counter-rotating beams. Surrounding the LHC ring, you'll find the four principal physics experiments of the LHC - ALICE [29], CMS [2], LHCb [30], and ATLAS [1]- positioned at intersecting points where the two beams collide. These experiments are integral to unraveling the mysteries of the universe at the subatomic level. ATLAS and CMS stand as the two most substantial multi-purpose experiments, while

LHCb primarily centres on precision measurements related to CP violation and rare decays of hadrons. ALICE, on the other hand, is specifically devoted to exploring the properties of quark-gluon plasma produced during heavy-ion collisions—a phenomenon that the LHC is also proficient at generating.

In addition to these four primary experiments, the LHC accommodates five supplementary experiments: MoEDAL-MAPP [31, 32], TOTEM [33], FASER [34], LHCf [35], and SND [36]. Each of these experiments serves to enrich our understanding of particle physics, contributing diverse perspectives and insights to the broader field of scientific exploration.

3.1 Proton Acceleration

The LHC's accelerator complex commences with the injection sequence. Protons utilized for collision are sourced from hydrogen gas, wherein the electrons are removed [37]. These protons then enter the Linac4, a linear accelerator, marking the initial phase of acceleration, elevating their energy to 160 MeV. Subsequently, the protons advance to the Proton Synchrotron Booster (PSB), where their energy experiences a boost to 2 GeV. This energy-enhanced proton stream is next introduced into the Proton Synchrotron (PS), where they undergo further acceleration to reach the range of $14 - 26$ GeV. The ultimate stage in the injection sequence takes place at the Super Proton Synchrotron (SPS), where the protons are propelled to an energy level of 450 GeV, preparing them for injection into the primary LHC ring [38]. The LHC employs Radio Frequency (RF) cavities and bending magnets to transition from 450 GeV to 7 TeV. RF cavities are instrumental in providing the essential longitudinal acceleration, contributing to the increase in beam energy. Meanwhile, the bending magnets perform the crucial function of ensuring transverse acceleration, thereby sustaining the circular trajectory of the particles. The LHC boasts 1232 superconducting dipole magnets composed of superconducting Niobium-Titanium ($NbTi$) coils, which are cryogenically cooled down to 1.9 K by superfluid helium to generate an intense magnetic field of 8.33 T.

This magnetic system effectively maintains the protons in orbit at the designated energy level of 7 TeV. Quadrupole magnets, on the other hand, are used to concentrate and focus the beams within the accelerator [39].

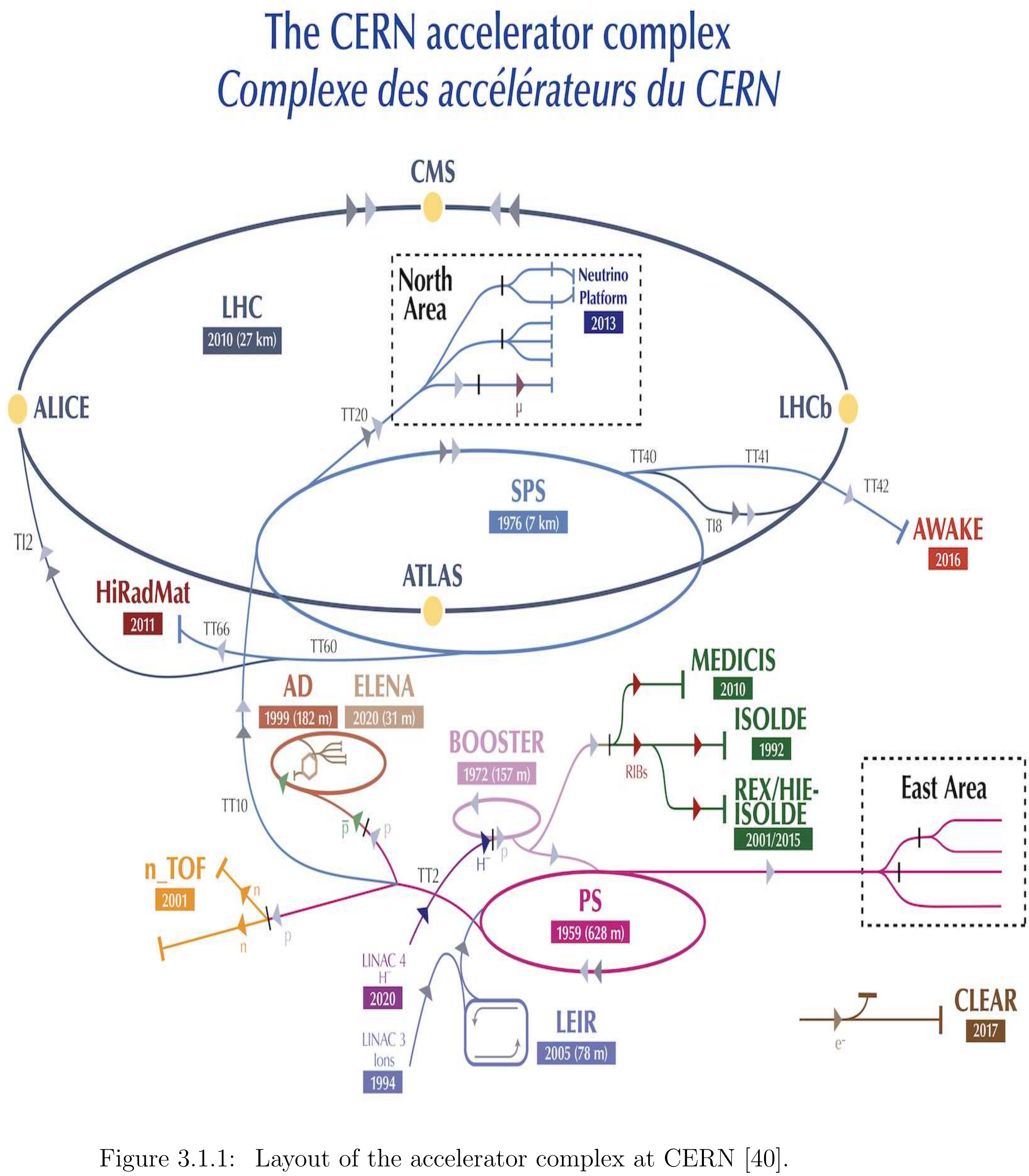

Figure 3.1.1: Layout of the accelerator complex at CERN [40].

Sustaining the required ultra-low temperature is the task of the LHC's cooling system. Achieving this demands an extensive cryogenic system that incorporates both liquid nitrogen and superfluid helium. The LHC ring is divided into eight distinct sections (or points). Points 1, 2, 5, and 8 are where the counter-rotating beams are intentionally brought into collision, representing the interaction points that house the primary experiments. The remaining points fulfill various roles as beam service facilities. Points 3 and 7, for instance, accommodate beam cleaning services responsible for collimating the beams, ensuring particles remain on the designated beam path. Point 4 is home to the superconducting RF cavities that play a pivotal role in elevating beam energy from 450 GeV to 7 TeV. In the event of malfunctions, Point 6 houses the "beam dump" facility, utilizing "kicker" magnets to swiftly redirect the beams out of the LHC ring and into an external absorber.

3.2 Beam Structure

The operation of the LHC entails a complex procedure for managing the circulation of proton beams. Contrary to the notion of a continuous flow, protons are organized into discrete groups known as "bunches". These bunches are initially structured by the smaller machinery within the LHC's injection system and are subsequently fine-tuned by the RF cavities.

The RF cavities produce an oscillating electromagnetic field that acts along the beam's direction, inducing what is referred to as "synchrotron oscillations" in the bunches, each containing up to 1.2×10^{11} protons. This oscillation takes place as the bunches traverse the LHC ring. The oscillating RF field plays a pivotal role in shaping the proton bunches by either accelerating or decelerating protons that lag behind or lead the central portion of the bunch.

The LHC's RF cavities operate at a frequency of 400 MHz, which governs the positioning of proton bunches. These positions are termed "RF buckets" and, in combination with the LHC's circumference, determine the maximum quantity of proton bunches that can be accommodated within the LHC. While the LHC is in operation, there are approximately 35640 RF buckets available, although not all are filled with proton bunches. Additionally, during routine operations, the train of "buckets" naturally decays as bunches are collided at the interaction points and is periodically replenished.

The minimal separation between RF buckets containing proton bunches is 10 RF buckets, which implies that there is a gap of at least 9 unfilled RF buckets following one that contains a proton bunch. This corresponds to a minimum inter-bunch duration of 25 ns, also known as "bunch spacing". Presently, the LHC's operating conditions for Run 3 are anticipated to comprise 2808 bunches spaced 25 ns apart, each with 1.8×10^{11} protons per bunch (ppb) [27]. The precise bunch spacing and overall bunch structure are determined by LHC operators and the detector capabilities at specific interaction points. The choice of shorter bunch spacing results in a higher collision intensity and multiplicity at these interaction points. A 25 ns bunch spacing corresponds to a maximum proton-proton collision rate of 40 MHz, a constraint dictated by the design of the detectors at these interaction points.

Occasionally, issues may arise during the LHC filling process, leading to bunches occupying incorrect RF buckets. This can result in collisions occurring at undesired locations within the detectors, which disrupts their data acquisition systems. In cases of unsatisfactory beam quality, the beam is deliberately dumped, and the LHC undergoes a refilling procedure. The beam dumping process entails the use of kicker magnets to redirect the beam out of the storage ring. These kicker magnets require a minimum window of 3 μs to reach full field strength. The refilling process for the LHC takes approximately 3 minutes per beam [38].

3.3 Luminosity

To determine the quantity of physics events anticipated during a specific data acquisition interval, it is important to understand the rate at which proton collisions take place. It is a very important measure in the context of high-energy physics and the research at LHC. This rate is denoted as “instantaneous luminosity” ($\mathcal{L}$), and it essentially signifies the number of potential collisions that could transpire at a particular moment. The luminosity is determined by the formula

$$\mathcal{L} = \frac{f_{rev} n_b N_p^2 \gamma R}{4\pi \beta^* \epsilon_n}, \tag{3.3.1}$$

where

$$R = \frac{1}{\sqrt{1 + \frac{\theta_c \sigma_z}{2\sigma_{xy}}}}. \tag{3.3.2}$$

Here f_{rev} is the frequency of revolution, n_b is the number of bunches, N_p is the bunch population, and γ is the proton beam energy. The geometrical factors that describe the shape of the beam are given by β^*, ϵ_n, θ_c, σ_z, and σ_{xy}, which represents focal length, normalized transverse emittance, crossing angle, transverse, and longitudinal r.m.s. size respectively. The integrated luminosity is needed to measure the total number of collisions to be achieved over time. It is related to the instantaneous luminosity by the formula

$$L_{int} = \int \mathcal{L} dt. \tag{3.3.3}$$

We can finally calculate the number of events (N) for integrated luminosity L_{int} for 100% efficient data taking is given by the formula

$$N = L_{int} \times \sigma, \tag{3.3.4}$$

where σ is the cross-section of the process, which gives the probability of the occurrence of the particular process.

3.4 High Luminosity LHC

Since the operations of research activities started in the spring of 2009 at the LHC, it has undergone several upgrades along the way. There has been two operational runs completed at the LHC; Run 1 between 2009 and 2012, and Run 2 between 2015 and 2018. The operations were performed at the centre-of-mass energies 7 TeV and 8 TeV yielding data of 5.61 $\text{fb}^{-1}$and 23.3 fb^{-1} in 2011 and 2012. The LHC operated at the centre-of-mass energy of 13 TeV for Run 2 yielding 156 fb^{-1} throughout the years. Currently, the LHC has been operating Run 3 and is scheduled to run until 2025. The centre-of-mass energy was increased to 13.6 TeV, and the integrated luminosity is expected to be doubled from the Run 2. As seen in Eq. (3.3.1), the luminosity can be increased by changing the beam parameters. The LHC is expected to undergo further advancements during the third long shutdown (LS3) and initiate High Luminosity LHC (HL - LHC) commencing in 2029 [41]. The projected operating schedule of LHC is presented in Figure 3.4.1. HL - LHC is expected to operate at $\sqrt{s} = 14$ TeV and deliver 715 fb^{-1} of data during Run 4 [41]. This thesis will be based on the projected Run 4 target.

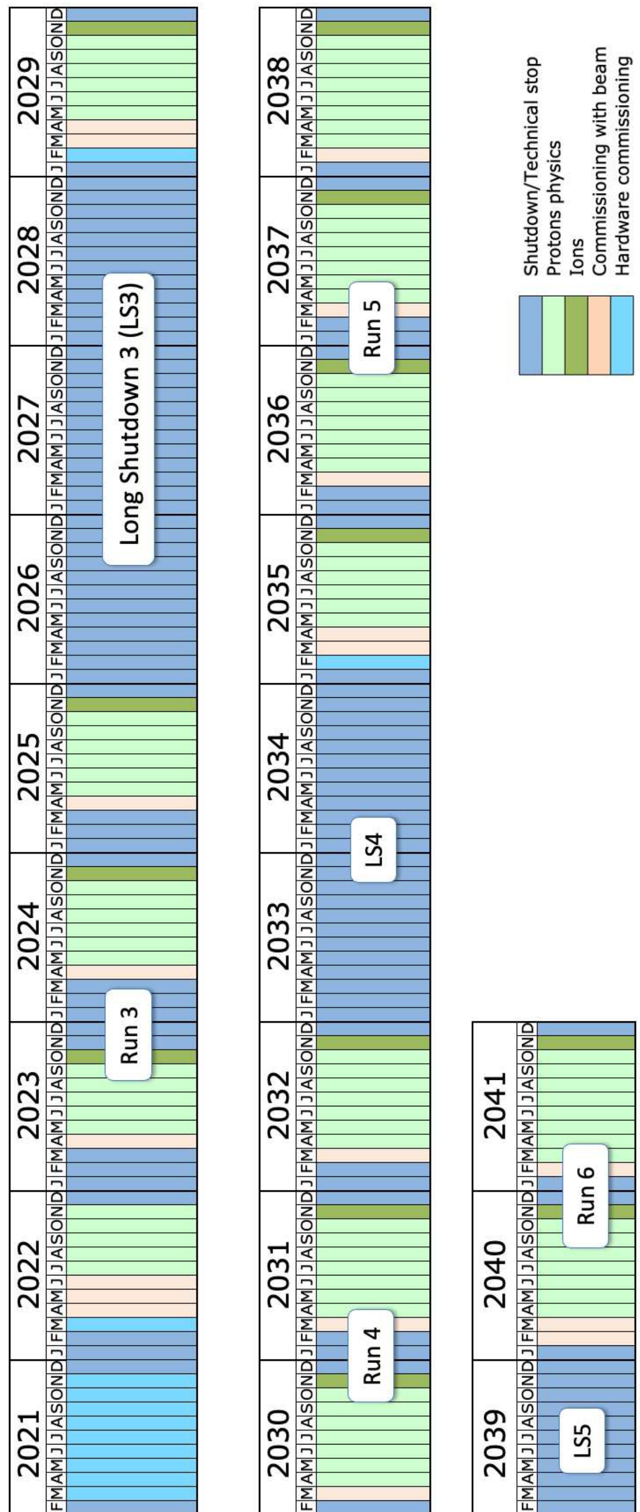

Figure 3.4.1: The projected LHC operating schedule [41].

3.5 The ATLAS Experiment

ATLAS is a multi-purpose detector which is situated at Point 1 in the LHC ring as shown in Figure 3.1.1. The detector exhibits cylindrical symmetry around the beam axis and also demonstrates symmetry in a forward-backward direction with respect to the interaction point (IP), effectively covering almost the entire 4π solid angle around the IP. ATLAS is an enormous scientific experiment, with a length of 44 meters, a diameter of 25 meters, and a total mass of approximately 7000 tons [42] as shown in Figure 3.5.1.

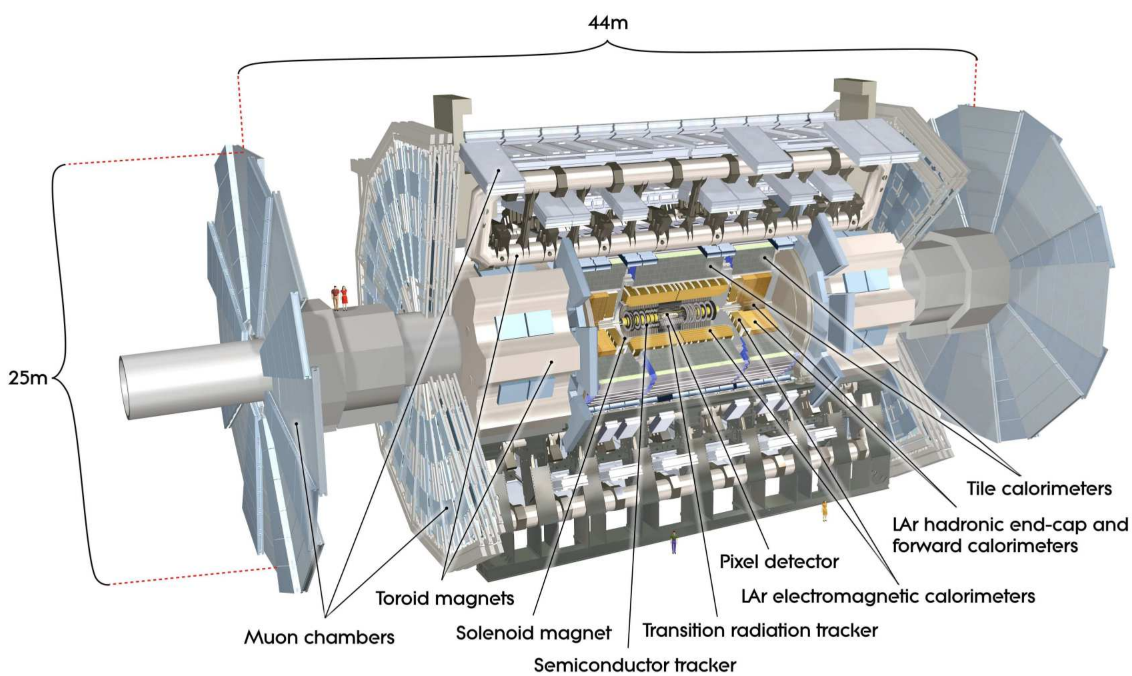

Figure 3.5.1: A cut-away view of the ATLAS detector with the sub-detectors labelled [42].

The technical details of the ATLAS detector can be found in [43, 44, 45, 46, 47, 48]. The structure of the detector comprises concentric cylindrical sub-detectors that envelop the IP. These sub-detectors are arranged in layers around the IP and extend into two end cap structures where they form disk-shaped layers. This design is necessary because proton-proton interactions in the LHC occur without a preferred direction transverse to the beam line, requiring the detector to cover all potential particle flight directions.

The innermost component of the detector, known as the Inner Detector (ID), plays a crucial role in reconstructing the trajectories of charged particles and determining their positions relative to the IP. The ID resides within a cylindrical enclosure, with dimensions of 7.02 m in length and a radius of 1.15 m [44]. It is surrounded by a 2 T axial magnetic field generated by a solenoid magnet. The ID measures the momentum of these particles by observing the curvature of their paths in the magnetic field. It is made of three distinct sub-detectors, namely the Pixel Detector, the Semiconductor Tracker (SCT), and the Transition Radiation Tracker (TRT), the ID's structure is visually depicted in Figure 3.5.2.

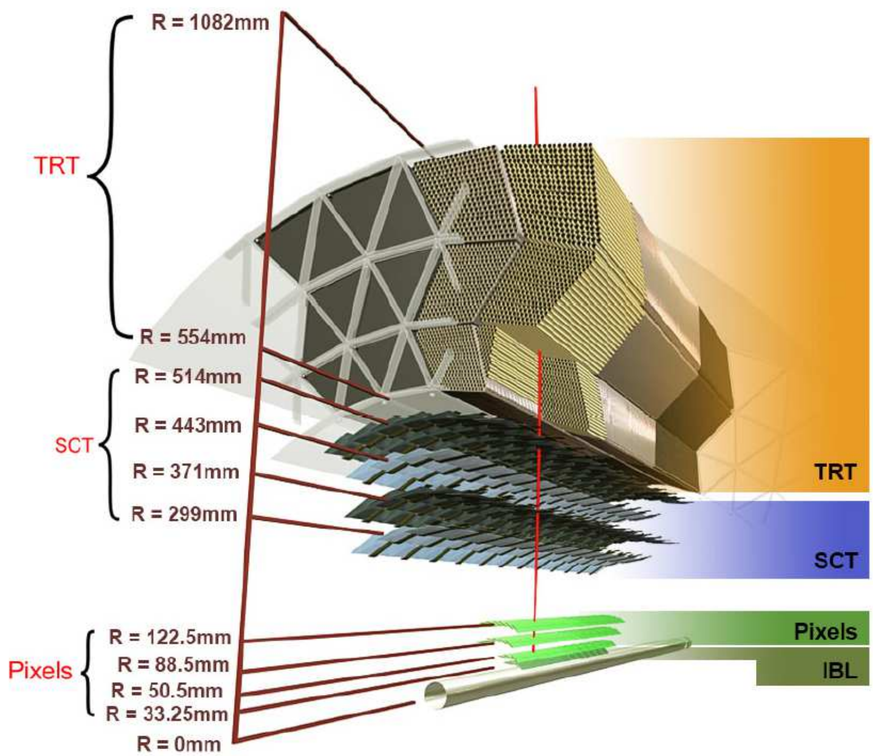

Figure 3.5.2: ATLAS inner detector sketch cutaway view depicting the 3 main regions with the distances to the interaction point [49].

Beyond the solenoid, there is the calorimeter system, consisting of an electromagnetic subsystem (ECAL) and a hadronic subsystem (HCAL). These calorimeters serve as effective energy absorbers for the majority of particles emerging from collisions, compelling them to deposit their energy and ultimately come to a halt within the detector. The ECAL is designed to identify electromagnetic showers, while the HCAL measures the energy of jets and missing transverse momentum. The technical report on the calorimetry can be found in [48]. Figure 3.5.3 provides a visual representation of the layout of these distinct calorimeter sections.

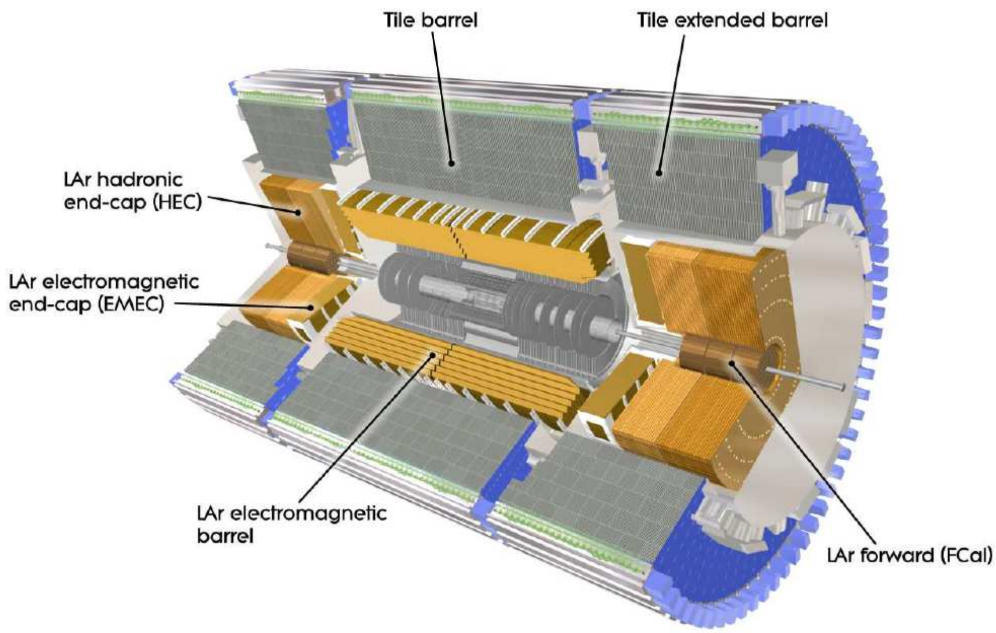

Figure 3.5.3: A diagram depicting the ATLAS calorimeter sections [50].

The outermost sub-detector, the Muon Spectrometer (MS), is responsible for identifying muons and measuring their momentum. This system is situated both inside and around a set of toroidal magnets, ensuring precise muon momentum measurements. Muons, distinct for their penetrating nature and minimal interaction via the strong force, requires dedicated detection. Positioned around the calorimeters, the MS employs gaseous radiation detectors, segmented into 16 parts, organized as precision and trigger chambers. Precision chambers, encompassing Monitored Drift Tube (MDT) and Cathode Strip Chamber (CSC) detectors, ensure precise muon track measurement within the MS [47]. These chambers provide accurate determination of muon momenta through curvature measurement. The specific regions covered by the various components of the muon spectrometer is shown in Figure 3.5.4.

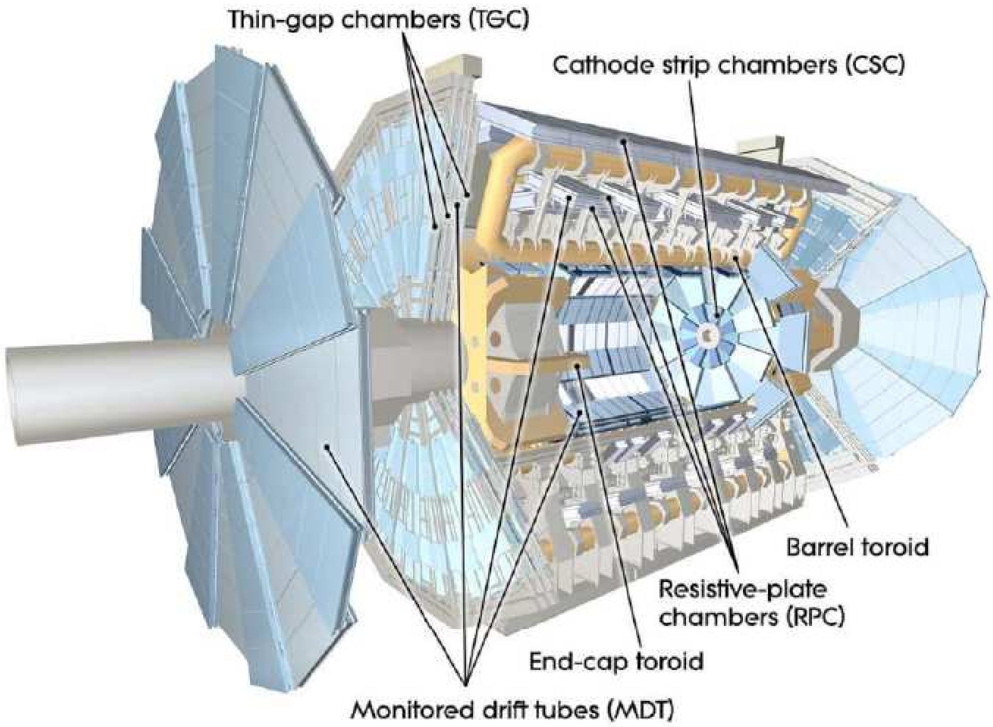

Figure 3.5.4: A cutaway diagram showing the sub-sections of the ATLAS muon spectrometer [42].

Additionally, the ATLAS detector incorporates sub-detectors designed specifically for luminosity measurement. The ATLAS detector is described using a right-handed coordinate system. In this system, the z-axis runs along the beam line, the x-axis points toward the centre of the LHC ring, and the y-axis points vertically upward. The azimuthal angle, denoted as ϕ, ranges from $-\pi$ to π and begins from the x-axis. The polar angle θ covers the interval $[0, \pi]$, although it is often substituted with the pseudorapidity (η) as the particle flow is approximately uniform per unit in η [51]. It is defined as

$$\eta = -ln(tan(\theta/2)). \tag{3.5.1}$$

The ATLAS experiment employs a sophisticated magnet system to enable the detection and analysis of charged particles, maintained at an operating temperature of approximately 4.5 K [52]. When charged particles move through a magnetic field, the Lorentz force causes them to follow a curved trajectory. This curvature depends on the particle's momentum and the magnetic field strength given by the formula

$$p_T = qBr, \tag{3.5.2}$$

where p_T represents the transverse momentum of the particle, q is its charge, B is the magnetic field, and r is the bending radius.

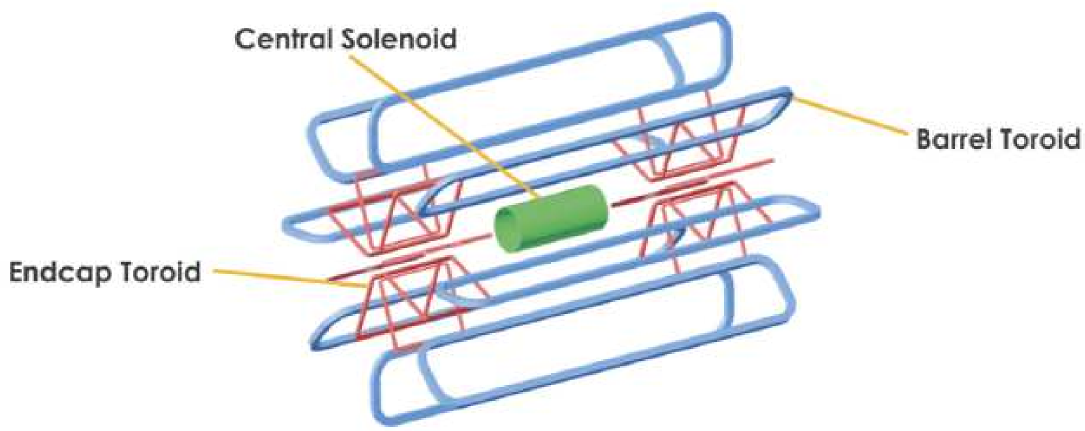

Figure 3.5.5: A diagrammatic representation of the ATLAS magnetic system [52].

The ATLAS magnet system, depicted in Figure 3.5.5, consists of four superconducting magnets: an inner solenoid, a barrel toroid, and two end-cap toroids, all cooled with liquid helium. Field sensors map this complex magnetic field structure to accurately measure and analyze the particle paths and momenta.

The LHC operates at a high collision frequency of 40 MHz during its operational cycle. Each collision event generates roughly 1.5 MB of data. This would lead to an enormous data rate of around 60 TB/s if every event were recorded. Handling such a massive volume of data is not only technically challenging but also unnecessary for scientific research. Most collision events fall under the category of soft parton scattering, lacking significant physics phenomena that needs detailed study. To address these challenges, the ATLAS experiment employs a system called the trigger to selectively identify and store potentially interesting events. The goal is to reduce the data rate to a manageable level for further analysis.The ATLAS trigger system comprises two levels: the Level 1 (L1) trigger and the High-Level Trigger (HLT). The L1 trigger is a hardware-based system that rapidly screens collision data, making a preliminary event filtering decision within 2.5 μs of the bunch crossing.

The primary role of the L1 trigger is to identify events involving high p_T leptons, photons, jets, significant total or missing transverse energy, and events originating at the interaction point. It does this by defining Regions of Interest (RoI) in the detector where unusual or intriguing features have been detected. The central trigger processor (CTP) handles the L1 trigger's decision-making process and can apply prescaling to reduce the event rate from 40 MHz to a target rate of 100 kHz.

Events selected by the L1 trigger are then passed to the HLT, a software-based system that performs more detailed data filtering by reconstructing physics objects in greater detail. It utilizes all available detector data within the RoIs identified by the L1 system, operating at full granularity and precision. The HLT substantially reduces the event rate to approximately 1 kHz, saving roughly one out of every $40,000$ collision events. The detailed description on the ATLAS trigger system is found in [53]. Further information on the ATLAS track reconstruction process can be found in [54].

Chapter 4

Auxiliary Detector above the ATLAS Muon spectrometer

As discussed in §2.4, one of the common features of many BSM theories is the existence of LLPs. However, the design of general-purpose particle physics detectors like ATLAS, is tailored towards the detection of promptly-produced particles with shorter lifetimes. Most neutral LLP species either possess considerable mass or exhibit weak interactions, rendering them challenging to observe directly in this manner. Consequently, the primary method for directly detecting these neutral LLPs is through the observation of their decay. In numerous theoretical frameworks [9], LLPs not only decay into observable products but also interact with other heavy SM or BSM particles.

The HL - LHC emerges as an invaluable tool offering both the requisite energy reach and luminosity to investigate potentially rare LLP signals. Nevertheless, the general-purpose LHC detectors have inherent limitations that curtail their effectiveness in probing very long-lived neutral particles. While LLP decays can manifest as striking signals, the high-rate environment at the HL - LHC poses challenges, with substantial QCD backgrounds and triggering constraints acting as significant obstacles for many LLP searches.

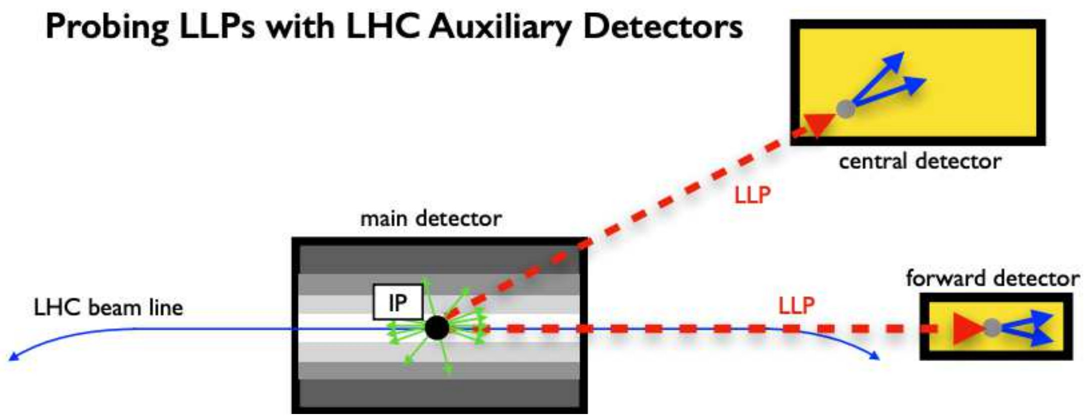

Figure 4.0.1: Basic idea for auxiliary detectors (Image credit: Brian Batell)

To comprehensively explore all plausible avenues for BSM physics, it would be highly advantageous to combine the energy reach of an energy frontier experiment with the shielding and detection capabilities of a dedicated long-lived particle detector. Such detectors are usually placed separate from any existing LHC detector at a large distance from the interaction point. An ideal LLP detector would effectively shield against QCD backgrounds generated in LHC collisions while simultaneously offering ample size and proximity to ensure sufficient acceptance for LLP decay products. The idea is to harness the primary high-energy proton-proton collisions at the LHC as the primary source of LLPs production. Then the reach of the main detectors can be significantly expanded by positioning a detector in close proximity to the interaction point to capture them as explained in Figure 4.0.1. Several dedicated detectors tailored specifically for LLP detection have been proposed, with some already operational at the LHC [55].

4.1 The Proposed ADAM Detector

The Auxiliary Detector above the ATLAS Muon spectrometer (ADAM) is a proposed particle detector to extend the physics reach of the ATLAS experiment. Its primary function is to detect the decay products of BSM particles, which evade detection by the ATLAS

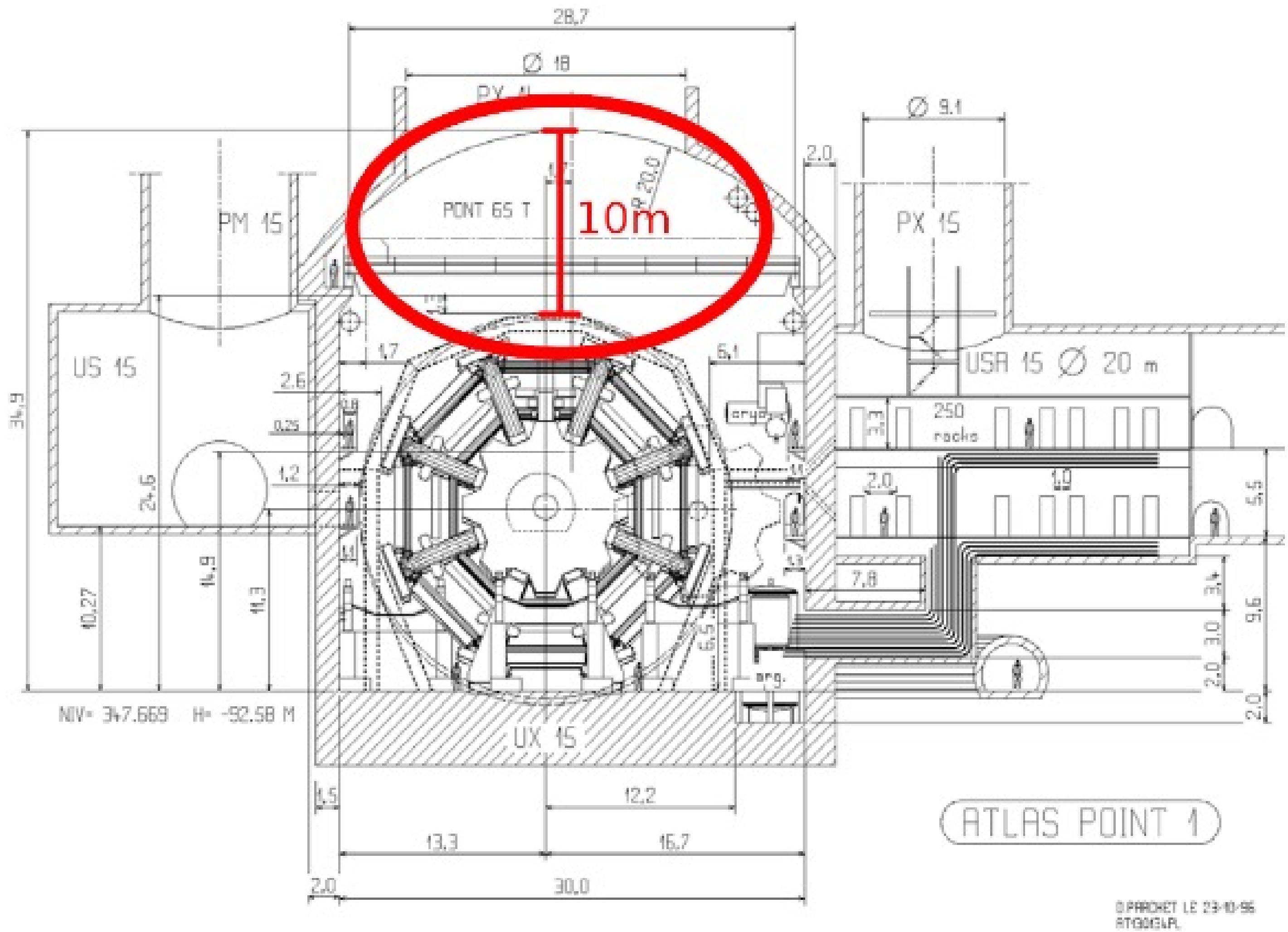

Figure 4.1.1: Schematic view of the underground ATLAS installation with the empty space in the upper cavern marked in red. The detector cavern is UX15, the adjacent caverns are USA15 and US15. PX14 and PX16 are the installation shafts for surface access, PM15 and PX15 are the two elevators [56].

experiment in such collisions. It is a low-cost addition to the existing infrastructure at the LHC that can extend the physics reach of such experiments. Being in close proximity of the ATLAS detector, ADAM can also benefit from its triggering capabilities in detecting the LLPs. The ADAM detector would be placed on top of the ATLAS detector utilizing the empty space in the ATLAS upper cavern. The schematic view of the underground ATLAS detector blueprint is shown in Figure 4.1.1 [56].

The ATLAS detector layout and its components were discussed in §3.5. The ATLAS collaboration maintains comprehensive databases of the detector geometry in the form of SQL-lite databases [57]. The database labeled "$geometry - ATLAS - R3S - 2021 - 03 - 02 - 00$" can be used for the simulation of particles that interacts with the ATLAS detector components. The modeling task of the geometry is executed using the Geant4 toolkit [11], renowned for its ability to simulate particle trajectories through matter and established as the standard for high-energy physics detector simulation.

However, Geant4 lacks a built-in capability to read the ATLAS geometry database file. FullSimLight tool can be employed to construct a Geant4 simulation using the database [58]. FullSimLight is a submodule of the GeoModel suite of tools [59], which is utilized by the ATLAS collaboration. It also allows the incorporation of the ATLAS magnetic field map and any Geant4 functionalities through user-defined "plug-ins". These tools are significant in the simulation that involves the modeling of the passage of a particle through the components that makes up the ATLAS detector. To create the simulation of ADAM with ATLAS, a Geometry Description Markup Language (GDML) file is generated to encompass measurements of individual panels within the detector, their spatial placement, and the materials they are composed of. This GDML file is then converted into an SQL-Lite database and integrated with the official ATLAS geometry using tools in the GeoModel toolkit. The detector geometry is illustrated in Figure 4.1.2. The ADAM detector consists of two regions, each containing three 12.5 mm thick planes of plastic scintillator spaced 30 cm apart. The first region of the ADAM detector is situated closest to the ATLAS detector at a radius ranging from 13.0 to 13.6 m (measured from the panel centre), consisting of three subregions, each 7.2 m in width. One of these subregions is normal with the y-axis, while the other two are positioned at -36 degrees with respect to the previous one.

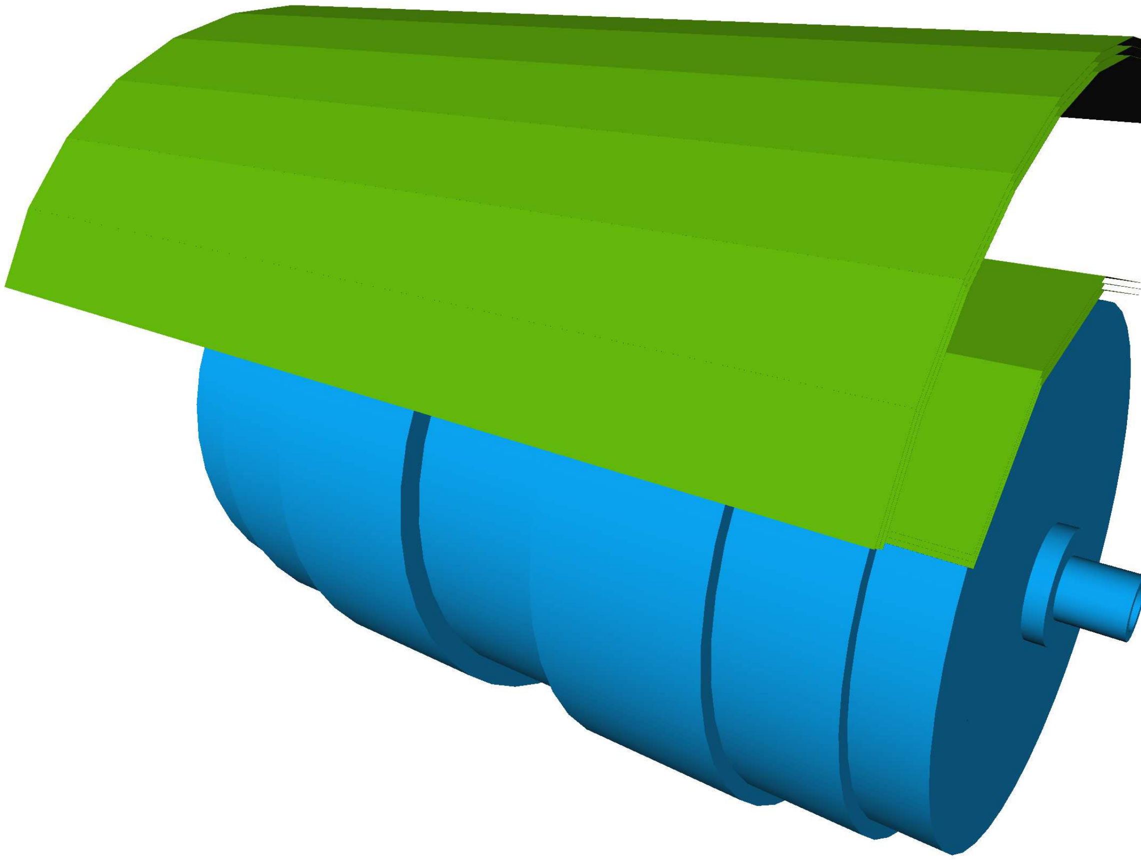

Figure 4.1.2: A simple $3-D$ model of the ADAM detector as a panel structure on top of the ATLAS detector in GeoModel Explorer.

The second region is mounted on the ATLAS cavern ceiling, occupying a radius from 22.9 to 23.5 m. It comprises nine subregions, each with a width ranging from 3.8 to 3.9 m. The centre region is normal with the y-axis, and each successive flanking panel is positioned at -11.25 degrees relative to the previous one. All the panel subregions have a length of 45.0 m in the z direction, resulting in a total area of ~ 7612 m^2. Importantly, this two-region setup creates a substantial decay volume of approximately $\sim 12,000$ m^3 (see Appendix C), which will be used for studying the LLPs decaying in flight. A detailed view of the three-layer structure with CAD rendering is presented in Figure 4.1.3.

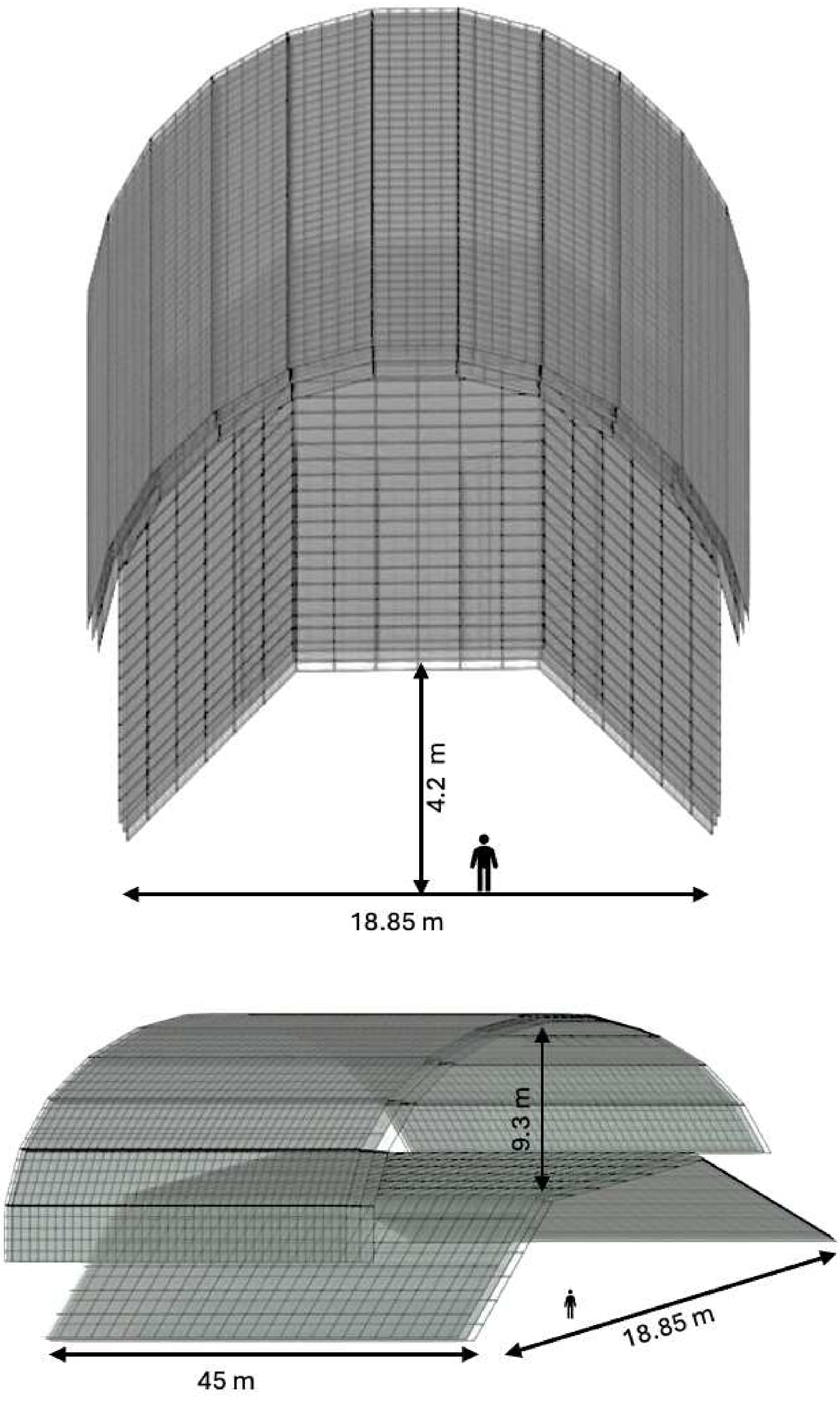

Figure 4.1.3: Simple CAD rendering of the ADAM geometry layout.

For particles traveling at nearly the speed of light through the panels, it takes roughly 1 ns to traverse the 30 cm panel spacing. This timing resolution can be achieved with Silicon Photomultipliers (SiPMs), enabling directional tracking by measuring the time difference between hits on the three panels. This capability allows for the differentiation of upwards-going tracks originating in ATLAS from downward-going tracks caused by cosmic rays. Additionally, it provides the opportunity to measure cosmic muon signals, serving as a secondary use case for ADAM. Last, but not least, ADAM provides an ability to trigger on cosmic muons that can be used to identify possible cosmic backgrounds to physics from $p-p$ interactions.

Joseph Mitchell Kelly simulated ADAM as a sensitive detector with simple panel structures to detect the decays of very long-lived stau particles produced in 14 TeV $p-p$ collisions which are trapped in the ATLAS detector material [60]. In the scope of this thesis, a simulation of individual ADAM detector module configuration is performed to estimate the spatial resolution using SiPM readout to measure tracks traversing the detector using $GEANT4$. The simulation of DHBs production using the Monte Carlo (MC) event generator $Pythia8$ [10] is performed at the ATLAS experiment and their subsequent detection of decay products in the proposed ADAM detector.

4.2 Preliminary Discussion of Backgrounds

The study of potential background sources is crucial for particle detector experiments. The inner layer of ADAM is designed to use as a veto layer for particles penetrating the ATLAS detector and reaching ADAM. The inner and outer layer of ADAM can also effectively identify the cosmic muons coming from above. The underground placement of ADAM detector provides significant shielding from cosmic ray backgrounds. However there are still some sources of background that can be expected to reach the ADAM detector, such as higher energy cosmic muons. While not studied in the current scope of the thesis, a detailed study of the potential background sources is planned for the future. The study of cosmic muons expected to reach ADAM will be performed using the EXcel-based Program for calculating Atmospheric Cosmic-ray Spectrum (EXPACS) which uses the PHITS-based Analytical Radiation Model in the Atmosphere (PARMA) [61].

There are also expected backgrounds from long-lived SM particles, such as K_L^0, primary and secondary neutrons, and muons produced during the collisions at the IP. The generation of these IP fluxes that reach ADAM will be achieved by performing detailed $Pythia8$ simulations. Another source of background is the beam induced backgrounds, which are caused by proton energy losses, collisions with residual gas inside the beam pipe, and the production of secondary particles due to interaction with collimators [62]. A detailed simulation of these beam induced backgrounds will be performed using MC simulation package like $GEANT4$ or FLUktuierende KAskade ($FLUKA$) [63].

4.3 Detector Components

As shown in Figure 4.1.3, the ADAM detector consists of three layer structure in two regions. These structures are formed by joining small detector modules, about 1×1 m in dimensions. There are two different models, being considered for these modules as shown in Figure 4.3.1. The X-Y fibre embedded model consists of wavelength shifting (WLS) fibre pairs, embedded in both x and y direction spaced at 1 cm with SiPM readouts at the ends as shown in Figure 4.3.1a. By selecting the strongest signals from any X-Y fibre pairs, it is possible to determine that the incident particle traveled closest to this fibre pair, providing roughly 1 cm resolution or better. The plug model consists of SiPM coupled with WLS fibres mounted vertically on the scintillating panel as plugs as shown in Figure 4.3.1b. With the plug model, it is also possible to measure tracks traversing the detector using squared charge centroiding technique based on the charge output in the individual SiPMs.

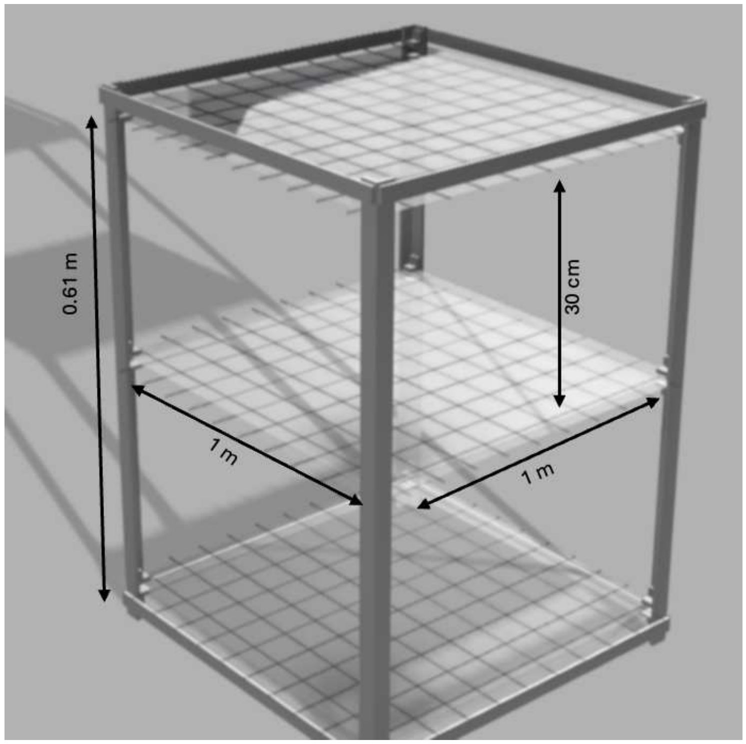

(a) Embedded X-Y WLS fibre with SiPM readouts at the ends.

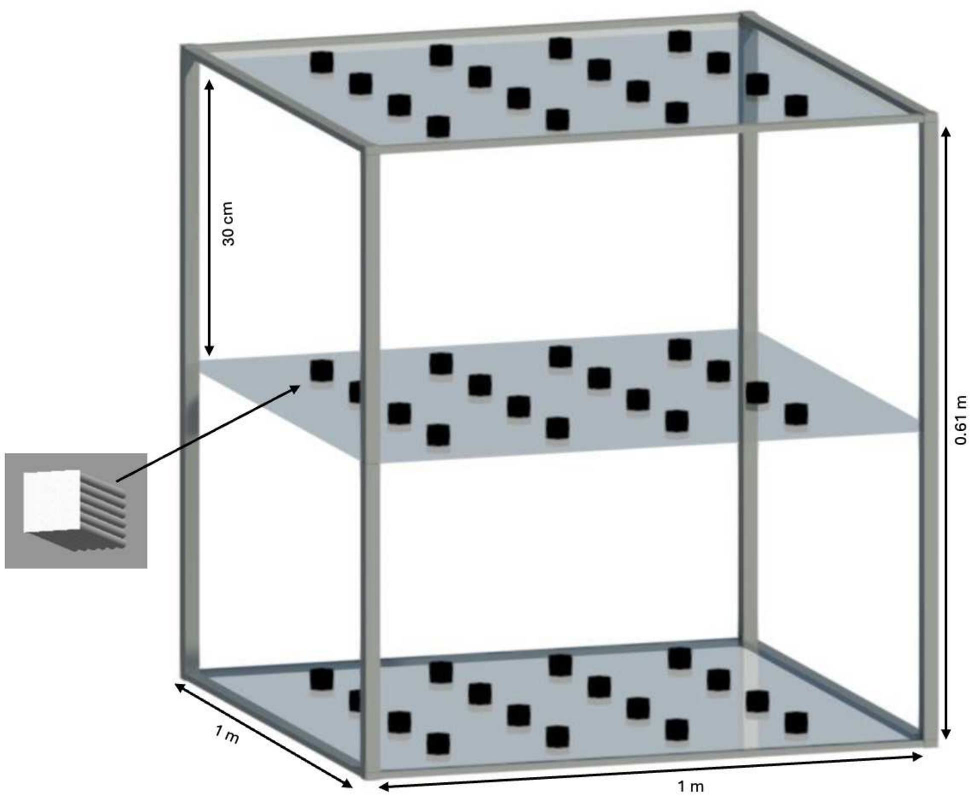

(b) SiPM plugs with WLS fibres on the scintillating panels.

Figure 4.3.1: Proposed ADAM detector modules.

The design of the detector depends critically on several factors, including the type of particles to be detected, the environment in which the detector operates , appropriate material or component combinations, geometrical restrictions, and costs. The behavior of a particle traversing through the detector material is crucial in considering a particle detector. Various physical processes govern the particle interactions with matter, such as elastic scattering, inelastic scattering with atomic electrons, bremsstrahlung emission, Cherenkov radiation emission, and nuclear interactions. Now, we will discuss the working mechanism of the optical detector elements that are part of the proposed ADAM detector modules. More detail descriptions of these detector elements can be found in [5] (Particle Detectors at Accelerators).

4.3.1 Scintillating Panels

Scintillators have been employed extensively in the detection of charged particles over an extended period. When charged particles traverse scintillating materials, they deposit energy, causing electrons to become excited to higher energy states. Subsequently, these molecules return to their ground states, releasing the stored energy in the form of light. Organic scintillators, characterized by their carbon ring structure, are notable for their short decay time of excited electronic states, rendering them well-suited for scintillation purposes. It utilizes ionization induced by charged particles to generate optical photons, typically in the blue to green wavelength regions [64]. Techniques to direct light towards the photon-electron converter, such as diffusive paint, reflectors, photonic crystals, or light guides, may be necessary to enhance light yield. Organic scintillators have found widespread application in various detectors [5], with plastic scintillators being particularly favoured due to their ease of fabrication into desired shapes and low cost, making them ideal for large detectors. The decay times of organic scintillators typically range from a few nanoseconds, with even shorter rise times [65]. Because of these properties, they offer excellent time resolution and are sufficiently rapid for applications with high event rates.

4.3.2 Wavelength Shifting (WLS) Fibres

A common method for extracting photons from a scintillator is by using WLS fibres connected to the scintillator. WLS materials absorb photons within a specific wavelength spectrum and emit new photons with higher wavelengths. These materials are typically organic and ideally sensitive to the scintillation light. WLS fibres are primarily employed for light collection in other optical detector components, such as scintillator tiles. In this process, the scintillation light is absorbed by the WLS fibre, re-emitted isotropically (with a longer wavelength), and captured within the fibre. The light captured within the scintillating or WLS fibre can then be directly transported to a photodetector or coupled into a light-guiding fibre for transport over longer distances. These fibres typically comprise a core and one or two claddings, as well as an absorbing coating if required. The materials used for these components are selected to ensure that the refractive index decreases from the core to the outer edge, enabling the capture of light inside the fibre through total internal reflection.

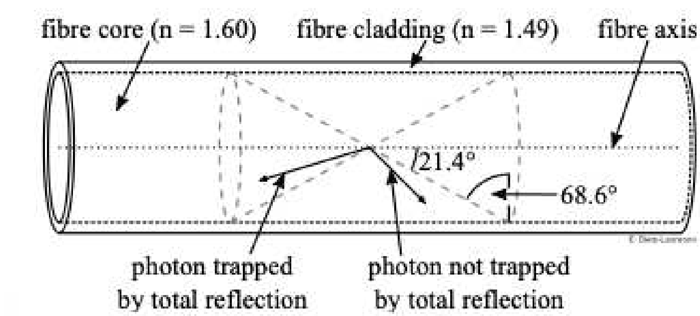

Figure 4.3.2: Sketch of the WLS fibre working mechanism [66].

4.3.3 Silicon Photomultiplier (SiPM)

A SiPM is a pixelated device where each pixel (or microcell) is a series combination of an Geiger-mode Avalanche Photodiode (GAPD) and a quenching resistor as shown in Figure 4.3.3. The APD, either structured like a pin-diode operated near breakdown voltage or with a specialized avalanche structure, amplifies signals by inducing an electron avalanche with a high external voltage.

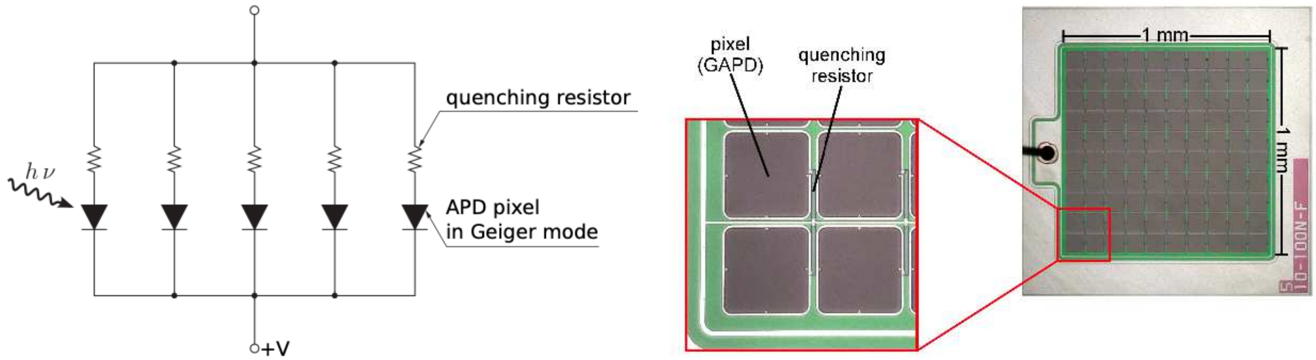

(a) Schematic circuit diagram (b) SiPM microscopic picture

Figure 4.3.3: Schematic diagram of SiPM [67].

When incoming photons are absorbed in the GAPD, they create an electron, triggering an avalanche. Many properties of the SiPM depend on the over-voltage (ΔV), which is the excess of the bias-voltage (V_{bias}) over the breakdown-voltage (V_{br}) of the GAPDs. The breakdown voltage (V_{br}) is the bias point at which the electric field strength generated in the depletion region is sufficient to create a Geiger discharge. SiPM sensors are typically operated at a bias point that is typically $10-25\%$ higher than the V_{br} [68]. Thus, V_{bias} to apply is calculated using the formula

$$V_{bias} = V_{br} + \Delta V, \tag{4.3.1}$$

where V_{br} depends approximately linearly on temperature within a small range. The gain of an SiPM sensor, defined as the charge created per detected photon, depends on the over voltage and microcell size. The gain can be calculated from ΔV, the microcell capacitance C, and the electron charge, q as

$$G = \frac{C \times \Delta V}{q}. \tag{4.3.2}$$

Due to the SiPM's structure, each microcell needs separation from its neighbor for optical and electrical isolation, along with space for the quench resistor and signal tracks, resulting in a "dead space" around the microcell. The photon detection efficiency (PDE) is a crucial photodetector property, representing the probability of an incident photon interacting with a microcell to trigger an avalanche defined as [68]:

$$PDE(\lambda) = QE(\lambda) \times F_{geom} \times \epsilon_{trig}, \tag{4.3.3}$$

where $QE(\lambda)$ is the probability to create primary electron-hole pair as a function of wavelength λ, F_{geom} is the geometrical fill factor (SiPM surface that is sensitive to incoming light), and ϵ_{trig} is the probability that the primary electron-hole pair initiates an avalanche. GAPDs can achieve gains of up to 10^8, enabling single photon detection covering wavelengths from 300 nm to 1700 nm, with a PDE of up to $\sim$ 70 % [69]. The total signal depends on the number of cells breaking down simultaneously, along with the recharge characteristics of the cells given by [69]

$$N_{fired}(N_\gamma, N_{total}, U, \lambda) = N_{total}\left(1 - \exp\left(-\frac{PDE(U,\lambda) \times N_\lambda}{N_{total}}\right)\right), \tag{4.3.4}$$

where U is the external voltage, λ is the photon wavelength, $N_{total}$is the total number of cells, N_γ is the number of incident photons, and N_{fired} is the total number of cells that has been fired. The sensor output is a photocurrent, and the total charge Q generated from an event is given by [68]

$$Q = N_{fired} \times G \times q, \tag{4.3.5}$$

where N_{fired} is given by Eq. (4.3.4).

Chapter 5

The $GEANT4$ Simulation of the ADAM Detector Module

Simulation frameworks that accurately model particle-matter interactions are indispensable tools in detector design. Several dedicated and versatile simulation tools are available, with $GEANT4$ being a prominent example. Its extensive and adaptable optical physics simulation capabilities make it a valuable asset for research in this field. In this thesis, $GEANT4$ will be utilized in the simulation of the proposed ADAM detector module.

5.1 Overview

$GEANT4$ [11], Geometry and Tracking, is a versatile toolkit for simulating particle interactions with matter using Monte Carlo methods. Developed at CERN, it serves as the foundation for detector simulation frameworks in experiments like the LHC. Its broad physics range, object-oriented design, and modular structure make it highly flexible, applicable not only in particle physics but also in fields like medical physics, materials science, and space radiation studies [70]. $GEANT4$'s capabilities extend to simulating optical detector components with precision. The C++ framework allows for standalone simulations or integration into other applications, providing methods to define detector geometries, simulate particle creation and tracking, and access data on particles and interactions. With various physical interaction models, it covers a wide energy range of particles such as electrons, muons, pions, protons and heavy ions as well as neutrals like neutrons and photons. Visualization of detector parts and particle trajectories is also supported. A basic workflow for $GEANT4$ simulation can be found Appendix E. Further details on $GEANT4$ can be found in the official CERN documentation [70].

5.2 ADAM Detector Module Simulation

As discussed in §4.3, the feasibility of the proposed ADAM detector modules are to be tested.. The thesis will focus on assessing the feasibility of the plug model as it involves the use of the squared charge centroiding technique. This setup may offer a cost-effective alternative to the X-Y fibre embedded model, requiring fewer readout electronics, WLS fibres, and machining costs. $GEANT4$ simulation was employed to simulate and test various setups for the plug model with a simple arrangement of SiPM plugs in a square grid, as illustrated in Figure 5.2.1. As described in §4.3, this detector module consists of 3 major component:

- Scintillating Panel
- Wavelength Shifting Fibres
- Silicon Photomultipliers

An essential aspect to consider when working with optical photons is their interaction at surface boundaries. Optical photons can undergo reflection or refraction at these boundaries. Simulating wrapping involves creating a volume with the inner part removed, representing the wrapping material as a shell. This allows for the application of reflection properties. Tyvek wrapping was used as reflective material at the surface boundary of scintillating panels to reflect optical photons back. In the following sections, each simulated component is discussed. Materials appropriate for the research were chosen based on manufacturer specifications.

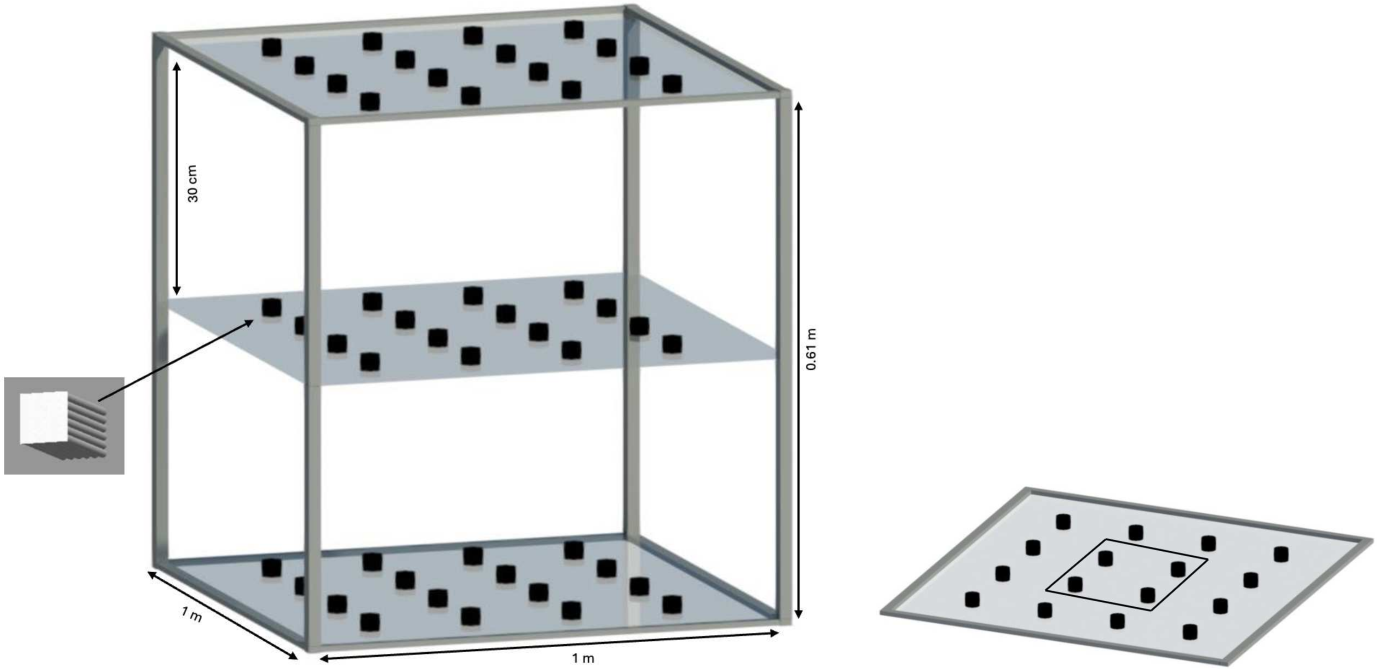

(a) Sketch of the test module (b) Square Grid to be tested for simulation

Figure 5.2.1: Setup model for the $GEANT4$ simulation

5.2.1 Scintillating Panel

The simulation utilized the Saint Gobain BC-408 model for the scintillating panel. The emission spectra for this model are illustrated in Figure 5.2.2. Below are the key properties of the scintillating panel obtained from the manufacturer [71]:

- Decay time (ns) = 2.1: After absorbing energy from incident radiation and undergoing excitation, the panel emits light as it returns to its ground state. This emitted light then decays over time, characterizing the decay rate. The decay time represents the duration for the scintillation light intensity to decrease to $\frac{1}{e}$(approximately 36.8%) of its initial intensity.

- Refractive index (n) = 1.58 : The refractive index of a material indicates the extent to which light slows down when traversing the material in comparison to its velocity in a vacuum.

- Density (g/cc) = 1.032: The density of the material.

- Wavelength of Maximum Emission (nm) = 425: The scintillating panel converts incident radiation or energy deposition with optimal efficiency into scintillation light at the designated wavelength.

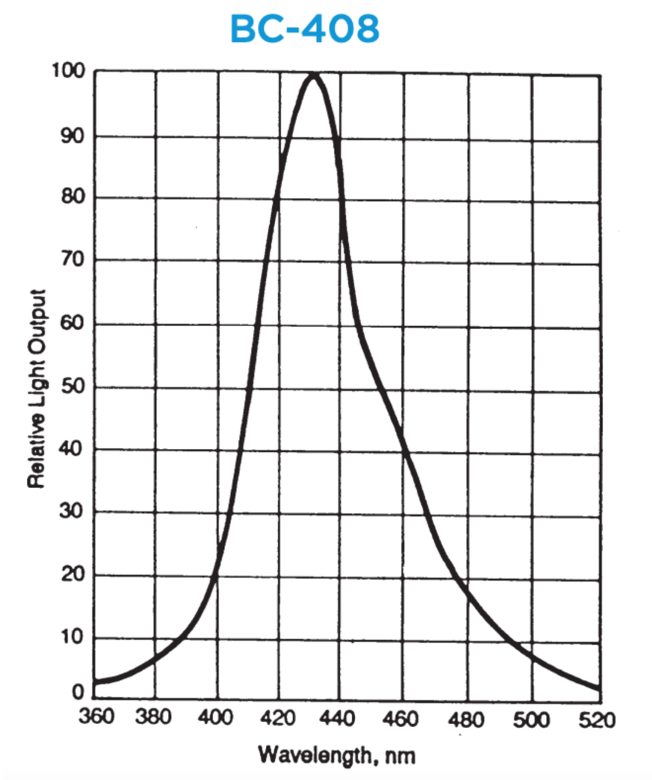

Figure 5.2.2: Emission Spectra of the Saint Gobain BC-408 panel [71].

5.2.2 Wavelength Shifting (WLS) Fibres

The simulation utilized the Kuraray Y11(200) MS multi-clad model for the WLS fibre, based on the manufacturer's data sheet [72]. The absorption length, representing the mean distance an optical photon travels before undergoing the WLS process, is depicted at various wavelengths in Figure 5.2.3a. Additionally, the emission and absorption spectra at various wavelengths are shown in Figure 5.2.3b. The properties of the model used in the simulation are listed as follows [72]:

- WLSTimeConstant(ns) = 6.9: Wavelength shifting involves the absorption of photons at one wavelength and the subsequent re-emission of photons at a longer wavelength.

The WLS time constant represents the time it takes for the wavelength shifting process to occur.

- Refractive index = 1.56(core), 1.49(inner), 1.42(outer): Refractive indices of the core and the inner and outer cladding.
- Absorption peak wavelength (nm) = 430: The absorption peak wavelength for a WLS fibre refers to the specific wavelength of light at which the fibre's core material exhibits maximum absorption.
- Emission peak wavelength(nm) = 476: The emission peak wavelength for a WLS fibre refers to the specific wavelength of light at which the fibre's core material exhibits maximum emission.

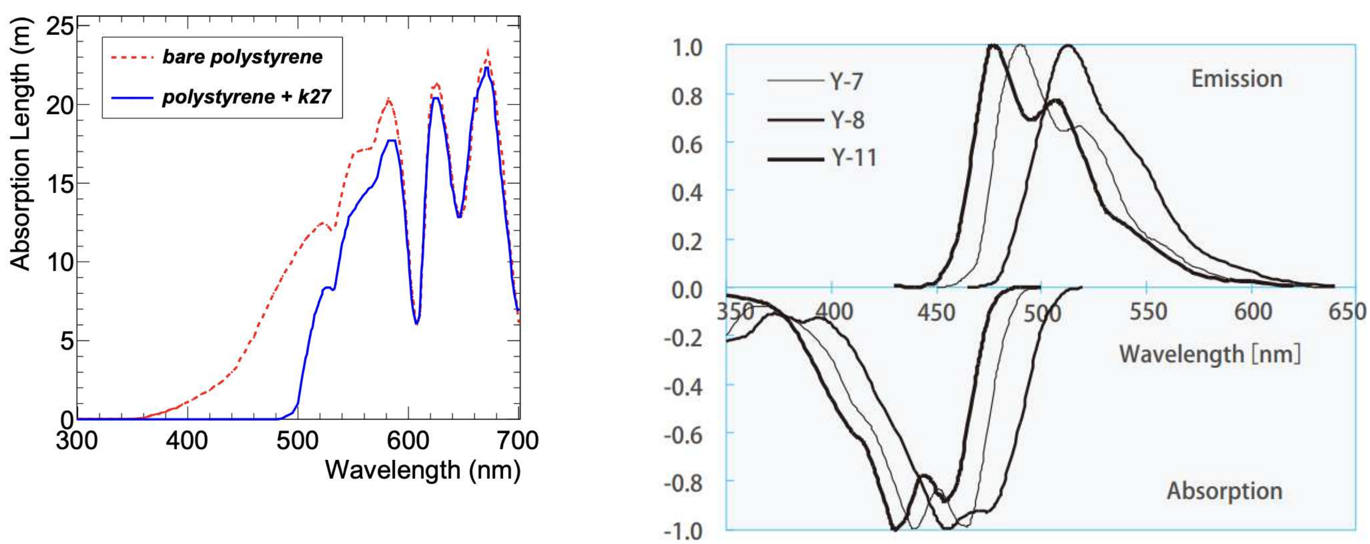

(a) Absorption Length [73]

(b) Absorption and Emission Spectra [72]

Figure 5.2.3: Properties of the Kurary Y-11 model.

5.2.3 SiPM

For our simulation of the SiPM, we will use the properties of the Hamamatsu $S14160-6050HS$ model. The specifications based on the manufacturer's data sheet is presented in

Table 5.2.1 and the $PDE(\lambda)$ for this model at $T = 25\ ^{o}$C is shown in Figure 5.2.4.

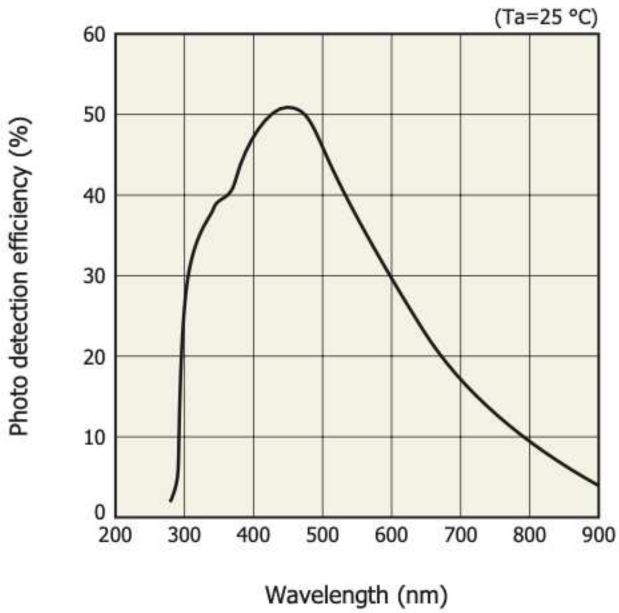

Figure 5.2.4: PDE for Hamamatsu $S14160-6050HS$ model [68].

Table 5.2.1: Electrical and Optical Characteristics ($T = 25^{o}$C and $\Delta V = 2.7$V) [68].

Breakdown Voltage(V_{br})	38 V
Recommended Operating Voltage	$V_{br} + 2.7$ V
Gain	2.5×10^{6}
Terminal Capacitance	900 pF
Sensitive Area	6×6 mm
Number of Pixels	14331

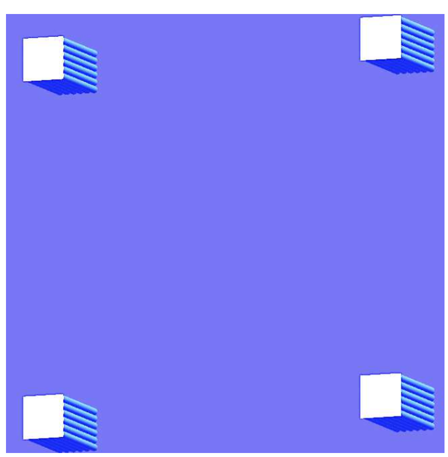

Figure 5.2.5: $GEANT4$ Simulation Model as viewed in OpenGl.

For our SiPM simulation as a sensitive detector, we will utilize these properties at a constant temperature ($T = 25\ ^{o}$C), and a constant ΔV . This approach allows us to estimate the number of photons reaching the SiPM based on the PDE. The total number of cells fired can now be estimated using Eq.(4.3.4) and the total charge output using Eq.(4.3.5) (assuming photons are reaching at normal angles). The visualization of the $GEANT4$ simulation Model is shown in the Figure 5.2.5. As discussed in §E.3, a 4 GeV muon will be shot into the square grid from the particle gun at a distance of 4 cm to initialize the run.

Chapter 6

Spatial Resolution Using SiPM Readout

The aim of this study is to evaluate the feasibility of the proposed detector modules for use in the ADAM detector, focusing on intrinsic spatial resolution and its dependence on key detector parameters (such as scintillator thickness and SiPM spacing). This evaluation serves as fundamental input for an initial performance (and cost) estimation. The primary motivation for employing the plug model is to determine the positioning of interaction events in the detector module based on the SiPM charge output. In the scope of this thesis, we will assess the feasibility of the plug model illustrated in Figure 5.2.5. Spatial resolution of ~ 1 cm or better is targeted for event position reconstruction in the proposed detector module. In this setup, SiPMs are vertically mounted as plugs, coupled with the WLS fibres. This configuration offers a cost-effective alternative due to reduced requirements for readout electronics, WLS fibres, and associated machining costs.

6.1 Squared-Charge Centroiding Technique

The centroid algorithm, developed by Anger in 1958, remains a fundamental principle in modern scintillation gamma cameras for imaging reconstruction [74]. These cameras utilized a phototube matrix to sample the distribution of scintillation light and generate signals proportional to the collected charge. The centroid algorithm calculates the position (X, Y) of each event by averaging the measured charge distribution, thereby determining a point in the imaging plane as seen in Figure 6.1.1. In the squared-centroiding method, the mean value of the squared charge distribution is used instead [75]. The calculation of the coordinates of the reconstructed position (r_x, r_y) for any registered event is given by [75]

$$r_k = \frac{\sum_{i=0}^{n} q_i^m r_{k,i}}{\sum_{i=0}^{n} q_i^m}, \tag{6.1.1}$$

where $m = 1$ for Anger-logic or $m = 2$ for the squared-charge centroiding technique, $k = x, y$ position of the interaction point, ($r_{x,i}$ and $r_{y,i}$) represents the x and y coordinates for photodetector i containing total charge q_i. In our simulation, with four SiPMs in a square grid, the formula can be written down as

$$(X, Y) = \frac{\sum_{i=0}^{4} q_i^2 (x_i, y_i)}{\sum_{i=0}^{4} q_i^2}, \tag{6.1.2}$$

where (X, Y) is the centroid position, (x_i, y_i) is the position of the SiPM i, and q_i is the total charge output in SiPM i.

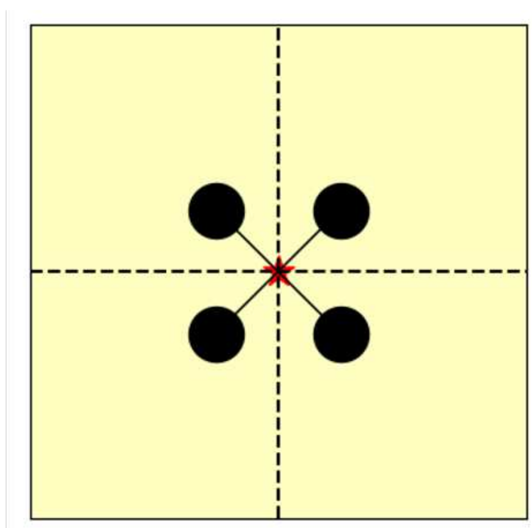

Figure 6.1.1: Sketch showing the centroiding technique.

Spatial resolution is related to the statistic uncertainty of the scintillation event position ($\sigma^2_{X_C}$), which can be written down as [76]:

$$\sigma^2_{X_C} = \frac{\sigma_{charge}}{\sqrt{n_{ph}}}, \tag{6.1.3}$$

where X_C is the centroid coordinate projected along the X-axis, σ_{charge} is the standard deviation of the charge distribution, and n_{ph} is the average number of photoelectrons. So we can define the Intrinsic Spatial Resolution (ISR) of the detector with respect to the Full Width of Half Maximum (FWHM) as [76]

$$ISR = FWHM_{PSF_{image}} = \frac{FWHM_{PSF_{light}}}{\sqrt{n_{ph}}}, \tag{6.1.4}$$

where PSF$_{light}$ is the point spread function (PSF) of a single scintillation event and PSF$_{image}$ is the PSF of many scintillation events.

6.2 Simulation Setups

Detector spatial resolution is a crucial parameter for the quality of particle (muon in our simulation) tracking and imaging results. The ISR of the detector is determined by the uncertainty in the positioning of the muon interaction points, defined as the width of the estimated interaction Point Spread Function (PSF) distribution as described by Eq.(6.1.4). Spatial coordinates (X, Y) of individual muon interaction events can be determined from the SiPM signal values (integrated light pulse charge generated by the SiPM) and their relative positions, using a simple centroid positioning algorithm [75]. The weights for the SiPM signals depend on the SiPM position within the grid. The positioning dispersion will be determined by the statistical variations in the light reaching the individual SiPMs. The light spread function (LSF) represents the spatial distribution of the number of photons detected at the readout face by the SiPMs [77]. The model parameters for the simulation was discussed in §5.2. To study the influence of the scintillator slab thickness on light production and collection, two different panel thickness were chosen. For our simulation, we will take four SiPMs arranged in a square grid as shown in Figure 5.2.5 at different scintillating panel thickness and SiPM spacings.

- Scintillating panel thickness: 1.27 cm and 2.5 cm
- SiPM spacings: 5 cm, 10 cm, 15 cm, 20 cm, and 25 cm

To obtain the PSF_{image}, 5000 scintillation events were simulated with 4 GeV muon interacting from 4 cm distance at the centre of the square grid and on the edge of the grid. The PSF_{image} was obtained as a 2D histogram based on the calculated (X, Y) positions using the centroiding algorithm as shown in Eq.(6.1.2). Following the similar procedure as [77, 75], the 2D histogram is projected along the X direction to make a Gaussian fit, and the FWHM was obtained from the fit to get the ISR using the PSF_{image} as given by Eq.(6.1.4).

6.3 Spatial Resolution

To evaluate the spatial resolution that can be obtained with the proposed detector module readout configuration using 6×6 mm active area Hamamatsu $S14160-6050HS$ model SiPM, a large number of muon interaction events (5000 events) have been simulated at the centre and the edge of the grid. The difference in the number of photons reaching each SiPM with different panel thicknesses is shown in Figure 6.3.1. The LSF represents the spatial distribution of the number of photons detected at the readout face by the SiPMs. Typical LSF values corresponding to muon interaction events at 5 cm SiPM spacing with interaction muon interaction at the centre and the edge of the grid with panel thickness 2.5 cm is shown in Figure 6.3.2. Similarly, typical LSF values for 1.27 cm panel thickness is shown in Figure 6.3.3.

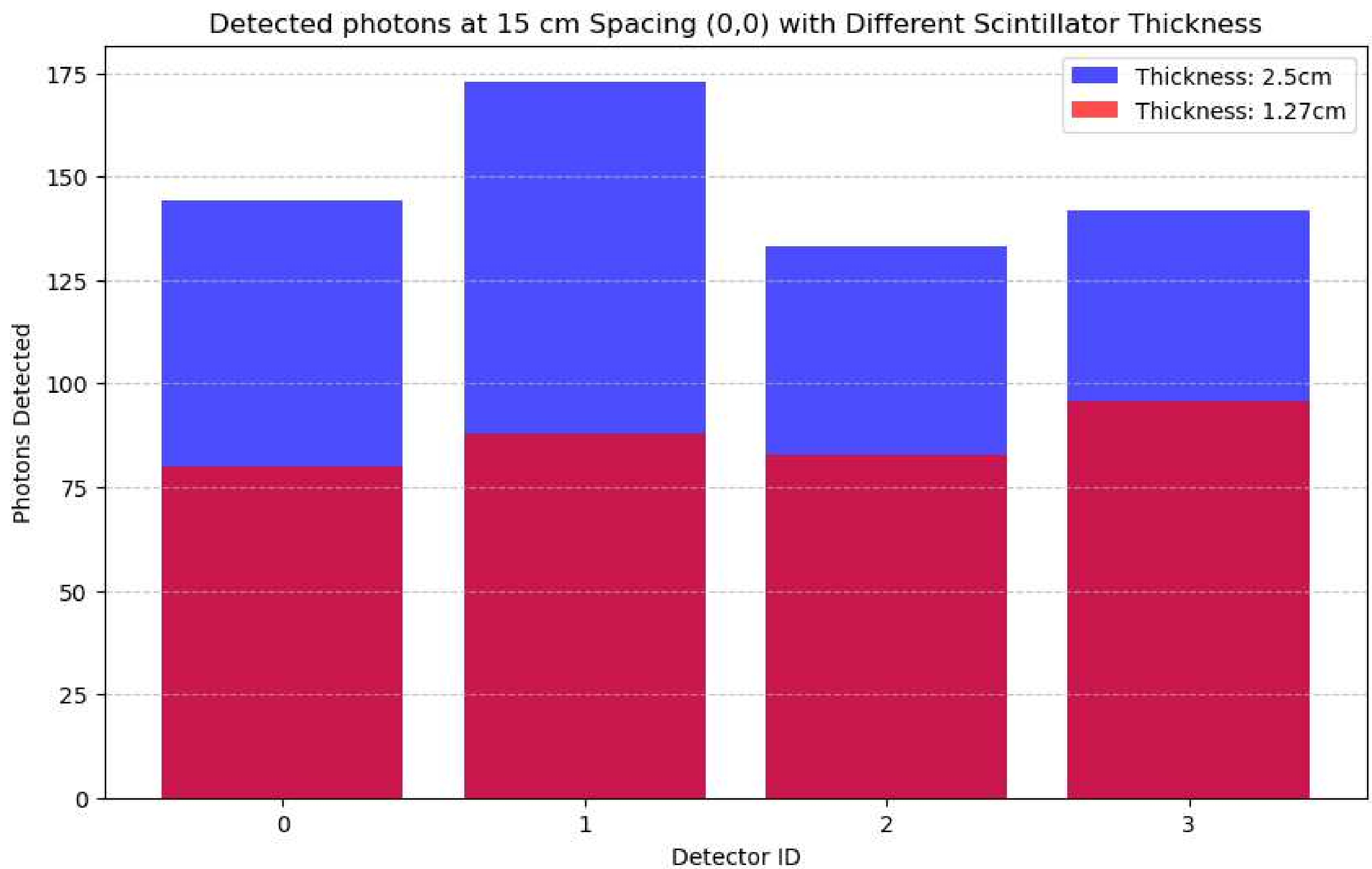

Figure 6.3.1: Detected photons at each SiPMs with two different panel thicknesses.

Distributions of the interaction point PSFs are obtained as a 2D histogram of the calculated interaction point coordinates, for all the muon interaction events simulated at two different points. A typical resulting planar image of the calculated interaction point position distributions of muon interactions at the centre of the grid is shown in Figure 6.3.4a, where well-resolved PSFs can be identified. The corresponding projection of the PSF profile on the X-axis of the and their Gaussian fits is shown in Figure 6.3.4b.

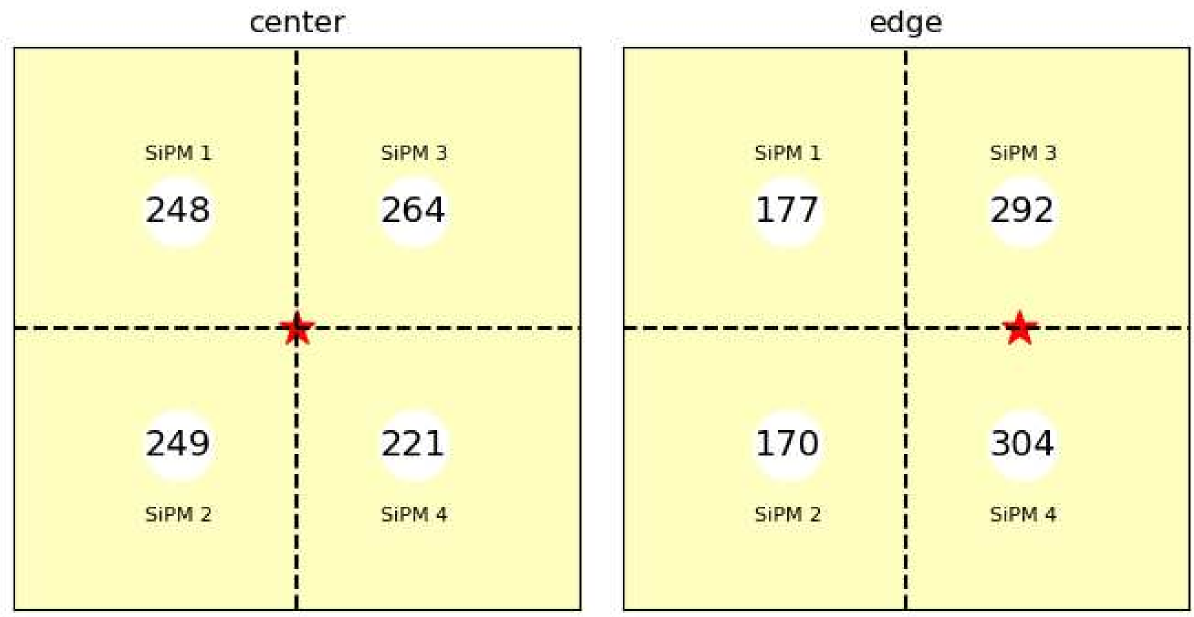

Figure 6.3.2: Typical LSF values at 5 cm SiPM spacing and 2.5 cm panel thickness.

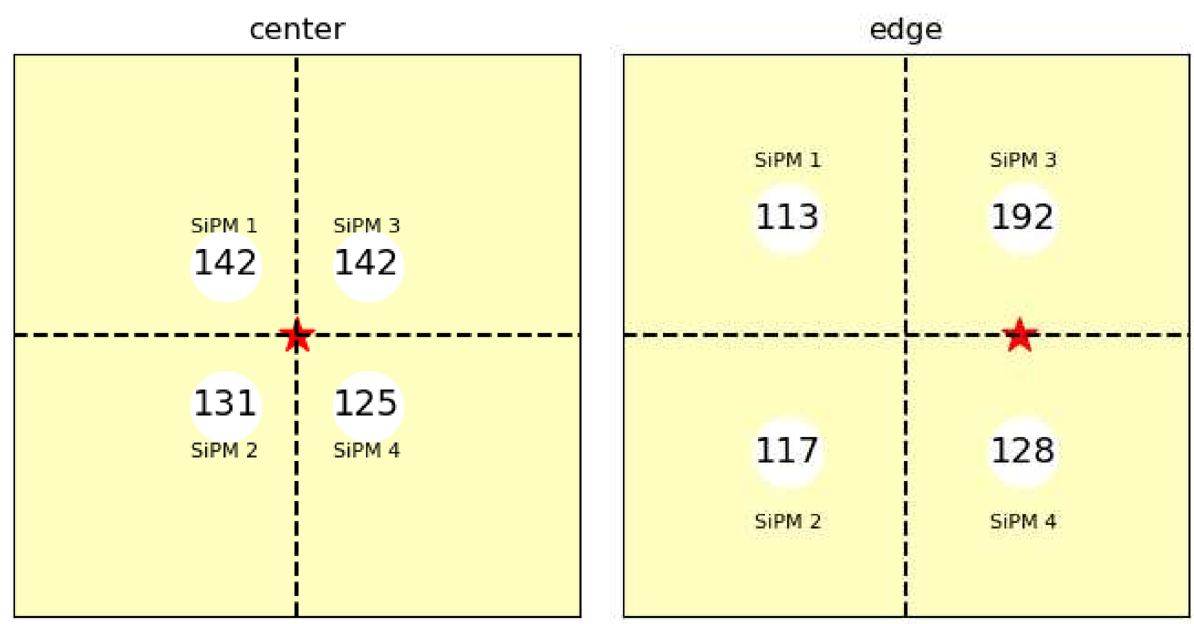

Figure 6.3.3: Typical LSF at 5 cm spacing and 1.27 cm panel thickness.

Distributions of the interaction point PSFs are obtained as a 2D histogram of the calculated interaction point coordinates, for all the muon interaction events simulated at two different points.

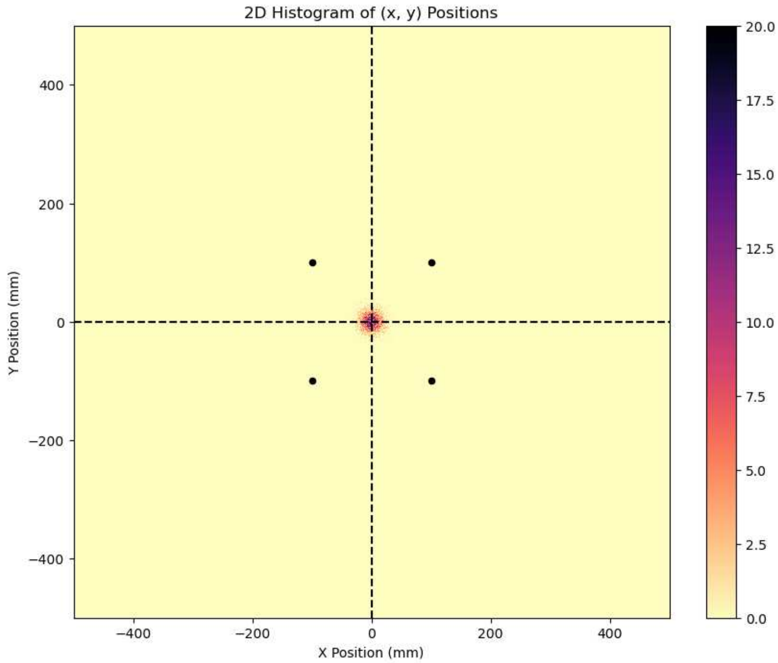

(a) PSF$_{image}$ at the centre

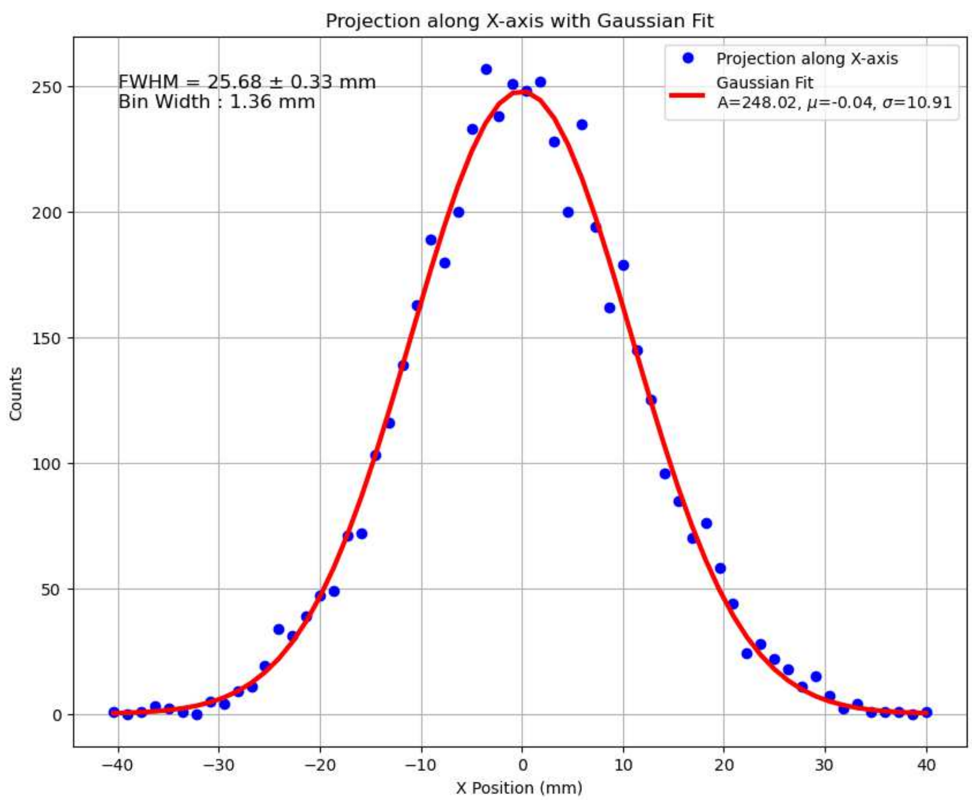

(b) Projection along X-axis with Gaussian fit. Here A = amplitude, μ = mean, and σ = Standard Deviation. [$\chi^2 = 64.80$, Critical value (df= 57, $\alpha = 0.05$) = 75.62]

Figure 6.3.4: PSF$_{image}$ obtained and its Gaussian fit projected along the X direction at 20 cm spacing of SiPMs at 1.27 cm panel thickness with the interaction event happening at the centre of the square grid.

The result for all the SiPM spacings with the interaction happening exactly at the centre of the square grid is shown for 5000 scintillation events is shown in Figure 6.3.5.

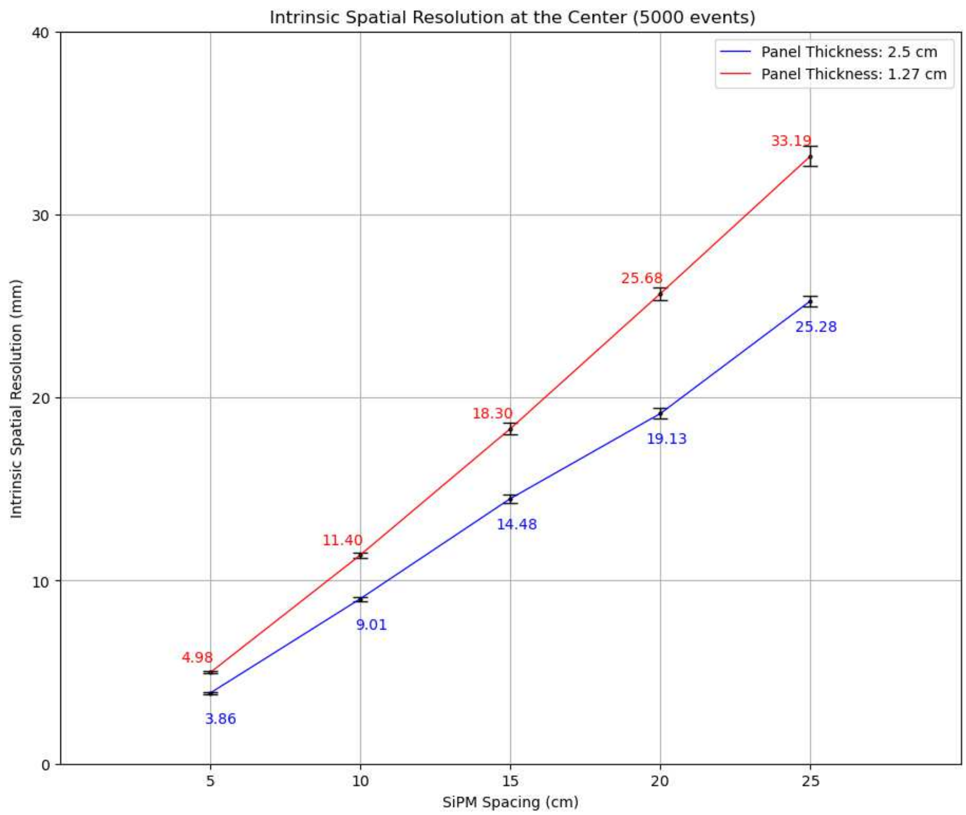

Figure 6.3.5: ISR for scintillation event happening at the centre of the square grid for different SiPM spacings and panel thicknesses.

To test the goodness of the fits, a χ^2 test for 95 % C.L was performed for all the fits. For 1.27 cm panel thickness, a successful test was obtained for all the SiPM spacings. For the 2.5 cm panel thickness, a successful χ^2 test was obtained only at 5 cm spacing. As the panel thicknesses increases, a tail starts to appear in the fit as seen in Figure 6.3.6, and keeps increasing as the spacing increases. This is because of the higher fluctuations in the number of scintillation photons being created and reaching individual SiPMs for 2.5 cm panel thickness.

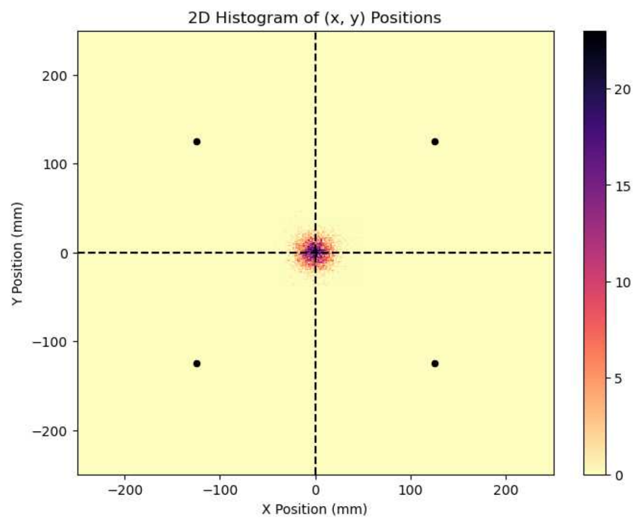

(a) PSF$_{image}$ at the centre

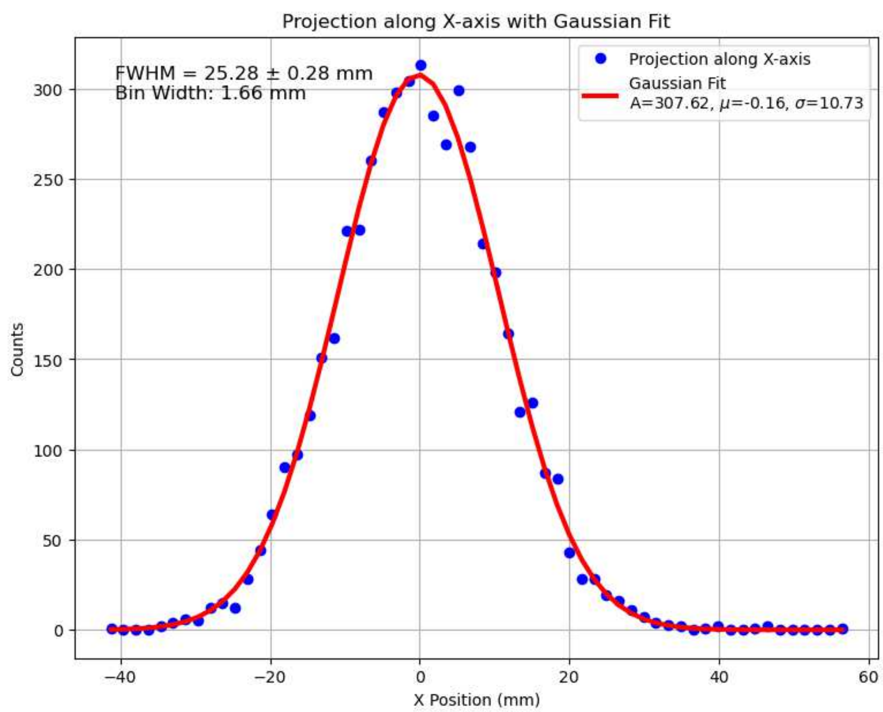

(b) Projection along X-axis with Gaussian fit

Figure 6.3.6: PSF$_{image}$ obtained and its Gaussian fit projected along the X direction at 25 cm spacing of SiPMs at 2.5 cm panel thickness with the interaction event happening at the centre of the square grid.

To test how the spatial resolution looks like as you move towards the edge of the grid, interaction events were performed moving half-way in X and centered in Y of the square grid. A typical example of this event interaction is shown in Figure 6.3.7.

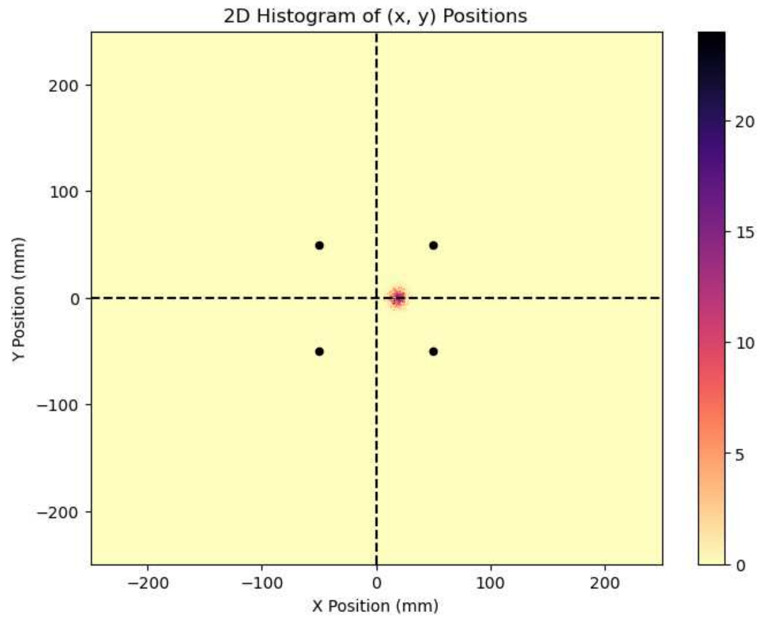

(a) PSF$_{image}$ for interaction event at (4 cm, 0)

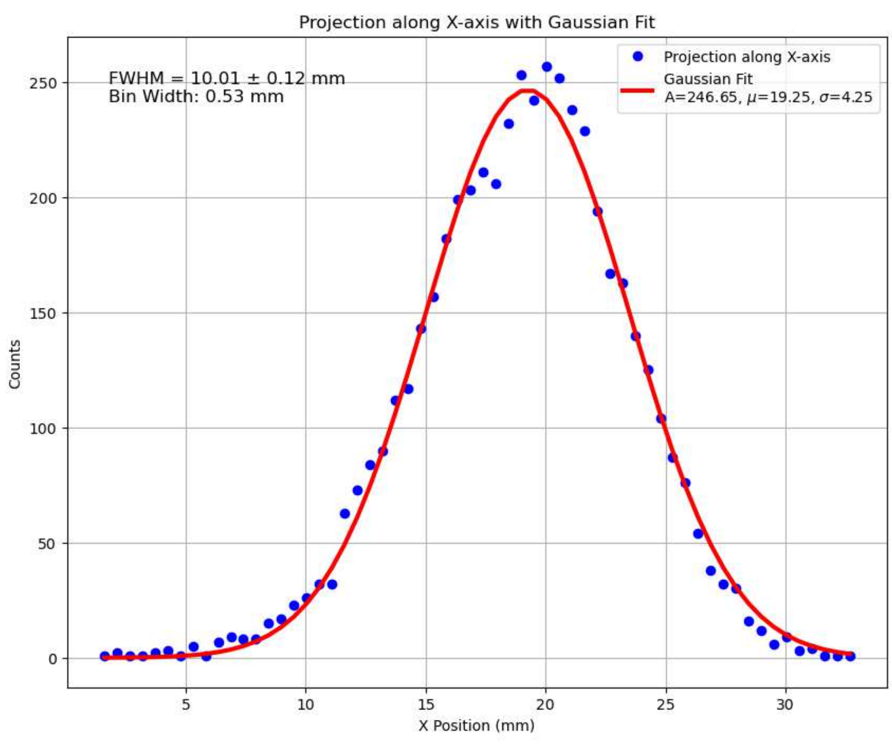

(b) Projection along X-axis with Gaussian fit

Figure 6.3.7: PSF$_{image}$ obtained and its Gaussian fit projected along the X direction at 10 cm spacing of SiPMs at 1.27 cm panel thickness with the interaction event happening at the edge of the square grid.

A degradation of the spatial resolution can be seen outside the central region. The centering of the PSF is off from where the actual event was happening, and a tail can be observed in the corresponding fit. The PSF corresponding to muon interactions as seen in Figure 6.3.7 are showing a non-linear response (compression effect) [77] of the centroid estimation algorithm. Table 6.3.1 shows the muon interaction point and the centering of the PSF profiles for different thicknesses and spacings.

Table 6.3.1: Table showing PSF centering for the respective muon interaction point at different spacings and thicknesses.

(a) 2.5 cm thickness

SiPM Spacing (cm)	Muon Interaction Point (cm)	PSF Centering (cm)
5	$(2, 0)$	1.020
10	$(4, 0)$	1.702
15	$(6, 0)$	2.267
20	$(9, 0)$	3.084
25	$(11, 0)$	3.780

(b) 1.27 cm thickness

SiPM Spacing (cm)	Muon Interaction Point (cm)	PSF Centering (cm)
5	$(2, 0)$	1.069
10	$(4, 0)$	1.925
15	$(6, 0)$	2.608
20	$(9, 0)$	3.568
25	$(11, 0)$	4.440

6.4 Summary

These results are an initial estimation of the expected detector spatial resolution considering a simple square arrangement of SiPMS at different spacings. To study the influence of the scintillator slab thickness on light production and collection, two different panel thickness was tested at different spacings. As seen in Figure 6.3.5, the ISR for two different panel thicknesses shows that ISR ~ 1 cm can be obtained at spacings $5 - 10$ cm. For the 2.5 cm panel thickness, a successful χ^2 test for 95 % C.L was obtained only at 5 cm spacing. As the spacing is increased, a skewed fit starts to appear. This is because of higher fluctuations in the number of scintillation photons being created and reaching individual SiPMs for the 2.5 cm panel as seen in Figure 6.3.1. The degradation of the spatial resolution can be seen outside the central region of the square grid as seen in Figure 6.3.7. The PSF corresponding to muon interactions at the edge as seen in Table 6.3.1 is showing a non-linear response (compression effect) [77] of the centroid estimation algorithm.

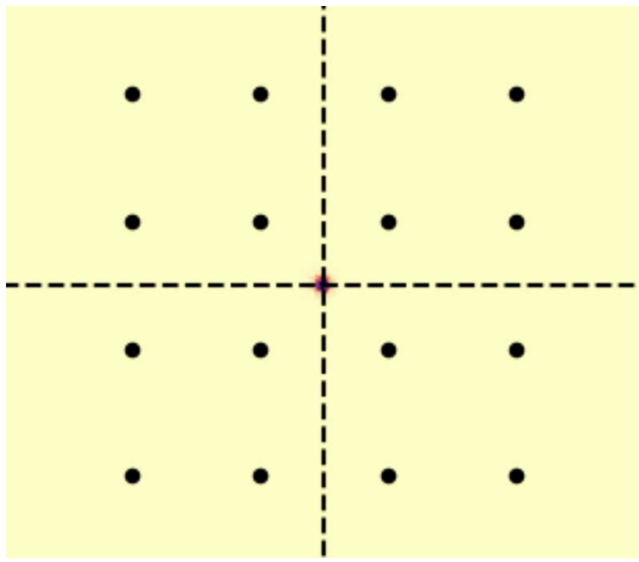

Figure 6.4.1: Schematic diagram of grid configuration with more SiPMs.

For realistic detector modules, a larger number of SiPMs in the readout configuration, as depicted in Figure 6.4.1, is essential for accurate point of interaction calculation, a topic to be explored in future work.

Chapter 7

The Scalar Dark Higgs Boson

The SM-like Higgs boson was discovered at the LHC. The ATLAS and CMS collaborations have subsequently demonstrated that the Higgs mechanism is responsible for generating the masses of elementary particles [78, 79]. As discussed in §2.2.1, the origin of the mass of DM in the universe remains a mystery because it does not consist of any SM particle. There are various models that predict observable signatures for which a number of experimental efforts are being carried out [8].

The discovery of a resonance at mass $\sim$ 125 GeV, with properties consistent with the (SM)-like Higgs boson confirms the basis for the electroweak symmetry breaking [3, 4]. For extensions of the SM, additional scalars are often required to exist. The perturbative Coleman-Weinberg [80] models with classical scale invariance broken radiatively and spontaneously can be constructed by coupling to a complex scalar field. These models feature at least one additional (real) singlet scalar, S [81]. One particularly interesting possibility for DM particles to obtain their mass is through electroweak symmetry breaking. If the scale invariance is broken at the electroweak scale by the vacuum expectation value (vev) $\langle S \rangle$, then a GeV-scale scalar state, ϕ, is produced from it [82]. This state is known as the pseudo-Goldstone boson associated with the spontaneous breaking of the scale invariance [83].

This mechanism is referred to as the dark Higgs mechanism, and the resulting scalar boson is called the dark Higgs boson (DHB) [84]. This concept implies that DM particles are not solitary; instead, they coexist with extra scalar and vector bosons, constituting a complete dark sector [84]. The existence of a DHB and a novel gauge symmetry, extending the SM, opens up exciting opportunities for investigating DM phenomenology. The scalar fields generally mix with each other through the scalar potential. This provides some SM-like characteristics to the DHB, influencing the experimental outcomes of the latter. Consequently, the identification of the SM-like Higgs boson at the LHC serves as a pathway to uncovering DHBs.

7.1 The Dark Higgs Properties

A renormalizable portal between the dark Sector and SM creates a scenario with a new scalar field "S" with a quartic couplings to SM Higgs field "H". A simple Lagrangian with the potential terms to describe this scenario looks like [85, 86]

$$\mathcal{L} = \mathcal{L}_{kin} + \mu_S^2|S|^2 - \lambda_S|S|^4 + \mu^2|H|^2 - \lambda|H|^4 - \lambda_{h\phi}|S|^2|H|^2, \tag{7.1.1}$$

where the terms with odd number of dark scalars "S" are suppressed. The parameters μ and λ are real constants, and μ_S and λ_S are free parameters. The quartic term $\lambda_{h\phi}|S|^2|H|^2$ induces the mixing between the dark scalar S and SM Higgs H.

The dark Higgs field is a complex scalar field which is a singlet under the SM gauge group but carries charge under a new $U(1)'$gauge group. The scalar field acquires a *vev*, breaking the $U(1)'$ gauge symmetry spontaneously, giving mass to the corresponding gauge boson. The other dark sector particles may also get masses in this process. The *vev* of dark Higgs field is denoted by "v_2" and the resulting physical DHB by "ϕ". Similarly the *vev* of SM Higgs field is denoted by "v_1" and the physical SM Higgs boson by "h". As seen in Eq.(7.1.1), before the symmetry breaking the scalar potential contains the term [87]

$$V(S,H) = \lambda_{h\phi}|S|^2|H|^2, \tag{7.1.2}$$

where the coupling term is denoted by $\lambda_{h\phi}$, S denotes the complex dark Higgs field, and H denotes the SM Higgs field. After the symmetry breaking and using *vev* (see Appendix §A.2 and §A.3), we have

$$S = \frac{\phi + v_2}{\sqrt{2}} \tag{7.1.3}$$

$$H = \frac{h + v_1}{\sqrt{2}} \tag{7.1.4}$$

After diagonalizing, the physical fields obtained are the 125 GeV SM Higgs boson, h, and the DHB ϕ. The physical fields in terms of the gauge eigenstates are now given by [87]

$$\phi \to \phi \cos\theta - h \sin\theta \tag{7.1.5}$$

$$h \to h \cos\theta + \phi \sin\theta, \tag{7.1.6}$$

where θ is the mixing angle between h and ϕ given by (assuming $\theta << 1$) [87]

$$\theta \approx \frac{\lambda_{h\phi} v_1 v_2}{m_h^2 - m_\phi^2}. \tag{7.1.7}$$

The mixing angle $\theta << 1$ and $\lambda_{h\phi} << 1$ to satisfy the current experimental constraints are required by the observed properties of the SM Higgs boson [85]. The SM Higgs-Dark Higgs mixing generates the Yukawa-like couplings between dark Higgs and SM fermions as

$$\sin\theta \frac{m_f}{v_1} \phi f \bar{f}. \tag{7.1.8}$$

For the mass of the scalar ϕ considerably below the electroweak scale, the effective Lagrangian can now be written as [85]

$$\mathcal{L} = -m_\phi^2\phi^2 - sin\theta\frac{m_f}{v_1}\phi f\bar{f} - \lambda v_1 h\phi\phi + ..., \tag{7.1.9}$$

where *vev* of the SM Higgs $v_1 \simeq 246$ GeV, $\lambda = \lambda_{h\phi}$, and m_f is the mass of the SM fermions. The higher order terms have been omitted here. The last term is the non-negligible trilinear interaction term between h and ϕ with the coupling λ.

7.2 Phenomenology of the Dark Higgs Boson

7.2.1 Decay Mode of Dark Higgs

The DHB obtains couplings to the SM particles proportional to $\sin\theta$. So it will have the same decay modes as the SM Higgs boson with mass m_ϕ and each partial decay width suppressed by a factor of $\sin^2\theta$. For $m_\phi < \frac{m_h}{2}$, the SM Higgs boson can also decay into a pair of DHBs. The reverse decay is also possible for $m_h < \frac{m_\phi}{2}$. We will look at the simplest case where there are no other hidden sector decay modes.

The public tool $HDECAY$ provides partial decay widths for SM-like Higgs bosons in the mass range $2m_D \lesssim m_\phi \lesssim 1$ TeV [88]. The decay width becomes unphysical due to diverging next-to-leading order electroweak corrections for larger masses [89]. It is also essential to take into account the confinement of the final-state particles for masses beyond the D meson threshold. There are complications in the decay width for the mass range $2m_\pi < m_\phi \lesssim 2.5$ GeV because of the decays into mesons and resonances [81]. There are no satisfactory agreement in the literature regarding their values. So we will use the most widely used approach from [90], which switches from dispersive analysis to spectator model at 2 GeV, and interpolate between these two for the intermediate mass range 1 GeV $\lesssim m_\phi \lesssim$ 2.5 GeV. The hadronic decay rates however requires careful treatment because of the strong final state interactions. The currently widely accepted branching ratios for the lighter dark Higgs boson are shown in Figure 7.2.1. Above the muon threshold ($2m_\mu < m_\phi$), the decay mode is dominated in the narrow region $2m_\mu < m_\phi < 2m_\pi$ by the $\mu^+\mu^-$ decays. The dominant decay modes are hadrons for larger masses. The relevant decay modes are presented in Appendix §B.1.1 based on the branching ratios.

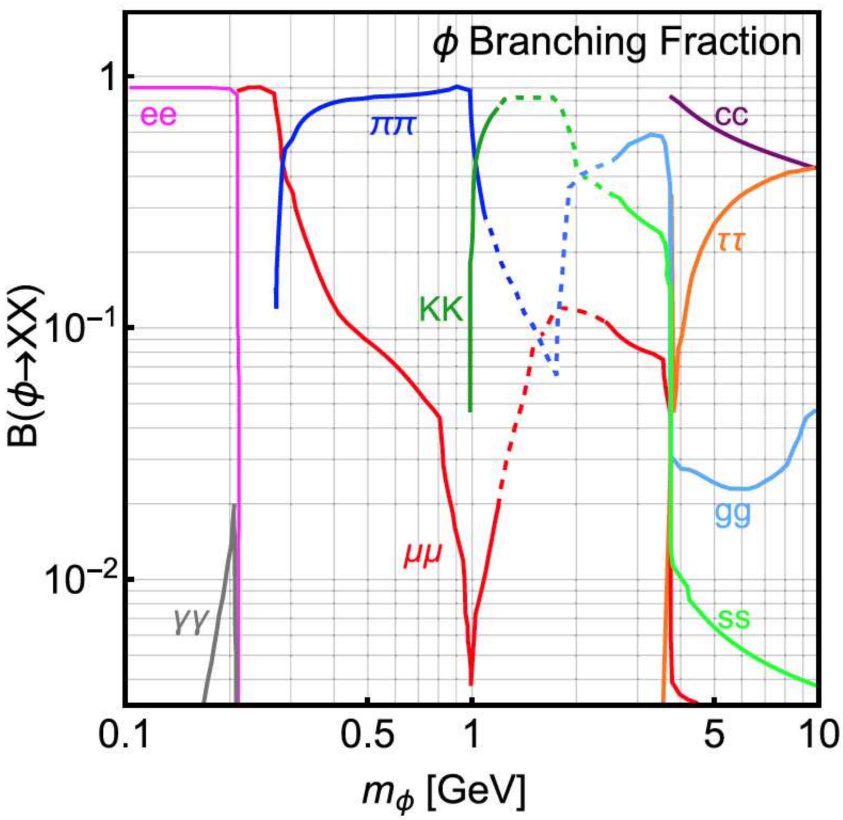

Figure 7.2.1: Branching ratios of the light dark Higgs as a function of m_ϕ as adapted from [91, 92].

7.2.2 Dark Higgs Production

In our analysis, we will consider two cases for the production of the DHBs. The first case will be the DHB with the vanishing trilinear coupling λ values as given by the second term in Eq.(7.1.9) for the inclusive B meson decays. The parameter space for this model is spanned by the DHB mass m_ϕ and the mixing angle $\sin^2\theta$. The second case will be the DHB with large trilinear coupling λ values as given by the last term in Eq.(7.1.9). In this case, the DHBs can be produced in pairs from the SM Higgs bosons with the parameter space for this model is spanned by the dark Higgs mass m_ϕ, the mixing term $\sin^2\theta$, and the trilinear coupling λ value.

7.2.2.1 Inclusive B Meson Decays $B \to X_s\phi$

The rare decays of B mesons and kaons offers the unique opportunity to search for a lower mass dark Higgs. It can also be produced in the D meson decays, however the corresponding effective coupling is suppressed by the small CKM elements and the ratio m_b^2/m_t^2 [87]. The branching ratio (Br) for the mesonic decays to dark Higgs have the hierarchy [91]

$$Br(B \to \phi) >> Br(K \to \phi) >> Br(\eta, \pi \to \phi). \tag{7.2.1}$$

The numbers of kaons (K) and light mesons (η, π) produced are roughly comparable [91]. The branching ratio hierarchy in Eq.(7.2.1) shows that the kaon decays are much more effective than the lighter mesons. The number of B mesons produced at the LHC is suppressed compared to kaons as shown by [91]. However the larger branching ratio of B mesons compensates for this as shown in Eq.(7.2.1). Another important aspect that needs consideration is that the B decays probes much higher dark Higgs mass compared to kaons because of higher mass of bottom quark in B mesons [91]. Taking his into consideration, we will show the results for DHB production from the rare decays of B mesons. The dominant contribution to B production comes from the parton-level process $gg \to b\bar{b}$.

Single DHB have the potential to emerge in meson decays by means of ϕ–h mixing, with rates directly linked to $\sin^2\theta$. Given that the dark Higgs inherits the couplings of the SM Higgs, the most substantial branching ratios occur in processes featuring heavy flavors, notably the B mesons. In particular, the inclusive decay of B mesons into dark Higgs bosons is chiefly governed by the parton-level phenomenon $b \to s\phi$, which encompasses a t–W loop, with the ϕ emitted from the top quark. Figure 7.2.2 shows the Feynman

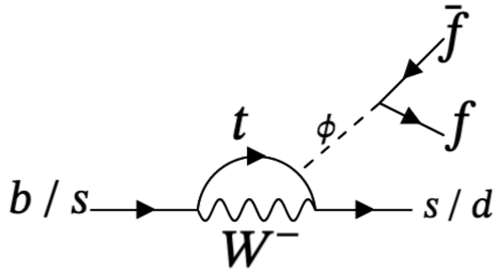

Figure 7.2.2: Feynman diagram for the dark Higgs boson (ϕ) production channels from rare B and K meson decays.

diagram for the DHB (ϕ) production channels discussed. A Higgs mixing portal introduces the possibility of inclusive $B \to X_s\phi$ decays. This mixing is characterized by a small angle $\theta \ll 1$. Top-loop contributions play a dominant role in determining the partial decay width, and the uncertainties from strong interaction effects are minimized yielding a branching ratio [93, 94, 95]

$$\frac{Br(B \to X_s\phi)}{Br(B \to X_c e\nu)} = \frac{27\sqrt{2}G_F m_t^4}{64\pi^2 \Phi m_b^2}\left|\frac{V_{ts}^* V_{tb}}{V_{cs}}\right|^2 \left(1 - \frac{m_\phi^2}{m_b^2}\right)\sin^2\theta, \tag{7.2.2}$$

where $Br(B \to X_c e\nu) = 0.104$ is the measured inclusive semi-leptonic rate [93], $X_{s,c}$ denotes any strange and charm hadronic state, where $\Phi \approx 0.5$ is the phase space factor for the semi-leptonic decay [96], $m_{b,t}$ is the bottom and top quark masses, V_{ij} denotes the CKM matrix elements. This yields the inclusive branching ratio [97]

$$Br(B \to X_s\phi) = 6.2\left(1 - \frac{m_\phi^2}{m_b^2}\right)\sin^2\theta. \tag{7.2.3}$$

The mass of the bottom quark is taken to be $m_b = 4.18$ GeV [5]. This ratio will break down as the mass of the dark Higgs m_ϕ approaches m_b. We will use the Eq.(7.2.3) to obtain the ϕ production rate in the inclusive B meson decays in the following section.

7.2.2.2 Exotic Higgs Decay $h \to \phi\phi$

The Lagrangian in Eq.(7.1.9) also describes $h \to \phi\phi$ decay [86]. The parameter space is spanned by the dark Higgs mass m_ϕ, the mixing angle $\sin^2\theta$, and an additional trilinear coupling λ parameter. The branching ratio for the exotic Higgs decay is given by [91]

$$Br(h \to \phi\phi) = \frac{\Gamma(h \to \phi\phi)}{\Gamma_h} \approx \frac{1}{\Gamma_h^{SM}} \frac{\lambda^2 \nu^2}{8\pi m_h} \left(1 - \frac{4m_\phi^2}{m_h^2}\right)^{\frac{1}{2}} \simeq 4700\lambda^2. \tag{7.2.4}$$

The longer lived DHBs are indicative of invisible Higgs decays which are constrained by the searches at CMS [98] and ATLAS [99, 100]. The most stringent current bound of $Br(h \to invisible) < 0.24$ implies the value for $\lambda < 7.1 \times 10^{-3}$ [91]. These decays can be detected by ADAM extending the reach of the ATLAS detector for the invisible Higgs decays.

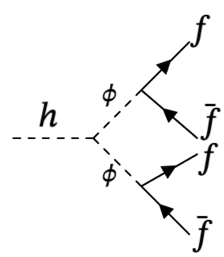

Figure 7.2.3: Feynman Diagram for the SM Higgs decaying to a pair of dark Higgs.

7.3 Cosmological Motivation

The DHB can play significant role in the early universe, astrophysical systems, and in the interactions of dark matter particles. The role of the DHB has been studied extensively in cosmological contexts given by references [92, 87, 101, 102] .

7.3.1 Early Universe

This discovery of neutrino oscillation posed a challenge to the original formulation of the SM, which did not include mechanisms for neutrino mass or oscillation. As a result, extensions to the SM were proposed to accommodate neutrino masses and oscillations. This suggests the existence of physics beyond the Standard Model. Additionally, cosmology puts forth two other phenomena - dark matter and the baryon asymmetry of the Universe - that remain unaccounted for within the Standard Model. The solution to these three challenges is proposed through the concept of a Neutrino Minimal Standard Model (νMSM) [101], conceived as a minimalistic extension of the Standard Model with neutrinos, aiming to comprehensively address all three issues [87].

The νMSM, originally a minimal extension of the standard model involving three right-handed neutrinos, also incorporate inflation. This extension offers a unified origin for electroweak symmetry breaking and the masses of right-handed neutrinos which also accounts for inflation simple extension of the νMSM by a real scalar field (inflaton) [101]. Furthermore, it aligns with experimental evidence on neutrino oscillations and complies with all relevant astrophysical and cosmological constraints regarding sterile neutrinos as potential dark matter candidates.

The processes that contribute to the thermalization (with the plasma of SM particles) of DHBs have been studied in detail in [103]. If DHBs enter into thermal equilibrium with the SM thermal bath, it is essential that they decay or annihilate away before the beginning of Big Bang Nucleosynthesis (BBN). If the mixing angle is so small that the DHBs do not enter into thermal equilibrium, it may still be possible to produce them non-thermally via the freeze-in mechanism [104]. In this case, the constraints from BBN are relaxed considerably, and it is possible for DHBs to be stable on cosmological scales, and constitute the dominant form of dark matter. Even if the DHB itself does not constitute a dark matter candidate, it may help to explain the observed dark matter relic abundance via the freeze-out mechanism either as a mediator for dark matter annihilations ($DM + DM \to \phi \to SM + SM$) or as final state in the annihilation process ($DM + DM \to \phi\phi$) [101].

7.3.2 Astrophysical systems

The lighter DHBs have the potential to be generated in astrophysical systems, presenting a unique cooling mechanism [105]. SN1987a, often interpreted as a core-collapse supernova explosion, is of particular interest in this context. Within the hot and dense core of a supernova, DHBs can be produced through nucleon-nucleon bremsstrahlung ($NN \to NN+\phi$) [105]. The emission of these low-mass elementary particles causes a direct energy-loss channel from the interior of stars. With the help of the observed properties of the stellar systems, limits can be derived on the energy-loss mechanism. It can also be used to constrain the interactions of these new particles.

Chapter 8

Detecting Dark Higgs Boson with ADAM

To illustrate the physics reach of the ADAM detector, we will consider the benchmark hidden sector model as discussed in Chapter 7. The dark Higgs boson mixes with the SM Higgs boson through the Higgs portal as described in Eq.(7.1.9) [106]. We need to obtain the ϕ production rate in the inclusive B meson decays in our study which is given by the Eq.(7.2.3). Then also the ϕ production rate in the exotic Higgs decays given by the equation Eq.(7.2.4). As discussed in in §3.4, the HL - LHC is expected to operate at the centre of mass energy $\sqrt{s} = 14$ TeV and deliver 715 fb^{-1} of data during Run 4. The following simulation model will be based on these projected parameters for the Run 4 target.

8.1 Leptonic Decays of the Dark Higgs Boson

As discussed in section §7.2, the most widely used approach for the decay rate into the leptonic final states is given by [90]

$$\Gamma_{\phi\to l\bar{l}}(GeV) = \frac{\sin^2\theta G_F m_\phi m_l^2}{4\sqrt{2}\pi}\beta_l^3, \tag{8.1.1}$$

where $l = e, \mu, \tau$, $G_F = 1.167 \times 10^{-5}$ GeV^{-2} is the Fermi constant, and $\beta_l = \sqrt{1 - \frac{4m_l^2}{m_\phi^2}}$ is the velocity of the leptons in the final state. The formula breaks down when m_ϕ approaches $2m_l$ because of the ratio in the β_l term.

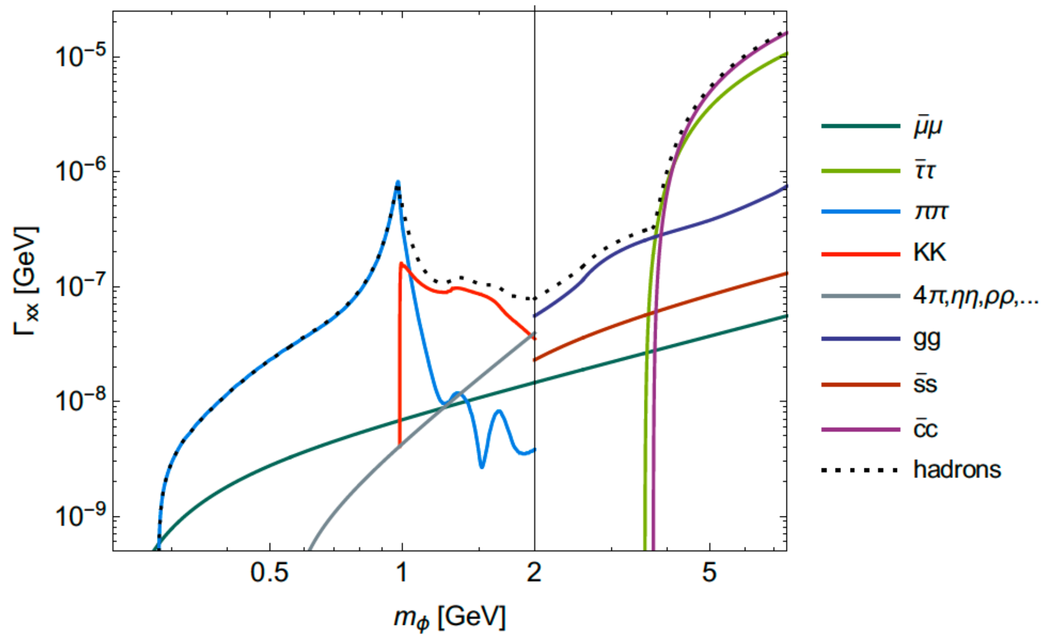

Figure 8.1.1: The hadronic and leptonic decay rates of a light scalar mixing with the Higgs scaled with $\sin^2\theta$ (set to unity) as adapted from [90].

The decay rate and the corresponding lifetime of the dark Higgs boson is shown in Figure 8.1.2, where $\sin^2\theta$ was set to unity. The DHB lifetime (τ_ϕ) can be calculated from the decay rate using the formula

$$\tau_\phi(s) = \frac{\hbar}{\Gamma}, \tag{8.1.2}$$

where $\hbar = 6.5821 \times 10^{-25}$ GeV.s, and decay rate Γ is as obtained from Eq.(8.1.1). The lifetime for the corresponding $\sin^2\theta$ value can be obtained using the Eq.(8.1.1). The formula breaks down below the muon threshold ($m_\phi < 2m_\mu$).

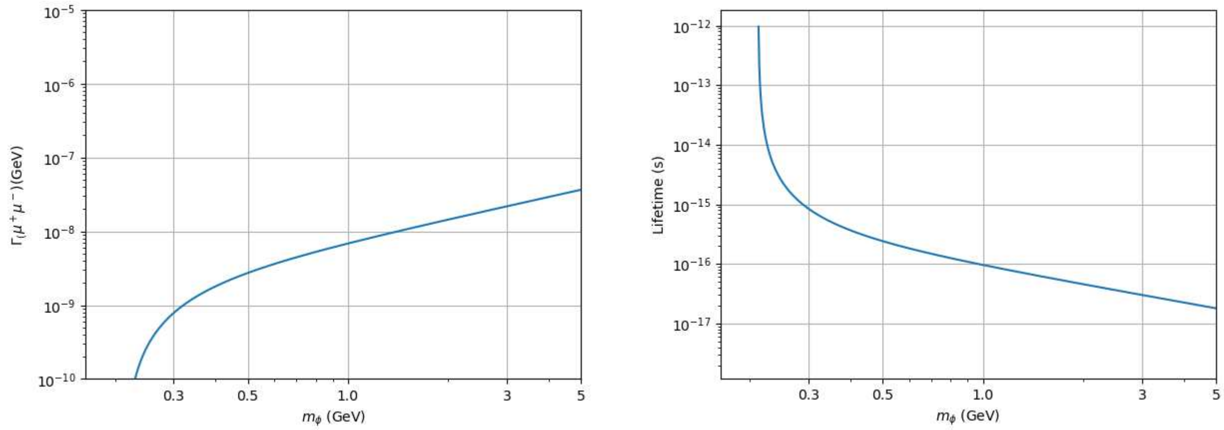

(a) Leptonic decay rate of the decay $\phi \to \mu^+\mu^-$

(b) Lifetime of ϕ in the decay $\phi \to \mu^+\mu^-$

Figure 8.1.2: The decay rate was obtained in (a) using the Eq.(8.1.1). The lifetime of ϕ was obtained in (b) using the decay rate. The scaling factor $\sin^2\theta$ has been set to unity in this plot.

The decay length is given by the formula (see Appendix §B.2)

$$l = c\tau_\phi\gamma\beta = c\tau_\phi\frac{p_\phi}{m_\phi}, \tag{8.1.3}$$

where c is the speed of light, τ_ϕ is the dark Higgs lifetime, and p_ϕ is the momentum. A DHB with m_ϕ may be produced in B meson decays with $p_\phi \approx m_B/2$ [87]. As seen in the Table B.1.1, the $\phi \to e^+e^-$ decay is relevant from 1.02 to 212 MeV. As discussed before and seen in Figure 7.2.1, the decay mode is dominated by the electrons below the muon threshold. The tiny electron Yukawa coupling leads to an extremely long lifetime. This results in a negligible event rate in ADAM, as most DHBs will typically overshoot the detector as seen in Figure 8.1.3. The decay distance was calculated using Eq.(8.1.3) considering B meson decays. In the exotic Higgs decays, the boost will be much higher because of the higher mass of SM Higgs than the B meson. The decays to taus also becomes relevant beyond the $m_\phi > 3.6$ GeV. The branching fraction $Br_{B\to X_s\phi}$ given by the Eq.(7.2.3) breaks down as m_ϕ approaches $m_b = 4.18$ GeV. So the decays to tau final states becomes unimportant because of the limit set by the bottom quark. The decays to taus can probe much higher masses for the DHB.

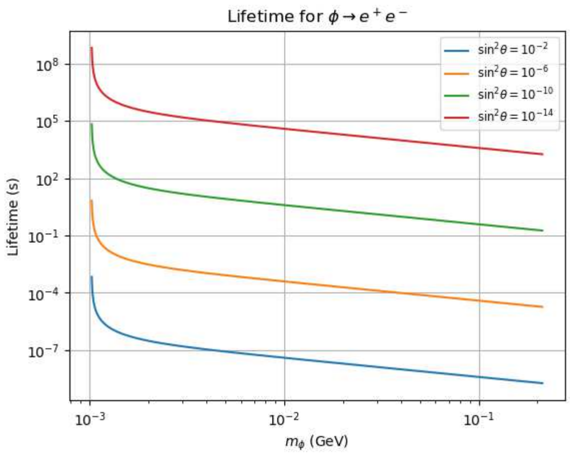

(a) Lifetime at various $\sin^2\theta$ values

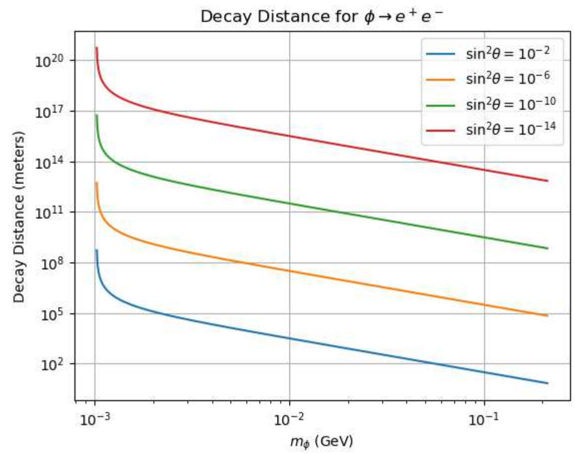

(b) Decay distance at various $\sin^2\theta$ values

Figure 8.1.3: Lifetime (s) and decay distance (m) of the dark Higgs boson for $\phi \to e^+e^-$ decay in the mass range $m_\phi \sim 1.02 - 212$ MeV.

This is essential specially in the case of the exotic Higgs decays which can probe much higher masses. The lifetime of the DHB and the associated decay distances considering exotic Higgs decays is shown in Figure 8.2.1. The decay distance is calculated using the formula from Eq.(8.1.3), where m_ϕ is being produced with $p_\phi \approx m_h/2$. In the lower mass range (< 5 GeV) ADAM is sensitive in a very narrow region. For higher $\sin^2\theta$ values, the DHB will typically undershoot the detector, and is sensitive in the very narrow mass range around 4 GeV in the lower $\sin^2\theta$ values. In the higher mass range (> 5 GeV), ADAM can be sensitive to $\phi \to \tau^+\tau^-$ in the exotic Higgs decays. However because of the uncertainties in the branching fraction for $\phi \to \tau^+\tau^-$ in the higher mass range [90, 92], we will only focus on the $\phi \to \mu^+\mu^-$ decays in the current scope of the thesis.

8.2 *Pythia8* Simulation for the Dark Higgs Boson

The Pythia event generator [10], a general-purpose Monte Carlo event generator, is widely utilized in particle physics and related fields, either independently or integrated into various other software programs. Its primary purpose is to simulate the physics phenomena happening during collisions of high-energy particles, like those occurring at the LHC collider at CERN. We will be using *Pythia*8 event generator [10], which can incorporate hadronization required for our study. In this introductory analysis, we are assuming a total detector/tracking efficiency of 100% and no background interference. This simplification allows for straightforward comparisons with other experiments in our research.

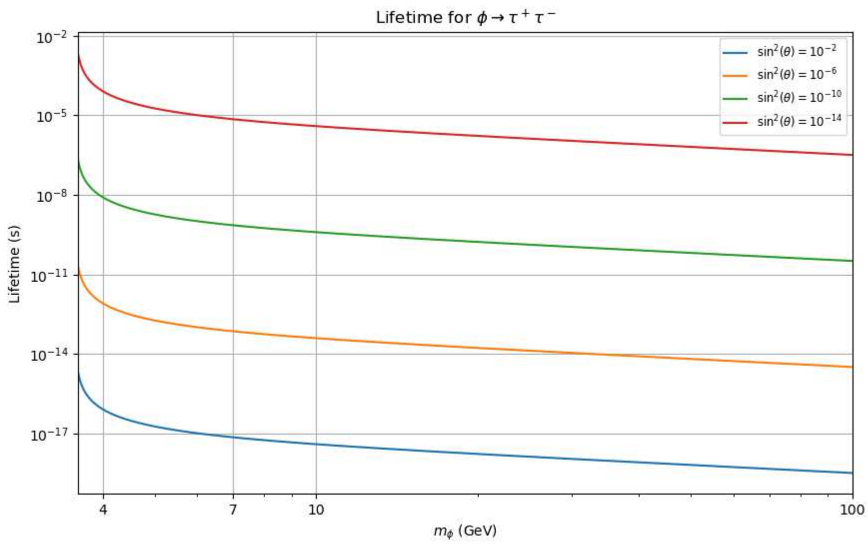

(a) Lifetime at various $\sin^2\theta$ values

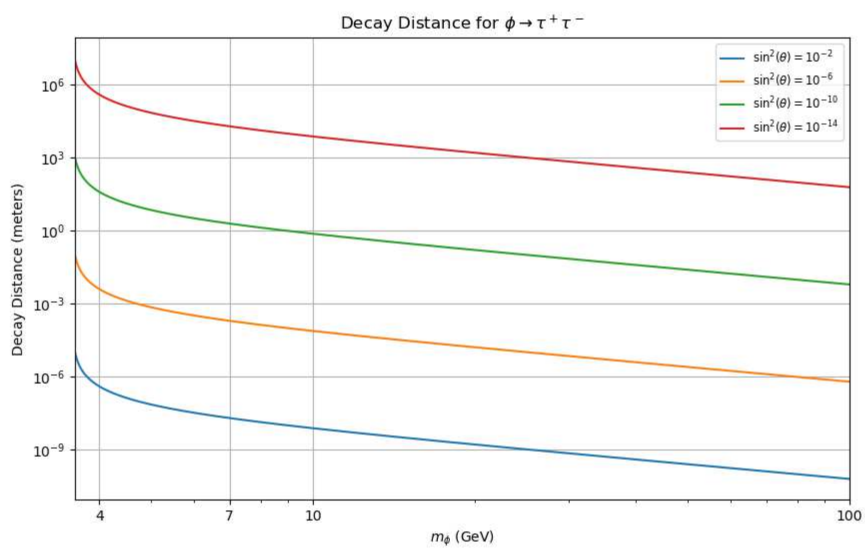

(b) Decay distance at various $\sin^2\theta$ values

Figure 8.2.1: Lifetime (s) and decay distance (m) of the dark Higgs boson for $\phi \to \tau^+\tau^-$ decay in the mass range $m_\phi \sim 3.6 - 100$ GeV.

A new particle with the properties of the dark Higgs as described in §7.2.1 is added to the standard *Pythia*8 particle data. The dark Higgs is set to decay as $\phi \to \mu^+\mu^-$ with branching fractions as shown in Figure 7.2.1. The total number of events to be generated for the simulation using Eq.(3.3.4) can be estimated as

$$N_{\phi,events} \simeq L^{int} \times \sigma \times Br_P, \tag{8.2.1}$$

where L^{int} is the integrated luminosity, σ is the cross-section of the specific process being considered ($b\bar{b}$ or gg in our study), Br_P is the branching ratio of the parent particle being considered (B meson or SM Higgs in our study). Hence, the number of the DHB decays in the ADAM detector can be estimated using

$$N_{\phi,ADAM} \simeq N_{\phi,events} \times Br(\phi \to \mu^+\mu^-) \times \epsilon_{fid}(c\tau) \times \epsilon_{det}, \tag{8.2.2}$$

where $N_{\phi,events}$ is as given by Eq.(8.2.1), $Br(\phi \to \mu^+\mu^-)$ is the branching ratio of the DHB decay to muon pairs, $\epsilon_{fid}(c\tau)$ is fiducial efficiency for the ADAM detector, and ϵ_{det} is the ADAM detector efficiency. Hereafter, we set the overall detector efficiency to $\epsilon_{det} = 1$ assuming 100% efficiency. Now the number of the DHB decays in the ADAM detector can be estimated using

$$N_{\phi,ADAM} \simeq N_{\phi,events} \times Br(\phi \to \mu^+\mu^-) \times \epsilon_{fid}(c\tau). \tag{8.2.3}$$

The detector's fiducial efficiency can be estimated in two ways: one is by using a suitable Monte Carlo event generator such as Pythia to simulate a significant number of events and tallying the fiducial decays directly, while the other involves gathering data on the kinematic distribution of the LLPs and carrying out a numerical integration across the detector decay volume.

8.2.1 *Pythia*8 Setup for the Inclusive B Meson decays

As discussed in §7.2.2.1, we will follow the similar approach as [93] using the process

$B \to K\phi$ as a proxy for $B \to X_s\phi$ for our study. Using the default *Monash* tune [107] in our Pythia8 model, we generate B meson samples produced in p–p collisions at $\sqrt{s} = 14$ TeV with the *HardQCD* : *hardbbbar* module turned on in Pythia. We will decay the B meson samples exclusively to the DHB as $B \to K\phi$. The total number of expected ϕ events can be estimated using Eq.(8.2.1) as

$$N_{\phi,events} \simeq L^{int} \times \sigma_{b\bar{b}} \times Br_{B\to X_s\phi}, \tag{8.2.4}$$

where $L^{int} = 715$ fb^{-1} for the HL - LHC during Run4 , $\sigma_{b\bar{b}}$ is the total $b\bar{b}$ cross-section, and $Br_{B\to X_s\phi}$ is the branching ratio of B meson decaying to $X_s\phi$ given by the Eq.(7.2.3). Pythia requires the mass of the DHB under a given set of model parameters. First we will calculate the lifetimes of the dark Higgs boson using the decay width formula given by the Eq.(8.1.1) for the leptonic decay which is constrained by the mass of DHB m_ϕ and the mixing term $\sin^2\theta$.

The next step is to determine the number of events for the ϕ production. We can get the number of events using the formula given by Eq.(8.2.4). The total $b\bar{b}$ cross-section will be assumed to be $\sigma_{b\bar{b}} = 500$ μb similar to that of [93] for 14 TeV HL - LHC. The branching fraction $Br_{B\to X_s\phi}$ can be obtained using the formula given by the Eq.(7.2.3), which is constrained by the mass of DHB m_ϕ and the mixing term $\sin^2\theta$. In this way, we can now perform the simulation to explore the parameter space $(m_\phi, \sin^2\theta)$ for the DHB. As seen in Eq.(7.2.3) and Eq.(8.1.1), the mass of the bottom quark $m_b = 4.18$ GeV sets the upper limit for this production mode and $2m_\mu$ sets the lower limit for the DHB mass to be probed. So we will perform the simulation exploring mass range $0.211 < m_\phi < 4.18$ GeV at 0.2 GeV interval and coupling ranging from $\sin^2\theta = 10^{-2} - 10^{-14}$. A typical example showing the total number of DHBs being produced at $\sin^2\theta = 10^{-10}$ for various mass ranges and the number of decays happening inside ADAM is shown in Figure 8.2.2.

.

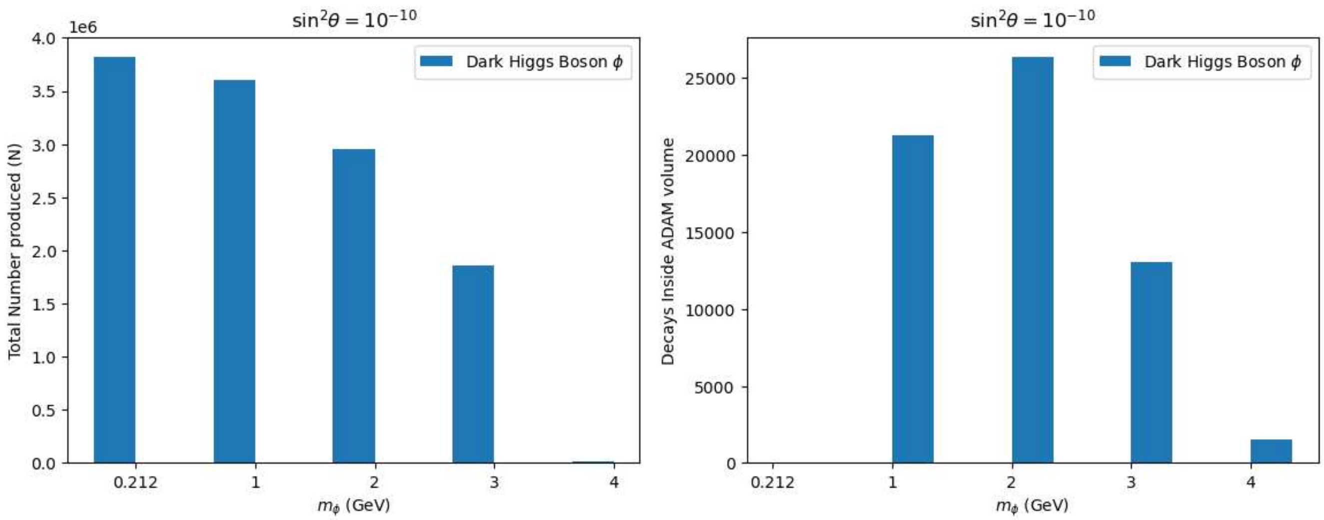

Figure 8.2.2: Total number of DHBs being produced at $\sin^2\theta = 10^{-10}$ various mass ranges and the number of decays happening inside ADAM

In this study, we explored a range of lifetimes (τ_ϕ) and the dark Higgs masses m_ϕ using our *Pythia*8 model for the leptonic decays. We are looking at the process $\phi \to \mu^+\mu^-$, and counting the number of dark Higgs decays to visible states (muons) that happens inside the decay volume of ADAM. As seen in the Eq.(8.1.1), the lifetime of the dark Higgs is inversely proportional to the mixing angle $\sin^2\theta$. Similarly, the rate of dark Higgs bosons being produced in the B meson decays, given by Eq.(7.2.3), are proportional to $\sin^2\theta$. We assume an overall detector/tracking efficiency of 100% and no background for ease of comparison between other experiments in our studies. We then generate limit curves for this process using *Pythia*8 simulations in the parameter space $(m_\phi, \sin^2\theta)$ for the DHB. In order to investigate ADAM's potential to detect the long-lived dark Higgs at the LHC, we simulate maximal fiducial volume of the ADAM detector geometry to generate Monte-Carlo events at a collision energy of $\sqrt{s} = 14$ TeV using the *Pythia*8. We require a minimum of 3 decay signals from $\phi \to \mu^+\mu^-$ in the decay volume ADAM to obtain the exclusion bounds at the 95% C.L (see Appendix §D).

8.2.1.1 ADAM Sensitivity to the Dark Higgs boson for Run 4 ($B \to X_s\phi$)

The DHBs produced in the rare decays of B mesons at the $\sqrt{s}$ = 14 TeV HL - LHC could decay within the ADAM's detector volume. Following the similar procedure as [93] by using the process $B \to K\phi$ as a proxy for $B \to X_s\phi$, we estimate the reach in dark Higgs parameter space $(m_\phi, \sin^2\theta)$ with ADAM. In Figure 8.2.3, we illustrate by the solid red contour the region of parameter space where at least three $\phi \to \mu^+\mu^-$ decays happen within the ADAM's volume. The branching ratio for $\phi \to \mu^+\mu^-$ as seen in Figure 7.2.1, along with the varying lifetime (τ_ϕ) and the branching ratio for the inclusive B decays given as a function of $(m_\phi, \sin^2\theta)$ creates the visible ripples in the contour.

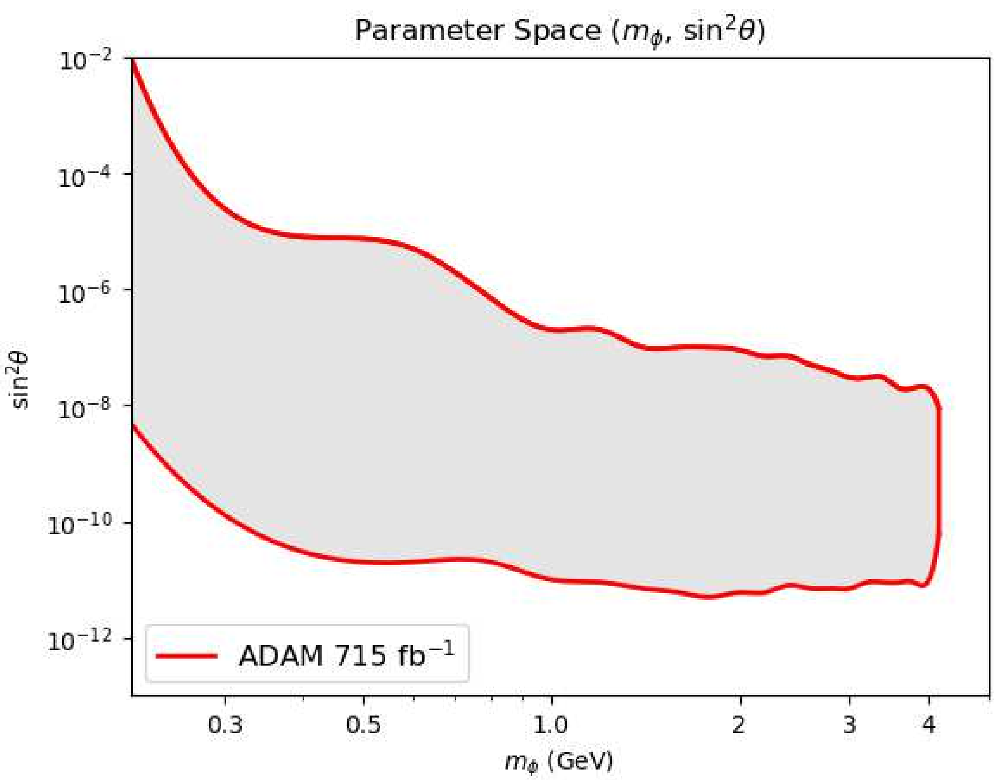

Figure 8.2.3: Projected sensitivity of ADAM for $B \to X_s(\phi \to \mu^+\mu^-)$ in the parameter space $(m_\phi, \sin^2\theta)$ is shown in the red contour. The bounds are shown assuming 100% tracking efficiency and background-free environment at 95 % C.L.

In this plot, the upper region in the parameter space is for DHB being produced high in numbers but with shorter lifetimes and vice versa. As seen in Eq.(8.1.1), the cut-off on the left of the parameter space is because of the lower limit for the DHB mass to be probed set by $2m_\mu$. The region on the right of the parameter space is kinematically forbidden (as set by mass of the bottom quark) in the current DHB production mechanism.

The apparent dip in these exclusion bounds is a result of the dark Higgs mixing with the $f_0(980)$ resonance [108]. The decrease in the number of DHB decays inside ADAM at ~ 1 GeV can be seen in Figure 8.2.2. However, the large decay volume and its close proximity to the IP helps ADAM in limiting the dip in the exclusion bound. Alongside this potential reach of ADAM, Figure 8.2.4 shows current experimental constraints on the parameter space for rare B decays from LHCb (green) [109], the CHARM beam dump (magenta) [110], CODEX-b for $B \to X_s\phi$ (blue) and projected reach of MATHUSLA (cyan) [93], and the projected sensitivity of MAPP-2 (purple) is also presented [108]. The region $\sin^2\theta \sim 10^{-7} - 10^{-4}$ and $m_\phi \sim 1 - 3$ GeV that ADAM and other current experimental constraints exclude is covered by LHCb. The large geometric volume ($\sim 200 \times 200 \times 20$ m^3), 100 m above the ATLAS detector [97], helps MATHUSLA to extend the lower limit in the parameter space. The current status of these experiments are presented in Appendix F.

8.2.2 *Pythia8* Setup for the exotic Higgs decays

As described in §7.2.2.2, another production mechanism for the DHB is through exotic Higgs decays. The branching ratio for exotic Higgs decay is given by Eq.(7.2.4) with the most stringent current bound of implying the value $\lambda < 7.1 \times 10^{-3}$. For the ease of comparison with other experiment, we will set the value of $\lambda = 4.61 \times 10^{-4}$ giving $Br(h \to \phi\phi) = 4700\lambda^2 = 0.001$. As before, we generate SM Higgs produced in p–p collisions at the centre of mass energy $\sqrt{s} = 14$ TeV using the default tune [107] in our Pythia8 model with the $HiggsSM : gg2H$ module turned on.

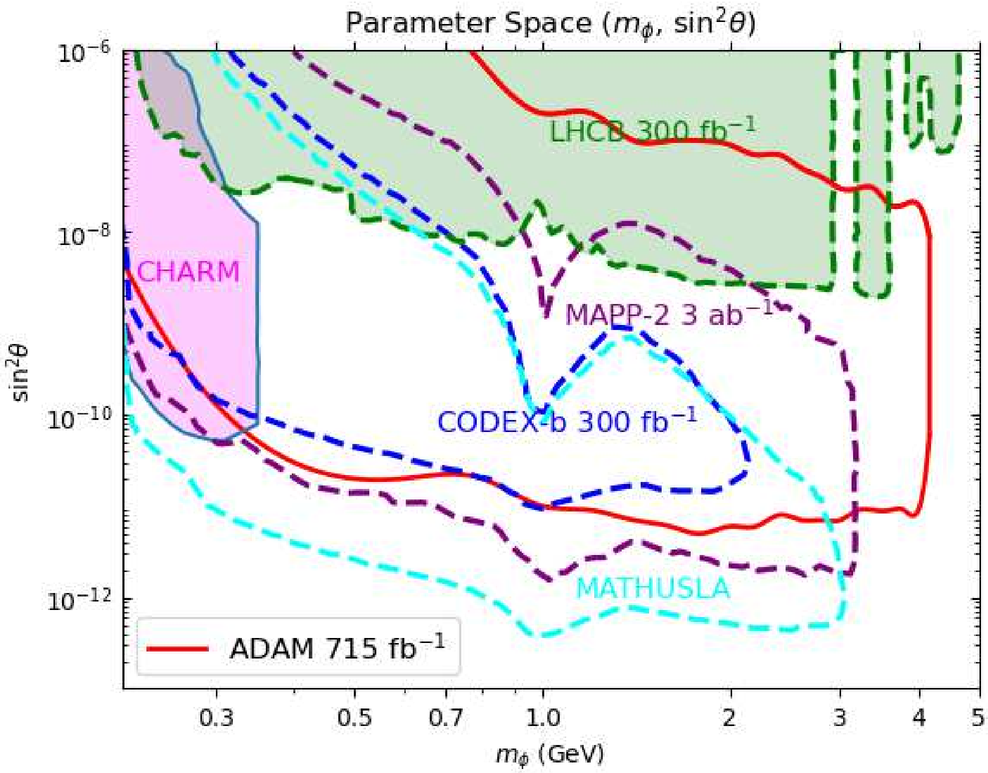

Figure 8.2.4: Projected reach for ADAM for dark Higgs boson along with current experimental bounds [93, 110, 108, 109]. The exclusion bounds shown here all assumes 100% efficiency and background-free environment at 95 % C.L.

The dominant production mechanism for SM Higgs is through the gluon fusion, which for the 14 TeV HL - LHC is $\sigma_{g\bar{g}} = 54.67$ pb [111]. The total number of expected ϕ events can be estimated using Eq. (8.2.1) as

$$N_{\phi,events} \simeq L^{int} \times \sigma_{gg} \times Br(h \to \phi\phi), \tag{8.2.5}$$

where $L^{int} = 715$ fb^{-1} for the HL - LHC during Run4, $\sigma_{b\bar{b}} = 54.67$ pb is the total gluon fusion (gg) cross-section, and $Br(h \to \phi\phi) = 0.001$ is the branching fraction. Hence, the number of events to be generated is constant in this production mechanism with only the lifetime of the DHB dependent in the parameter space. As before we first calculate the lifetimes of the DHB using the decay width formula given by the Eq.(8.1.1) which is constrained by the mass of DHB m_ϕ and the mixing term $\sin^2\theta$. We then explore a range of lifetimes (τ_ϕ) and the dark Higgs masses m_ϕ using our Pythia8 model for the process $\phi \to \mu^+\mu^-$. In this way, we can now perform the simulation for the parameter space $(m_\phi, \sin^2\theta)$ for the DHB. As before, we assume an overall detector/tracking efficiency of 100% and no background for ease of comparison between other experiments in our studies. We then generate limit curves for this process using Pythia8 simulations in the parameter space $(m_\phi, \sin^2\theta)$ for the DHB requiring a minimum of 3 decay signals from $\phi \to \mu^+\mu^-$ produced in the ADAM detector to obtain the exclusion bounds over the dark Higgs parameter space $(m_\phi, \sin^2\theta)$ at the 95% C.L. As before, the simulation is performed at 0.2 GeV mass interval and mixing term ranging from $\sin^2\theta = 10^{-2} - 10^{-14}$.

8.2.2.1 ADAM Sensitivity to the Dark Higgs boson for Run 4 ($h \to \phi\phi$)

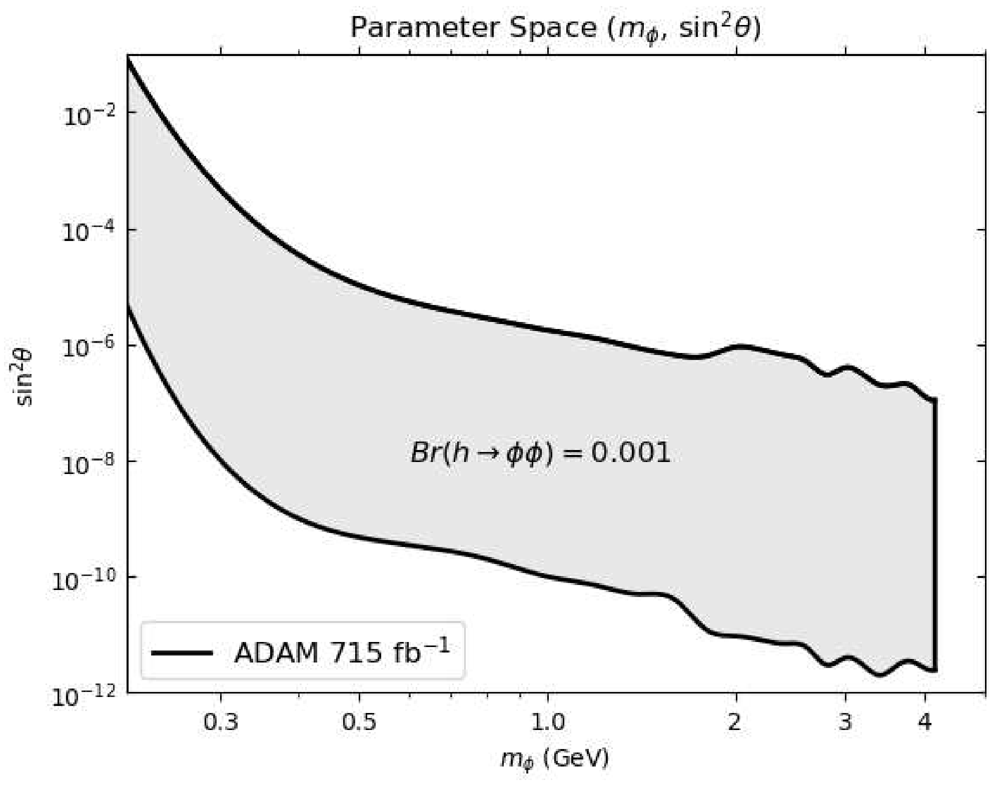

Figure 8.2.5: Projected sensitivity of ADAM for $h \to \phi\phi$ ($\phi \to \mu^+\mu^-$) in the parameter space $(m_\phi, \sin^2\theta)$ is shown in black contour. The bounds are shown assuming 100% tracking efficiency and background-free at 95 % C.L.

The DHBs produced in exotic Higgs decays at the $\sqrt{s} = 14$ TeV HL - LHC could decay within the ADAM's detector volume. In Figure 8.2.5, we illustrate by the solid black contour the region of parameter space $(m_\phi, \sin^2\theta)$ where at least three $\phi \to \mu^+\mu^-$ decays happen within the ADAM's volume. The number of DHBs being produced remains the same because of constant branching fraction for the exotic Higgs decay. The lifetime of DHB is the only variable dependent on the parameter space $(m_\phi, \sin^2\theta)$.

The projected sensitivity of ADAM for the exotic $h \to \phi\phi$ decays in the parameter space $(m_\phi, \sin^2\theta)$ is also shown in Figure 8.2.6 alongside two other experiments [97, 91]. As shown in Eq.(7.1.9), this production mechanism is induced by the non-negligible trilinear interaction term between h and ϕ. The parameter space coverage for MATHUSLA and FASER 2 in exotic Higgs decays is up to $m_\phi < 10$ GeV with decay modes ($\phi \to e^+e^-, \mu^+\mu^-, \tau^+\tau^-, \gamma\gamma$, hadrons) [97, 91].

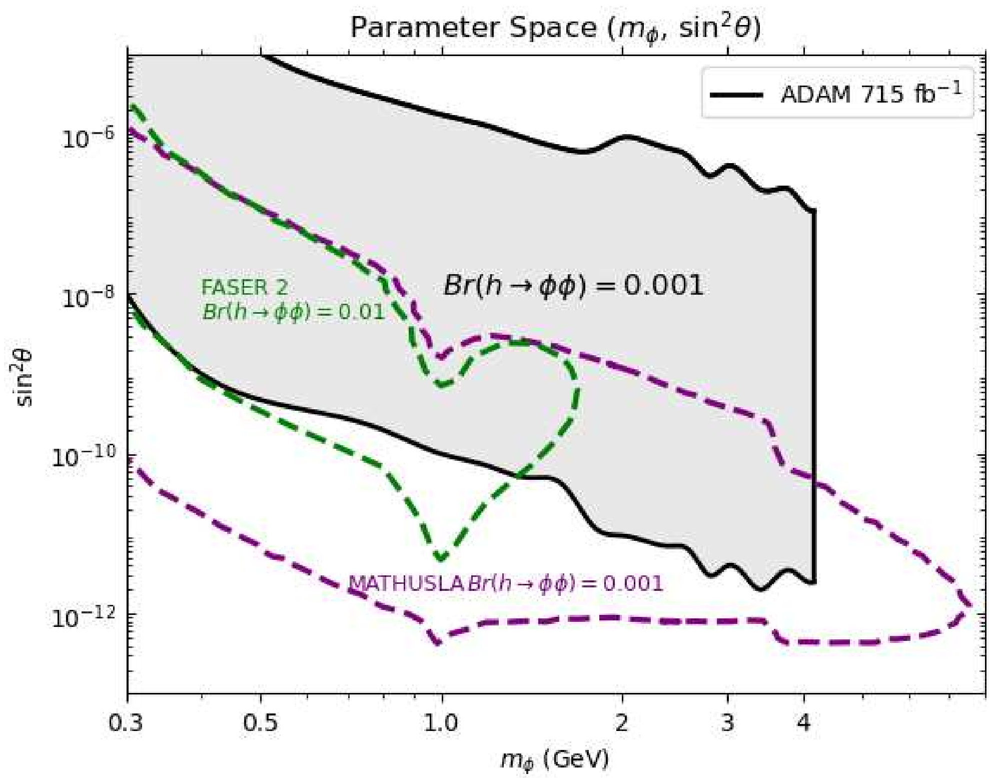

Figure 8.2.6: Projected reach for ADAM for the light DHBs along with current experimental bounds ($L^{int} = 3$ ab^{-1} for MATHUSLA and FASER 2 [97, 91]). The exclusion bounds shown here all assumes 100% efficiency and background-free environment at 95 % C.L.

Chapter 9

Conclusion and Future Outlook

9.1 Conclusion

Neutral LLPs are predicted by a number of BSM theories. These particles may have extremely long lifetimes, which are challenging for the main LHC detectors like ATLAS and CMS to detect. The purpose of the proposed ADAM detector is to enhance the sensitivity of ATLAS to LLP messenger of new physics through a cost-effective enhancement to the current ATLAS detector.

In the current scope of the thesis, an initial estimation of the expected detector resolution for the proposed ADAM detector module with SiPM plugs was performed using $GEANT4$. A simple arrangement with four SiPM plugs in a square grid of scintillating panel was simulated based on the data sheet provided by manufacturer for each detector components. A 4 GeV muon was shot from 4 cm distance to test the spatial resolution of the detector configuration using the squared charged centroiding algorithm based on Anger's logic [75]. The simulation was performed for two different panel thicknesses (1.27 cm and 2.5 cm) and various SiPM spacings (5 cm, 10 cm, 15 cm, 20 cm, 25 cm) in the square grid. Spatial resolution of ~ 1 cm or better is targeted for event position reconstruction in the proposed detector module. The centroiding algorithm using SiPM charge output showed that a resolution of ~ 1 cm or better could be obtained for SiPM spacings of 5 - 10 cm for both scintillating panel thicknesses being considered. The degradation of the spatial resolution outside the central region of the square grid showed a non-linear response [77] of the centroid estimation algorithm. These evaluation were performed to serve as fundamental input for an initial performance (and cost) estimation of the proposed detector configuration.

In the second part of the thesis, we also explored the potential for ADAM to discover DHBs, neutral hidden scalars that couple to the SM through the Higgs portal interaction. As with SM Higgs bosons, DHBs couple preferentially to heavy SM fermions. The widely accepted decay of DHBs to muons ($\phi \to \mu^+\mu^-$) as shown in Figure 7.2.1 to explore the relevant mass range $0.211 < m_\phi < 4.2$ GeV, was considered for the *Pythia*8 simulations. The production of DHBs through the processes $B \to X_s\phi$ and $h \to \phi\phi$ was considered in the scope of the thesis.

We can see that for the upcoming Run-4, ADAM can make significant contributions to existing bounds fro DHBs. It can extend the reach from $m_\phi \sim 0.212 - 4.18$ GeV with mixing as low as $\sin^2\theta \sim 10^{-11}$. ADAM benefits from both the large geometrical volume (~ 12000 m^3) and the proximity to the IP. This allows ADAM to extend both upper and lower limits in the parameter space from the current experimental bounds.

9.2 Future Outlook

Exploring the complete parameter space of unconstrained LLP masses, branching ratios, and lifetimes poses a challenge. The construction of a single detector to cover this extensive range is impractical. Therefore, a strategy involving complementary detectors presents itself as the logical choice for a thorough LLP search in the particle physics experiment community.

The ATLAS and CMS are suitable detectors to search for LLPs for a wide range of lifetimes because of their $\sim 4\pi$ coverage and large size. ADAM can play an important role as a relatively cost effective addition to extend the reach of ATLAS in search for LLPs while utilizing its triggering capabilities. In terms of reach, we projected that ADAM can extend the reach from $m_\phi \sim 0.212 - 4.18$ GeV with mixing as low as $\sin^2\theta \sim 10^{-11}$ for DHBs produced in rare inclusive B decays and exotic Higgs decays. The number of DHBs decaying inside ADAM could be increased by including additional decay modes and production mechanisms, like scalars produced in kaon decays, dark photons radiating off dark Higgs bosons etc. [87].

While light scalars arising from rare meson decays and exotic Higgs decays represent a compelling and intriguing example of hidden sector particle production, there exists other interesting BSM particles with extended lifetimes that might be kinematically reachable with ADAM. The study of the supersymmetric model by Joseph Mitchell Kelly includes a theoretical graviton, predicting the possibility of supersymmetric tau leptons with lifetimes of up to a year, showed 132.3 ± 0.9 events with ADAM [60]. The secondary use case for ADAM is the study cosmic muon showers, or to trigger the ATLAS detector to study comic muon events. A good example topic here is the study of cosmic muon bundles [112].

As discussed in §6.4, a larger number of SiPMs in the readout configuration for accurate point of interaction calculation will be explored in future work. Other potential distributions of SiPM plugs, like a hexagonal footprint, will also be considered for future exploration. Integrating noise factors such as dark counts and crosstalk [68] into SiPM readout will contribute to a more realistic simulation. Additionally, a small prototype will be developed to validate the simulation model. Testing the X-Y fibre embedded model with different spacings for optimization and performance evaluation will also be conducted. These findings will be integrated in optimizing with cost-benefit analysis of full ADAM detector configuration.

Future work will also include the study of trigger rates expected from ATLAS to access the ATLAS event information required for ADAM. As discussed in §4.2, a detailed study of the potential background sources from cosmic muons, particles from collisions at the IP, and beam induced backgrounds is planned for future. ADAM has a promising prospect in detecting long-lived particle avatars of new physics and it also has the capacity to function independently from ATLAS allowing the study of cosmic ray muons and of extremely long-lived trapped particle decays. A comprehensive examination of potential background sources, along with a cost-benefit analysis of modifying ADAM to enhance its capabilities in detecting other BSM particles, would be of great significance.

Bibliography

[1] G. Aad et al., *The ATLAS experiment at the CERN large hadron collider* (2008).

[2] S. Chatrchyan et al., *The CMS experiment at the CERN LHC*, Jinst **3**, S08004 (2008).

[3] G. Aad et al., *Observation of a new particle in the search for the Standard Model Higgs boson with the ATLAS detector at the LHC* **716**, 1–29 (2012).

[4] S. Chatrchyan et al., *Observation of a new boson at a mass of 125 GeV with the CMS experiment at the LHC*, Physics Letters B **716**, 30–61 (2012).

[5] R. L. Workman and Others, *Review of Particle Physics*, PTEP **2022**, 083C01 (2022).

[6] I. J. Aitchison and A. J. Hey, *From relativistic quantum mechanics to QED*, CRC Press (2012).

[7] J. Beacham et al., *Physics beyond colliders at CERN: beyond the standard model working group report*, Journal of Physics G: Nuclear and Particle Physics **47**, 010501 (2019).

[8] A. Arbey and F. Mahmoudi, *Dark matter and the early Universe: a review*, Progress in Particle and Nuclear Physics **119**, 103865 (2021).

[9] T. Virdee, *Beyond the standard model of particle physics*, Philosophical Transactions of the Royal Society A: Mathematical, Physical and Engineering Sciences **374**, 20150259 (2016).

[10] T. Sjöstrand, S. Mrenna, and P. Skands, *A brief introduction to PYTHIA 8.1*, Computer Physics Communications **178**, 852–867 (2008).

[11] S. Agostinelli et al., *GEANT4 - a simulation toolkit*, Nuclear instruments and methods in physics research section A: Accelerators, Spectrometers, Detectors and Associated Equipment **506**, 250–303 (2003).

[12] W. Commons, *Standard model of elementary particles*, `https://en.m.wikipedia.org/wiki/File:Standard_Model_of_Elementary_Particles.svg` (2019), [Online; accessed 14-November-2023].

[13] M. Thomson, *Modern particle physics*, Cambridge University Press (2013).

[14] R. N. Cahn, *The eighteen arbitrary parameters of the standard model in your everyday life*, Reviews of Modern Physics **68**, 951 (1996).

[15] R. P. Feynman, *Space-Time Approach to Quantum Electrodynamics*, Phys. Rev. **76**, 769–789 (1949).

[16] S. L. Glashow, *Partial-symmetries of weak interactions*, Nuclear physics **22**, 579–588 (1961).

[17] A. Salam, *Proe. 8th Nobel Symp., ed. N. Svartholm* (1968).

[18] S. Weinberg, *A model of leptons*, Physical review letters **19**, 1264 (1967).

[19] W. Commons, *Standard model of particle physics, most complete diagram*, `https://en.wikipedia.org/wiki/File:Standard_Model_Of_Particle_Physics,_Most_Complete_Diagram.jpg` (2014), [Online; accessed 14-November-2023].

[20] N. Aghanim et al., *Planck 2018 results-VI. Cosmological parameters*, Astronomy & Astrophysics **641**, A6 (2020).

[21] E. Hubble, *A relation between distance and radial velocity among extra-galactic nebulae*, Proceedings of the national academy of sciences **15**, 168–173 (1929).

[22] A. G. Riess et al., *Observational evidence from supernovae for an accelerating universe and a cosmological constant*, The astronomical journal **116**, 1009 (1998).

[23] B. A. Robson, *The matter-antimatter asymmetry problem*, in *Cosmology, Gravitational Waves and Particles: Proceedings of the Conference*, pages 154–162, World Scientific (2018).

[24] G. Bellini et al., *Neutrino oscillations*, Advances in High Energy Physics **2014**, 1–28 (2014).

[25] G. F. Giudice, *Naturally speaking: the naturalness criterion and physics at the LHC*, Perspectives on LHC physics pages 155–178 (2008).

[26] C. Rovelli, *Notes for a brief history of quantum gravity*, arXiv preprint gr-qc/0006061 (2000).

[27] S. Fartoukh et al., *LHC configuration and operational scenario for run 3*, Technical report (2021).

[28] L. Evans and P. Bryant, *LHC machine*, Journal of instrumentation **3**, S08001 (2008).

[29] K. Aamodt et al., *The ALICE experiment at the CERN LHC*, Journal of Instrumentation **3**, S08002 (2008).

[30] A. A. Alves Jr et al., *The LHCb detector at the LHC*, Journal of instrumentation **3**, S08005 (2008).

[31] B. Acharya et al., *The physics programme of the MoEDAL experiment at the LHC*, International Journal of Modern Physics A **29**, 1430050 (2014).

[32] J. Pinfold, *MoEDAL-MAPP, an LHC Dedicated Detector Search Facility*, arXiv preprint arXiv:2209.03988 (2022).

[33] G. Anelli et al., *The TOTEM experiment at the CERN large hadron collider*, Journal of Instrumentation **3**, S08007 (2008).

[34] J. L. Feng et al., *ForwArd search ExpeRiment at the LHC*, Physical Review D **97**, 035001 (2018).

[35] O. Adriani et al., *LHCf experiment: technical design report*, Technical report, CERN (2006).

[36] G. Acampora et al., *SND@ LHC: The scattering and neutrino detector at the LHC*, arXiv preprint arXiv:2210.02784 (2022).

[37] R. Scrivens et al., *Overview of the status and developments on primary ion sources at CERN* (2011).

[38] H. Bartosik and G. Rumolo, *Performance of the LHC injector chain after the upgrade and potential development*, arXiv preprint arXiv:2203.09202 (2022).

[39] D. Boussard and T. P. R. Linnecar, *The LHC superconducting RF system*, Technical report (1999).

[40] E. Lopienska, *The CERN accelerator complex, layout in 2022* (2022), general Photo.

[41] R. Tomás et al., *Operational scenario of first high luminosity LHC run*, in *Journal of Physics: Conference Series*, volume 2420, page 012003, IOP Publishing (2023).

[42] G. Aad et al., *The ATLAS experiment at the CERN large hadron collider* (2008).

[43] *Technical Design Report*, CERN/LHC pages 97–17 (1997).

[44] L. Rossi et al., *ATLAS inner detector: Technical Design Report, 2*, Technical report, ATLAS-TDR-005 (1997).

[45] J. Badiou et al., *ATLAS barrel toroid: Technical design report*, Technical report, ATLAS-TDR-007 (1997).

[46] *ATLAS liquid argon calorimeter: Technical design report. 1996*, ATLAS TDR **2**, 97–41.

[47] *ATLAS muon spectrometer: Technical Design Report*, CERN (1997).

[48] *ATLAS tile calorimeter: Technical design report*, CERN (1996).

[49] G. Aad et al., *Track Reconstruction Performance of the ATLAS Inner Detector at $\sqrt{s} = 13$ TeV*, Technical report, Tech. Rep. ATL-PHYS-PUB-2015-018. CERN. URL https://cds. cern. ch/record/2037683 (2015).

[50] G. Aad et al., *Alignment of the ATLAS inner detector in Run 2*, The European Physical Journal C **80**, 1194 (2020).

[51] C.-Y. Wong, *Introduction to high-energy heavy-ion collisions*, World Scientific (1994).

[52] *ATLAS magnet system: Technical design report*, CERN (1997).

[53] G. Aad et al., *Triggers for displaced decays of long-lived neutral particles in the ATLAS detector*, arXiv preprint arXiv:1305.2284 (2013).

[54] M. Aaboud et al., *Performance of the ATLAS track reconstruction algorithms in dense environments in LHC Run 2*, The European Physical Journal C **77**, 1–30 (2017).

[55] J. Alimena et al., *Searching for long-lived particles beyond the Standard Model at the Large Hadron Collider*, Journal of Physics G: Nuclear and Particle Physics **47**, 090501 (2020).

[56] R. Bates et al., *The ATLAS SCT grounding and shielding concept and implementation*, Journal of Instrumentation **7**, P03005 (2012).

[57] A. Salzburger, M. Wolter, and S. Todorova, *The ATLAS tracking geometry description*, Technical report (2007).

[58] M. Bandieramonte et al., *FullSimLight: ATLAS standalone Geant4 simulation*, in *EPJ Web of Conferences*, volume 245, page 02029, EDP Sciences (2020).

[59] M. Bandieramonte et al., *The GeoModel tool suite for detector description*, in *EPJ Web of Conferences*, volume 251, page 03007, EDP Sciences (2021).

[60] J. M. Kelly, *A Study of the Detection of Long-Lived Charged Particles With an Auxiliary Detector Above the ATLAS Muon Spectrometer (ADAM)* (2023).

[61] T. Sato et al., *Particle and heavy ion transport code system, PHITS, version 2.52*, Journal of Nuclear Science and Technology **50**, 913–923 (2013).

[62] I. Chalupková and Z. Dolezal, *Non-collision Background Monitoring Using the Semi-Conductor Tracker of ATLAS at LHC* .

[63] G. Battistoni et al., *The FLUKA code: Description and benchmarking*, in *AIP Conference proceedings*, volume 896, pages 31–49, American Institute of Physics (2007).

[64] J. S. Carlson et al., *Taking advantage of disorder: Small-molecule organic glasses for radiation detection and particle discrimination*, Journal of the American Chemical Society **139**, 9621–9626 (2017).

[65] M. Moszyński and B. Bengtson, *Status of timing with plastic scintillation detectors*, Nuclear Instruments and Methods **158**, 1–31 (1979).

[66] E. Dietz-Laursonn et al., *Detailed studies of light transport in optical components of particle detectors*, Technical report, Fachgruppe Physik (2016).

[67] K. Yamamoto, *Newly developed semiconductor detectors by Hamamatsu*, in *International Workshop on New Photon-Detectors*, volume 51, page 004, SISSA Medialab (2008).

[68] *Hamamatsu SiPMs*, https://www.hamamatsu.com/optical-sensors/ (2024).

[69] D. Renker and E. Lorenz, *Advances in solid state photon detectors*, Journal of Instrumentation **4**, P04004 (2009).

[70] Geant4 Collaboration, *Geant4 User's Guide*, CERN (2024).

[71] *Saint-Gobain bc-408 scintillator*, https://www.crystals.saint-gobain.com (2016).

[72] *Kurary Y11 Model WLS Fiber*, http://kuraraypsf.jp/ (2024).

[73] R. Pahlka et al., *Spectral Characterization and Modeling of Wavelength-shifting Fibers*, arXiv preprint arXiv:1911.03790 (2019).

[74] H. O. Anger, *Scintillation camera*, Review of scientific instruments **29**, 27–33 (1958).

[75] V. Babiano et al., *γ-Ray position reconstruction in large monolithic LaCl3 (Ce) crystals with SiPM readout*, Nuclear Instruments and Methods in Physics Research Section A: Accelerators, Spectrometers, Detectors and Associated Equipment **931**, 1–22 (2019).

[76] R. Pani et al., *Revisited position arithmetics for LaBr3: Ce continuous crystals*, Nuclear Physics B-Proceedings Supplements **197**, 383–386 (2009).

[77] P. Aguiar et al., *Geant4-GATE simulation of a large plastic scintillator for muon radiography*, IEEE Transactions on Nuclear Science **62**, 1233–1238 (2015).

[78] G. Aad et al., *A detailed map of Higgs boson interactions by the ATLAS experiment ten years after the discovery*, Nature **607**, 52–59 (2022).

[79] A. Tumasyan et al., *A portrait of the Higgs boson by the CMS experiment ten years after the discovery*, Nature **607**, 60–68 (2022).

[80] S. Coleman and E. Weinberg, *Radiative corrections as the origin of spontaneous symmetry breaking*, Physical Review D **7**, 1888 (1973).

[81] F. R. Clarke, Jackson D and R. R. Volkas, *Phenomenology of a very light scalar* ($100MeV < mh < 10GeV$) *mixing with the SM Higgs*, Journal of High Energy Physics **2014**, 1–28 (2014).

[82] K. A. Foot, Robert and R. R. Volkas, *Cosmological constant in scale-invariant theories*, Physical Review D **84**, 075010 (2011).

[83] E. Gildener and S. Weinberg, *Symmetry breaking and scalar bosons*, Physical Review D **13**, 3333 (1976).

[84] E. Weihs and J. Zurita, *Dark Higgs models at the 7 TeV LHC*, Journal of High Energy Physics **2012**, 1–21 (2012).

[85] A. Ariga et al., *FASER physics reach for long-lived particles*, Physical Review D **99**, 095011 (2019).

[86] D. Curtin et al., *Exotic decays of the 125 GeV Higgs boson*, Physical Review D **90**, 075004 (2014).

[87] T. Ferber, A. Grohsjean, and F. Kahlhoefer, *Dark Higgs Bosons at Colliders*, arXiv preprint arXiv:2305.16169 (2023).

[88] A. Djouadi, J. Kalinowski, M. Muehlleitner, and M. Spira, *HDECAY: Twenty++ years after*, Computer Physics Communications **238**, 214–231 (2019).

[89] T. Bringmann et al., *Freezing-in a hot bath: resonances, medium effects and phase transitions*, Journal of High Energy Physics **2022**, 1–35 (2022).

[90] M. W. Winkler, *Decay and detection of a light scalar boson mixing with the Higgs boson*, Physical Review D **99**, 015018 (2019).

[91] J. L. Feng et al., *Dark Higgs bosons at the forward search experiment*, Physical Review D **97**, 055034 (2018).

[92] F. Bezrukov and D. Gorbunov, *Light inflaton hunter's guide*, Journal of High Energy Physics **2010**, 1–22 (2010).

[93] V. V. Gligorov et al., *Searching for long-lived particles: a compact detector for exotics at LHCb*, Physical Review D **97**, 015023 (2018).

[94] B. Grinstein, L. Hall, and L. Randall, *Do B meson decays exclude a light Higgs?*, Physics Letters B **211**, 363–369 (1988).

[95] R. S. Chivukula and A. V. Manohar, *Limits on a light Higgs boson*, Physics Letters B **207**, 86–90 (1988).

[96] A. Lenz, *B-mixing in and beyond the Standard model*, arXiv preprint arXiv:1409.6963 (2014).

[97] J. A. Evans, *Detecting hidden particles with MATHUSLA*, Physical Review D **97**, 055046 (2018).

[98] V. Khachatryan et al., *Searches for invisible decays of the Higgs boson in pp collisions at* $\sqrt{s} = 7, 8,$ *and* $13\ TeV$, Journal of High Energy Physics **2017**, 1–56 (2017).

[99] G. Aad et al., *Search for invisible decays of a Higgs boson using vector-boson fusion in pp collisions at* $\sqrt{s} = 8\ TeV$ *with the ATLAS detector*, arXiv preprint arXiv:1508.07869 (2015).

[100] M. Aaboud et al., *Search for an invisibly decaying Higgs boson or dark matter candidates produced in association with a Z boson in pp collisions at* $\sqrt{s} = 13\ TeV$ *with the ATLAS detector*, Physics Letters B **776**, 318–337 (2018).

[101] M. Shaposhnikov and I. Tkachev, *The* ν*MSM, inflation, and dark matter*, Physics Letters B **639**, 414â417 (2006).

[102] F. Bezrukov and D. Gorbunov, *Light inflaton after LHC8 and WMAP9 results*, Journal of High Energy Physics **2013**, 1–17 (2013).

[103] J. A. Evans et al., *Looking for the WIMP next door*, Journal of High Energy Physics **2018**, 1–52 (2018).

[104] X. Chu, T. Hambye, and M. H. Tytgat, *The four basic ways of creating dark matter through a portal*, Journal of Cosmology and Astroparticle Physics **2012**, 034 (2012).

[105] G. G. Raffelt, *Stars as laboratories for fundamental physics: The astrophysics of neutrinos, axions, and other weakly interacting particles*, University of Chicago press (1996).

[106] B. Patt and F. Wilczek, *Higgs-field portal into hidden sectors*, arXiv preprint hep-ph/0605188 (2006).

[107] P. Skands, S. Carrazza, and J. Rojo, *Tuning PYTHIA 8.1: the Monash 2013 tune*, The European Physical Journal C **74**, 3024 (2014).

[108] M. A. Staelens, *Physics From Beyond the Standard Model: Exotic Matter Searches at the LHC with the MoEDAL-MAPP Experiment*, Ph.D. thesis, Alberta U. (2021).

[109] R. Aaij et al., *Search for long-lived scalar particles in B+ $\rightarrow$ K+ χ (μ+ μ-) decays*, Physical Review D **95**, 071101 (2017).

[110] F. Bergsma et al., *Search for axion-like particle production in 400 GeV proton-copper interactions*, Physics Letters B **157**, 458–462 (1985).

[111] C. Anastasiou et al., *High precision determination of the gluon fusion Higgs boson cross-section at the LHC*, Journal of High Energy Physics **2016**, 1–101 (2016).

[112] E. González Hernández et al., *Cosmic-ray studies with experimental apparatus at LHC*, Symmetry **12**, 1694 (2020).

[113] I. Boiarska et al., *Phenomenology of GeV-scale scalar portal*, Journal of High Energy Physics **2019**, 1–45 (2019).

Appendix A

Hidden Sector Mechanism

A detailed description and derivation can be found in [13, 86, 81].

A.1 Complex Scalar Field

Let us consider a complex scalar field $\phi = \frac{1}{\sqrt{2}}(\phi_1 + i\phi_2)$, with the potential given by $V(\phi) = \mu^2(\phi^*\phi) + \lambda(\phi^*\phi)^2$. The corresponding Lagrangian is given by

$$\mathcal{L} = (\partial_\mu\phi)^*(\partial^\mu\phi) - V(\phi). \tag{A.1.1}$$

The Lagrangian can also be expressed in terms of the two real scalar fields ϕ_1 and ϕ_2 as

$$\mathcal{L} = \frac{1}{2}(\partial_\mu\phi_1)(\partial^\mu\phi_1) + \frac{1}{2}(\partial_\mu\phi_2)(\partial^\mu\phi_2) - \frac{1}{2}\mu^2(\phi_1^2 + \phi_2^2) - \frac{1}{4}\lambda(\phi_1^2 + \phi_2^2)^2. \tag{A.1.2}$$

The Lagrangian given in Eq. (A.1.1) has a global $U(1)$ symmetry because it is invariant under the transformation $\phi \to \phi' = e^{i\alpha}\phi$ since $\phi'^*\phi' = \phi^*\phi$. For the potential to have a finite minimum, λ must be a positive. The shape of the potential now depends on the choice of the sign of μ^2. When $\mu^2 > 0$, the minima of the potential occurs when both of the fields (ϕ_1 and ϕ_2) are zero. If $\mu^2 < 0$, the potential has an infinite set of minima defined by

$\phi_1^2 + \phi_2^2 = \frac{-\mu^2}{\lambda} = \nu^2$. The physical vacuum state will now correspond to a particular point in a circle, which breaks the global $U(1)$ symmetry of the Lagrangian. The vacuum state can now be chosen to be in the real direction $(\phi_1, \phi_2) = (\nu, 0)$, and the field can now be expanded by writing $\phi_1(x) = \eta(x) + \nu$ and $\phi_2(x) = \xi(x)$, which gives

$$\phi = \frac{1}{\sqrt{2}}(\eta + \nu + i\xi). \tag{A.1.3}$$

The Lagrangian written in terms of the fields η snd ξ is

$$\mathcal{L} = \frac{1}{2}(\partial_\mu \eta)(\partial^\mu \eta) + \frac{1}{2}(\partial_\mu \xi)(\partial^\mu \xi) - V(\eta, \xi), \tag{A.1.4}$$

where $V(\eta, \xi) = \mu^2\phi^2 + \lambda\phi^4$ with $\phi^2 = \phi\phi^* = \frac{1}{2}[(\nu + \eta)^2 + \xi^2]$. The potential can now be written in terms of the fields η and ξ using $\mu^2 = -\lambda\nu^2$ as

$$V(\eta, \xi) = -\frac{1}{4}\lambda\nu^4 + \lambda\nu^2\eta^2 + \lambda\nu\eta^3 + \frac{1}{4}\lambda\eta^4 + \frac{1}{4}\lambda\xi^4 + \lambda\nu\eta\xi^2 + \frac{1}{2}\lambda\eta^2\xi^2. \tag{A.1.5}$$

The quadratic term in the field η can be identified as a mass, and the terms with powers of three or four can be identified as the interaction terms. The Lagrangian can now be written as

$$\mathcal{L} = \frac{1}{2}(\partial_\mu \eta)(\partial^\mu \eta) - \frac{1}{2}m_\eta^2\eta^2 + \frac{1}{2}(\partial_\mu \xi)(\partial^\mu \xi) - V_{int}(\eta, \xi), \tag{A.1.6}$$

where $m_\eta = \sqrt{2\lambda\nu^2}$ and the interaction term is given by [13]

$$V_{int}(\eta, \xi) = \lambda\nu\eta^3 + \frac{1}{4}\lambda\eta^4 + \frac{1}{4}\lambda\xi^4 + \lambda\nu\eta\xi^2 + \frac{1}{2}\lambda\eta^2\xi^2. \tag{A.1.7}$$

The Lagrangian given in Eq.(A.1.6) represents a scalar field η with mass $m_\eta = \sqrt{2\lambda\nu^2}$ and a massless scalar field ξ. The particles described by the massless scalar field ξ is called the Goldstone boson [83], which corresponds to the the excitations in the direction where the potential do not change.

A.2 The Higgs Mechanism

The Lagrangian for a complex scalar field ϕ in Eq.(A.1.1) is not invariant because of the presence of derivatives under the $U(1)$ local gauge transformation $\phi(x) \to \phi^{'}(x) = e^{ig\chi(x)}$ [13]. The $U(1)$ local gauge invariance can be achieved by replacing the derivatives in the Lagrangian with the corresponding covariant derivatives $\partial_\mu \to D_\mu = \partial_\mu + igB_\mu$. The Lagrangian can now be written as

$$\mathcal{L} = (D_\mu \phi)^*(D^\mu \phi) - V(\phi^2), \tag{A.2.1}$$

which is gauge invariant if the new gauge field B_μ transforms as [13]

$$B_\mu \to B_\mu^{'} = B_\mu - \partial_\mu \chi(x). \tag{A.2.2}$$

The combined Lagrangian for the complex scalar field ϕ and the gauge field B is given by

$$\mathcal{L} = -\frac{1}{4}F^{\mu\nu}F_{\mu\nu} + (D_\mu \phi)^*(D^\mu \phi) - \mu^2\phi^2 - \lambda\phi^4, \tag{A.2.3}$$

where $F^{\mu\nu}F_{\mu\nu}$ is the kinetic term for the new field and $F^{\mu\nu} = \partial^\mu B^\nu - \partial^\nu B^\mu$. The gauge field B is required to be massless because the mass term $\frac{1}{2}m_B B_\mu B^\mu$ would break the gauge invariance [13]. The covariant term in Eq.(A.2.3) can be written out as

$$(D_\mu \phi)^*(D^\mu \phi) = (\partial_\mu \phi)^*(\partial^\mu \phi) - igB_\mu \phi^*(\partial^\mu \phi) + ig(\partial_\mu \phi^*)B^\mu \phi + g^2 B_\mu B^\mu \phi^* \phi. \tag{A.2.4}$$

The Lagrangian from Eq.(A.2.3) can now be expressed

$$\mathcal{L} = -\frac{1}{4}F^{\mu\nu}F_{\mu\nu} + (\partial_\mu \phi)^*(\partial^\mu \phi) - igB_\mu \phi^*(\partial^\mu \phi) + ig(\partial_\mu \phi^*)B^\mu \phi + g^2 B_\mu B^\mu \phi^* \phi - \mu^2\phi^2 - \lambda\phi^4. \tag{A.2.5}$$

As discussed in §A.1, with the choice of $\mu^2 < 0$, the vacuum state is degenerate, which spontaneously breaks the symmetry of the Lagrangian in Eq.(A.2.5). With the vacuum state chosen to be $\phi_1 + i\phi_2 = \nu$, the complex scalar field can be expanded like it was done in Eq.(A.1.3) as

$$\phi(x) = \frac{1}{\sqrt{2}}(\eta(x) + \nu + i\xi(x)). \tag{A.2.6}$$

Substituting ϕ from Eq.(A.2.6) in Eq.(A.2.5) gives the Lagrangian in the form

$$\mathcal{L} = -\frac{1}{4}F^{\mu\nu}F_{\mu\nu} + \frac{1}{2}g^2\nu^2 B_\mu B^\mu + \frac{1}{2}(\partial_\mu \eta)(\partial^\mu \eta) - \lambda\nu^2\eta^2 + \frac{1}{2}(\partial_\mu \xi)(\partial^\mu \xi) - V_{int} + g\nu B_\mu(\partial^\mu \xi). \tag{A.2.7}$$

The breaking of the symmetry produced the massive scalar field η and a massless Goldstone boson ξ as before. The gauge field B was required to be massless before, which has now acquired a mass term $\frac{1}{2}g^2\nu^2 B_\mu B^\mu$. The gauge boson has become massive in Eq.(A.2.7) and has one additional longitudinal polarization state. The term $g\nu B_\mu(\partial^\mu\xi)$ represents a direct coupling between the Goldstone field ξ and the gauge field B. The Goldstone field ξ in Eq.(A.2.7) can be eliminated from the Lagrangian by making the appropriate gauge transformation [13]. Using

$$\frac{1}{2}(\partial_\mu \xi)(\partial^\mu \xi) + g\nu B_\mu(\partial^\mu \xi) + \frac{1}{2}g^2\nu^2 B_\mu B^\mu = \frac{1}{2}g^2\nu^2\left[B_\mu + \frac{1}{g\nu}(\partial_\mu \xi)\right], \tag{A.2.8}$$

and making the gauge transformation as

$$B_{\mu(x)} \to B_\mu^{'}(x) = B_\mu(x) + \frac{1}{g\nu}\partial_\mu \xi(x), \tag{A.2.9}$$

the Lagrangian from Eq.(A.2.7) now becomes

$$\mathcal{L} = -\frac{1}{4}F^{\mu\nu}F_{\mu\nu} + \frac{1}{2}g^2\nu^2 B_\mu^{'} B^{\mu'} + \frac{1}{2}(\partial^\mu \eta)(\partial_\mu \eta) - \lambda\nu^2\eta^2 - V_{int}. \tag{A.2.10}$$

The physical properties of the theory remains unchanged by the gauge transformation in Eq.(A.2.9) since the original Lagrangian was constructed to be invariant under the local $U(1)$ gauge transformations. The Goldstone field ξ no longer appears in the Lagrangian. The choice of the gauge corresponds to taking $\chi(x) = -\frac{\xi(x)}{g\nu}$ in Eq.(A.2.2). The gauge transformation of the original complex scalar field $\phi(x)$ is now

$$\phi(x) \to \phi^{'}(x) = e^{-ig\frac{\xi(x)}{gv}}\phi(x) = e^{-i\frac{\xi(x)}{\nu}}\phi(x). \tag{A.2.11}$$

The complex scalar field expanded about the physical vacuum in Eq.(A.2.6) can be expressed to first order as $\phi(x) \sim \frac{1}{\sqrt{2}}[\nu+\eta(x)]e^{i\xi(x)/\nu}$ [13]. The effect of the gauge transformation from Eq.(A.2.11) on the original complex scalar field is given by

$$\phi(x) \to \phi^{'}(x) = \frac{1}{\sqrt{2}}e^{-i\xi(x)/\nu}[\nu + \eta(x)]e^{i\xi(x)/\nu} = \frac{1}{\sqrt{2}}(\nu + \eta(x)). \tag{A.2.12}$$

The gauge in which the Goldstone field $\xi(x)$ is eliminated from the Lagrangian is known as the unitary gauge. This leads to the complex scalar field being entirely real

$$\phi(x) = \frac{1}{\sqrt{2}}(\nu + \eta(x)). \tag{A.2.13}$$

A.3 The Standard Model Higgs

The Higgs mechanism was used to generate a mass for the gauge boson corresponding to a $U(1)$ local gauge symmetry. In the Salam-Weinberg model [18, 17], three Goldstone bosons will be required to provide the longitudinal degrees of freedom of the $\mathrm{W}^{\pm}$ and Z bosons. Because the Higgs mechanism is required to generate the masses of the electroweak gauge bosons, one of the scalar fields must be neutral, written as ϕ^0, and the other must be charged such that ϕ^+ and $(\phi^+)^* = \phi^-$ give the longitudinal degrees of freedom of the $\mathrm{W}^{\pm}$. The minimal Higgs model consists of two complex scalar fields in a weak isospin doublet [13]

$$H = \begin{pmatrix} \phi^+ \\ \phi^0 \end{pmatrix} = \frac{1}{\sqrt{2}} \begin{pmatrix} \phi_1 + i\phi_2 \\ \phi_3 + i\phi_4 \end{pmatrix}, \tag{A.3.1}$$

where the upper and lower components of the doublet differ by one unit of charge. The Lagrangian for this doublet of complex scalar fields is $\mathcal{L} = (\partial_\mu H)^\dagger(\partial^\mu H) - V(H)$, where the Higgs potential is given by $V(H) = \mu^2 H^\dagger H + \lambda(H^+ H)^2$. With the choice of $\mu^2 < 0$, the potential has an infinite set of degenerate minima satisfying $H^\dagger H = \frac{1}{2}(\phi_1^2 + \phi_2^2 + \phi_3^2 + \phi_4^2) = \frac{\nu^2}{2} = -\frac{\mu^2}{2\lambda}$. The neutral photon is required to remain massless after the symmetry breaking. Therefore, the minimum of the potential must correspond to a non-zero vacuum expectation value only of the neutral scalar field ϕ^0 as

$$< 0|H|0 >= \frac{1}{\sqrt{2}} \begin{pmatrix} 0 \\ \nu \end{pmatrix}. \tag{A.3.2}$$

The fields can be expanded about this minimum as before by writing

$$H(x) = \frac{1}{\sqrt{2}} \begin{pmatrix} \phi_1(x) + i\phi_2(x) \\ \nu + \eta(x) + i\phi_4(x) \end{pmatrix}. \tag{A.3.3}$$

After the spontaneous breaking of the symmetry, there will be a massive scalar and three massless Goldstone bosons, which will ultimately give the longitudinal degrees of freedom of the $W^\pm$ and Z bosons [13]. As shown before in §A.2, the Higgs doublet can be written in the unitary gauge as

$$H = \frac{1}{\sqrt{2}} \begin{pmatrix} 0 \\ \nu + h \end{pmatrix}. \tag{A.3.4}$$

Appendix B

Dark Higgs Decays

B.1 Relevant Dark Higgs Decay Channels

The branching ratios of the dark Higgs boson was presented in Figure 7.2.1. Some of the relevant decay channels are presented in the table below. The table presents the the specific decay channels that opens up at specific m_ϕ and its relevance.

Table B.1.1: Relevant scalar decay channels as adapted from [113].

Channel	Opens at [MeV]	Relevant from [MeV]	Relevant to [MeV]
$\phi \to \gamma\gamma$	0	0	1.02
$\phi \to e^+e^-$	1.02	1.02	212
$\phi \to \mu^+\mu^-$	211	211 & 1668	564 & 2527
$\phi \to \pi^+\pi^-$	279	280	1163
$\phi \to K^+K^-$	987	996	2000
$\phi \to gg$	275	2000	4178
$\phi \to s\bar{s}$	990	2000	3807
$\phi \to c\bar{c}$	3740	3797	–
$\phi \to \tau^+\tau^-$	3560	3608	–

B.2 Decay Length Formula

Using the relativistic formula for energy $E = \gamma mc^2$, where $\gamma = \frac{1}{\sqrt{1-\beta^2}}$, and $\beta = \frac{v}{c}$. We can write

$$E^2 = \gamma^2 (mc^2)^2 \tag{B.2.1}$$

$$(pc)^2 + (mc^2)^2 = \gamma^2 (mc^2)^2 \implies (pc)^2 = (mc^2)^2 (\gamma^2 - 1) \tag{B.2.2}$$

$$\frac{(pc)^2}{(mc^2)^2} = (\gamma^2 - 1) \tag{B.2.3}$$

$$= \frac{\beta^2}{1 - \beta^2} \tag{B.2.4}$$

Now we can write

$$\frac{pc}{mc^2} = \frac{\beta}{\sqrt{1 - \beta^2}} = \gamma\beta \tag{B.2.5}$$

Hence,

$$\gamma\beta = \frac{p}{mc}. \tag{B.2.6}$$

Appendix C

Decay Volume of ADAM Detector

The two separate regions of ADAM as seen in Figure 4.1.3 creates a large decay volume for neutral LLPs decaying in flight. We can approximate the decay volume between the two regions of ADAM as an annulus (region between two concentric circles). As discussed in §4.1, the outer radius (r_2) = 22.9 m and the inner radius (r_1) = 13.6 m. The area of the annulus is given by

$$A = \pi(r_2^2 - r_1^2) \tag{C.0.1}$$

$$\sim 1066m^2. \tag{C.0.2}$$

The area of ADAM approximating as an annulus with an azimuthal coverage of $\frac{\pi}{2}$ is obtained by dividing the area A by 4

$$A_{ADAM} = \frac{1066}{4} \tag{C.0.3}$$

$$= 266.5m^2. \tag{C.0.4}$$

The length of each panels in the ADAM detector is 45 m. Finally we can estimate the decay volume for ADAM as

$$\begin{aligned} V_{ADAM} &= 266.5 \times 45 \\ &\sim 12000m^3. \end{aligned}$$

Appendix D

Requirement of 3 Decay Signals

Bayesian posterior probability maybe used to determine the regions that will have a given probability of containing the true value of a parameter. Let us suppose the outcome of an experiment is characterized by the vector data $\mathbf{x}$, whose probability distribution is dependent on an unknown parameter θ. In Bayesian statistics, the interpretation of probability is more general and includes degree of belief. The knowledge about θ is summarized by the posterior probability density function (p.d.f.) $p(\theta|\mathbf{x})$, which expresses one's state of knowledge about where its true value lies. The integral over any given region gives the degree of belief for θ to take on values in that region is obtained by using Bayes' theorem [5]

$$p(\theta|\mathbf{x}) = \frac{P(\mathbf{x}|\theta)\pi(\theta)}{\int P(\mathbf{x}|\theta')\pi(\theta')d\theta'}, \tag{D.0.1}$$

where $P(\mathbf{x}|\theta)$ is the joint p.d.f for the data as a function of θ, evaluated with the data actually obtained in the experiment, and $\pi(\theta)$ is the prior p.d.f for θ. The integral in the denominator normalizes the posterior p.d.f. to unity.

In a single parameter case, an interval $[\theta_{bottom}, \theta_{up}]$ can be determined which contains a given fraction $(1-\alpha)$ of the posterior probability,

$$1 - \alpha = \int\limits_{\theta_{bottom}}^{\theta_{up}} p(\theta|\mathbf{x})d\theta. \tag{D.0.2}$$

In the case of Poisson variable n, which counts signal events with unknown mean s as well as background with mean b (assumed known). For the signal mean "s", the prior

$$\pi(s) = \begin{cases} 0 & s < 0 \\ 1 & s \geq 0 \end{cases} \tag{D.0.3}$$

can be used to obtain the upper limit on "s" [5]. The likelihood for "s" is given by the Poisson distribution "n" with mean "$s + b$"

$$P(n|s) = \frac{(s+b)^n}{n!} e^{-(s+b)}. \tag{D.0.4}$$

The upper limit s_{up} at the confidence level (C.L) $(1 - \alpha)$ can be obtained by requiring

$$1 - \alpha = \int_{-\infty}^{s_{up}} p(s|n)ds = \frac{\int_0^{s_{up}} P(n|s)\pi(s)ds}{\int_0^{\infty} P(n|s)\pi(s)ds}. \tag{D.0.5}$$

The lower limit of the integration is effectively zero because of the cut-off in the prior $\pi(s)$ given in Eq.(D.0.3). Also, for the signal events, $s \geq 0$ gives $\pi(s) = 1$. Then

$$1 - \alpha = \frac{\int_0^{s_{up}} P(n|s)ds}{\int_0^{\infty} P(n|s)ds}. \tag{D.0.6}$$

In the case of no events and background-free assumption $(n = 0, b = 0)$

$$1 - \alpha = \frac{\int_0^{s_{up}} e^{-s}ds}{\int_0^{\infty} e^{-s}ds}, \tag{D.0.7}$$

where $\int_0^{\infty} e^{-s}ds = 1$. In the absence of an clear discovery, $n = 0$ and the background free assumption $b = 0$,

$$1 - \alpha = \int_0^{s_{up}} e^{-s} ds \tag{D.0.8}$$

$$1 - \alpha = -e^{-s_{up}} - (-e^{-0}) \tag{D.0.9}$$

$$1 - \alpha = -e^{-s_{up}} + 1 \tag{D.0.10}$$

$$\alpha = e^{-s_{up}} \tag{D.0.11}$$

For 95% C.L, $1 - \alpha = 0.95$, which gives $\alpha = 0.05$. Then

$$0.05 = e^{-s_{up}} \tag{D.0.12}$$

$$s_{up} \approx 2.99 \tag{D.0.13}$$

This gives the upper limit on "s" for no clear discovery and background-free assumption. So we will require at least 3 signals for clear discovery at the 95% C.L. For a detailed description, see [5] ("Bayesian Intervals").

Appendix E

Geant4 WorkFlow

To illustrate the structure of a program built with the *GEANT4* framework, it's important to consider the following key aspects:

- Geometry
- Material properties
- Physics processes
- Particles and their properties
- Sensitive detector components
- Access to the simulation data at several levels (tracking)
- Visualization of geometries and trajectories

GEANT4 provides additional C++ classes essential for simulation creation. Additionally, an executable main program must be developed to combine the extended Geant4 classes and perform the simulation. To establish a functional simulation, users need to define fundamental features like physics models, particle types, matter and its geometry for interaction simulation. The framework offers interfaces for eight user classes, with three being mandatory:

- *G4VUserDetectorConstruction*: User has to provide information about the geometry of the detector (DetectorConstruction) that shall be simulated.

- *G4VPhysicsList*: User defines the physics process classes (PhysicsList) to be used.

- *G4VUserPrimaryGeneratorAction*: User has to provide information about the initial properties of the primary particles (Primaries).

The next list of classes which are not mandatory but necessary for the simulation in the scope of thesis is presented below:

- *G4UserRunAction*: User can specify actions to be executed at every start and end of every Run.

- *G4UserEventAction*: User can specify actions for every Event

- *G4UserStackingAction*: User can select the particle tracks of high interest

- *G4UserTrackingAction* : User can specify action for the particle tracks

- *G4UserSteppingAction*: User can customize the step to step behavior

A Run represents a single simulation process with a defined number of events, which can be identical or by changing the random number seed. A Track represents the instantaneous state of a particle between two track points. Entire particle trajectories are typically not retained due to memory constraints.

E.1 Geometrical Construction

As mentioned above, in the DetectorConstruction class users define all detector components, specifying volume types and their alignment for simulation. This entails detailing the chemical composition of materials to compute quantities like absorption length and corrections for energy loss using the Bethe-Bloch formula. Additionally, optical process properties such as refractive indices, PDE, and reflectivity are set here. $GEANT4$ presents two challenges for creating or modifying complex geometric setups. Firstly, positions and rotations for placing volumes must be specified relative to the mother volume, which can require complex calculations. $GEANT4$ boasts extensive optical physics simulation, enhancing its capability for particle-physics simulations. Defining a volume involves three steps: defining a Solid containing geometrical information, creating a LogicalVolume merging a Solid with physical information like material, and finally creating a PhysicalVolume by combining LogicalVolume information with rotation and position in a mother volume, accomplished through Placement.

E.2 Physics List

In the PhysicsList, relevant processes are activated. This class allows for the implementation of specific processes or processes within a defined energy range. Optical physics holds a unique position in $GEANT4$, introducing optical photons and new properties for materials and optical surfaces. Assigning optical properties to materials is necessary for simulating optical physics processes, including user-defined and predefined materials. Each material requires at least a refractive index and attenuation length spectrum. Special optical materials like scintillators and WLS materials additionally need emission spectra and rise and decay times specified. Emission spectra are defined as a function of particle energy and must be sorted by rising energy values. While refractive index and attenuation length values are interpolated linearly between two given points, emission spectra values are not; instead, the mean of energy-dependent quantity values between two points is applied for interpolation.

E.3 Primary Particle

The G4ParticleGun initiates single G4Events within a G4Run. Users define the number of primary particles and their properties, including particle type, initial position, kinetic energy or momentum, and momentum direction. These properties can be fixed values or probability distributions. Users set the number and starting properties, such as position, direction, momentum, and polarization if applicable, of the primary particle(s), along with their type and charge. All intrinsic particle properties are sourced from the PDG50-Database [5] and processed by an instance of the G4ParticleGun.

Appendix F

Status of Proposed Experiments

The status of the various proposed experiments whose experimental bounds were used to compare with the reach of ADAM are listed below [93, 110, 108, 109, 91]:

1. CHARM: Out of Commission

2. LHCb: Operational

3. CODEX-b: CODEX-beta, a small $2 \times 2 \times 2$ m^3 pilot detector approved as a $2024 - 2025$ LHCb R&D project

4. MATHUSLA: Proposal, a new proposal is being implemented with revised geometry and reduced size

5. FASER 2: Proposal

6. MAPP-2: Proposal